# Alma Mater Studiorum – Università di Bologna

DOTTORATO DI RICERCA IN
## CHIMICA
Ciclo: XXVIII

**Settore Concorsuale di afferenza:**   03/A2

**Settore Scientifico disciplinare:**    CHIM/02

# ELECTROCHEMISTRY OF NANOCOMPOSITE MATERIALS FOR ENERGY CONVERSION

**Presentata da:**              Alessandro Boni

<table>
<tr><td><b>Coordinatore Dottorato</b></td><td><b>Relatore</b></td></tr>
<tr><td>Prof. Aldo Roda</td><td>Prof. Francesco Paolucci</td></tr>
<tr><td></td><td><b>Correlatore</b></td></tr>
<tr><td></td><td>Dr. Giovanni Valenti</td></tr>
</table>

**Esame finale anno 2016**

*"There is no passion to be found in playing small*

*- in settling for a life that is less than the one you are capable of living"*

Nelson Mandela

*to my growing family*

# Preface

This thesis is submitted in partial fulfilment for the degree of Doctor of Philosophy (PhD) in Chemistry at the University of Bologna (Italy, XXVIII doctoral cycle). The work herein presented has been carried out in the EMFM Electrochemistry Laboratory (Electrochemistry of Molecular and Functional Materials) of the Chemistry Department "Giacomo Ciamician" from January 1$^{st}$ 2013 to 31st December 2015, under the supervision of Prof. Francesco Paolucci and the co-supervision of Research Assistant Dr. Giovanni Valenti.

A significant part of the thesis has been inspired by and conducted in collaboration with the *Materials, Environment and Energy (MEE) research group* of Prof. Paolo Fornasiero, and the *Carbon Nanotechnology Group* (CNG) of Prof. Maurizio Prato, both in the Department of Chemical and Pharmaceutical Science, at the University of Trieste (Italy). *MEE* and *CNG* performed the synthesis and part of the physical characterization of the studied nanocomposite materials, whose properties regarding electrocatalytic hydrogen evolution and $CO_2$ reduction are respectively reported in Chapter 1 and Chapter 2. M*EE* and *CNG* have also provided the lab space for several field work campaigns of electrochemical measurements. For these and other reasons they are greatly acknowledged for their contribution in the work.

The photo-electrochemistry work reported in Chapter 3 stems from an ongoing collaboration with the Electrochemical Energy Lab (EEL) at Massachusetts Institute of Technology, where I spent six months of research (March-September 2015) under the supervision of Prof. Yang Shao-Horn and supported by a "Marco Polo" scholarship for international research mobility.

# Abstract

Energy is the most relevant technological issue that the world experiences today, and the development of efficient technologies able to store and convert energy in different forms is urgently needed. The storage of electrical energy is of major importance and electrochemical processes are particularly suited for the demanding task of an efficient inter-conversion.

A potential strategy is to store electricity into the chemical bonds of electrogenerated fuels, like hydrogen and/or energy-dense hydrocarbons. This conversion can be accomplished by water splitting and $CO_2$ electrolysis. In this context, are herein presented three different electrochemical approaches towards water and $CO_2$ reduction.

In Chapter 1 is reported a novel class of nanostructured electrocatalysts, **MWCNTs@Pd/TiO₂**, able to efficiently reduce water at neutral pH. Multi-walled carbon nanotubes, Pd nanoparticles and titanium dioxide are mutually integrated within the nanocomposites, whose electrocatalytic properties are thoroughly investigated and optimized. By electrochemical methods it is rationalized the effect of each building block on the overall activity, which originate from the synergic cooperation of the three units.

In Chapter 2 is presented an electrochemical study of **MWCNTs@CeO₂**, a noble-metal free electrocatalyst with a similar architecture to **MWCNTs@Pd/TiO₂**. The electroreduction of $CO_2$ has often the drawbacks of a poor selectivity and high energy losses for the high overpotential required to drive the reaction. However, detailed studies of **MWCNTs@CeO₂** highlights the possibility to convert $CO_2$ to formic acid at very low overpotential and with a high selectivity. A reaction mechanism that involves the participation of surface hydride species and the $CeO_2$ shell is proposed.

Finally, in Chapter 3 is presented a photo-electrochemical approach to hydrogen production. Solar energy is converted to hydrogen via water reduction on the surface of a catalyst-free, oxide-protected solar cell. The large solar-to-hydrogen activity of the photocathode assembly has been explained by a combination of experimental and theoretical studies.

x

# Table of Contents

# List of Symbols & Abbreviations

| | |
|---|---|
| $\alpha$ | Electron transfer coefficient |
| AM1.5g | Air Mass 1.5 Global |
| ALD | Atomic Layer Deposition |
| $b$ | Tafel slope |
| BET | Brunauer, Emmett and Teller areas |
| B-V | Butler-Volmer equation |
| CA | Chronoamperometry |
| CB | Conduction Band |
| $CE_{MAX}$ | Maximum collection efficiency |
| CHP | Combined Heat and Power |
| $CO_2RR$ | Electrochemical $CO_2$ reduction reaction |
| CV | Cyclic Voltammetry |
| $C_{dl}$ | Capacitance of the double-layer (analogous to $C_H$) |
| $C_G$ | Capacitance of the Guy layer |
| $C_H$ | Capacitance of the Helmotz layer |
| $C_{SC}$ | Capacitance of the space charge |
| c-Si | Crystalline silicon solar cell |
| $\vec{\gamma}_i$ | Observable charge transfer coefficient |
| DFT | Density Function Theory |
| ECSA | Electrochemical Surface Area |
| EDX | Energy-Dispersive X-ray Spectroscopy |
| EELS | Electron Energy Loss Spectroscopy |
| EIS | Electrochemical Impedance Spectroscopy |
| $E_{app}$ | Applied potential |
| $E_{eq}$ | Equilibrium potential |
| $E_F$ | Fermi Energy |
| $E_{F,n}$ | Quasi-Fermi Energy of electrons |
| $E_{F,p}$ | Quasi-Fermi Energy of holes |
| $E_{FB}$ | Flatband potential |
| $E_g$ | Bandgap Energy |
| EQE | External Quantum Efficiency |
| $E_{sub}$ | Applied potential at the substrate |
| $E_{tip}$ | Applied potential at the tip |
| F | Faraday constant |
| FCs | Fuel Cells |
| F.E. | Faradaic Efficiency |
| FRA | Frequency Response Analyzer |

| | |
|---|---|
| $\Delta G_{ad}$ | Free energy of adsorption |
| GC | Glassy Carbon electrode |
| G.C. | Gas Chromatography |
| $H_{abs}$ | Absorbed hydrogen |
| $H_{ad}$ | Adsorbed hydrogen |
| HER | Hydrogen Evolution Reaction |
| HOR | Hydrogen Oxidation Reaction |
| HHV | Higher Heating Value |
| HR-TEM | High-Resolution Transmission Electron Microscopy |
| H-UPD | Hydrogen Underpotential deposition |
| I.C. | Ionic Chromatography |
| IPCE | Incident Photon-to-Current Efficiency |
| J | Current density |
| $J_0$ | Exchange current density |
| $J_{sub}$ | Current density at the substrate |
| $J_{tip}$ | Current density at the tip |
| $J_{SC}$ | Short-circuit current |
| $k_i$ | Rate constant of process $i$ |
| L.C. | Liquid Chromatography |
| LHV | Lower Heating Value |
| LSV | Linear Seep Voltammetry |
| MBE | Molecular Beam Epitaxy |
| MECs | Microbial Electrolysis Cells |
| m.p. | melting point |
| MS analysis | Mott-Schottky analysis |
| $N_D$ | Number of donors |
| NMR | Nuclear Magnetic Resonance |
| OCP | Open Circuit Potential |
| OER | Oxygen Evolution Reaction |
| ORR | Oxygen Reduction Reaction |
| PB | Phosphate Buffer |
| PCET | Proton Coupled Electron Transfer |
| PDMS | Polydimethylsiloxane |
| PEC | Photo-electrochemistry |
| PEC HER | Photo-electrochemical Hydrogen Evolution Reaction |
| PEMFCs | Polymer Electrolyte Fuel Cells |
| PTFE | Poly-Tetra-Fluoro-Ethylene (Teflon) |
| PV | Photovoltaic |
| p-Si | $p$-type silicon |
| R | Gas constant |
| *rds* | rate-determining step |

| | |
|---|---|
| RFBs | Redox Flow Batteries |
| SECM | Scanning ElectroChemical Microscopy |
| SG/TC | Substrate Generation – Tip Collection |
| SOFCs | Solid Oxide Fuel Cells |
| SPE | Screen Printed Electrode |
| TOF | Turnover Frequency |
| $TOF_0$ | Turnover Frequency at zero overpotential |
| TON | Turnover Number |
| UME | Ultra Microelectrode |
| VB | Valence Band |
| $V_{OC}$ | Photovoltage |
| $V_{SC}$ | Space-charge potential |
| V-H | Volmer-Heyrovsky mechanism |
| V-T | Volmer-Tafel mechanism |
| XPS | X-Ray Photoelectron Spectroscopy |
| Z | Impedance |
| Z' | Real impedance |
| Z'' | Imaginary impedance |
| $\emptyset$ | Diameter |
| $\emptyset_{EXT}$ | External diameter |
| $\eta$ | Overpotential |
| $\eta_{kin}$ | Kinetic overpotential |
| $\eta_{iR}$ | Uncompensated overpotential |
| $\eta_{conc}$ | Concentration overpotential |
| $\eta_{abs}$ | Efficiency of light absorption |
| $\eta_{ct}$ | Efficiency of the interfacial charge-transfer |
| $\eta_{transp}$ | Efficiency of charge transport |

# INTRODUCTION

# INTRODUCTION

## I.0. A general picture

Energy is the most important technological issue that the world experiences today. Our modern lives run on various form of energy, that are mostly not produced in a sustainable way by the exploitation of fossil energy resources, namely oil, coal and natural gas. Indeed, 87% of the global primary energy supply is provided by non-renewable fossil fuels, complex molecules that take millions of years to form from natural processes and that cannot be regenerated in the human time-scale.[1-3]

The easy-to-use energy stored in the chemical bonds of fossil fuels, made them the most exploited, corrupted and dangerous source of energy in the world, making imperative the urgent need for alternatives. Moreover, the availability of fossil fuels on the planet is limited,[4] and their geographical distribution is restricted to a few regions, being the cause of multiple conflicts. The main problem of fossil fuels utilization is the combustion process with which energy is extracted out of them. Such process has an efficiency that is strictly limited by thermodynamic, and also produces carbon dioxide ($CO_2$) a dangerous greenhouse gas. Even if $CO_2$ is not the worst gas with a greenhouse effect, its enormous release in the atmosphere due to mankind activities is a major issue that we are experiencing today. $CO_2$ emissions in the atmosphere broke the 400ppm threshold in 2014 with an astonishing raise during the last decades (+30% from 1960),[5] that contributes to increase the global temperature on Earth.

Up to now the great advantages of fossil fuels in terms of availability, relatively easy storage, distribution and energy extraction made them the best sparring partners for mankind evolution. The realization that the drawbacks are worst the advantages, fortunately encouraged the development of technologies able to capture other form of renewable energy resources with the lowest possible impact on the delicate equilibrium of Earth. Renewable energies like wind, solar, biomass, etc. are now about to reach a 10% of overall share in the global energy supply,[1] and thanks to their widespread distribution they are becoming always more integrated.

Regarding electrical energy production, the contribution of renewables exceeds 22%, but fossil fuels are still responsible for the 69% of the global production.

Considering the thermal losses of power plants, this all fossil-based electricity corresponds roughly to the consumption of 5000 GW of primary power.[6] Ideally, if all the fossil-based electricity is replaced with a renewable electricity source,[7] approximately \$300 billion/yr of coal and natural gas, and $1.25 \times 10^{13}$ kg/yr of $CO_2$ emissions ( $\sim 40\%$ of all fossil-fuel-related $CO_2$ emissions), will be saved.[8]

Besides reducing $CO_2$ emissions, the widespread utilization of renewables is often able by itself to supply the local the demand of electrical energy.[6] This virtuous quality, however, poses the question about how to stock the surplus of electricity produced during peak production times and not adsorbed by the grid.[9] These intrinsic intermittent and diluted forms of energy then require to be stored and efficiently reconverted under different forms when needed. Electrochemical processes and related technologies are particularly suited for this purpose, and can thus accomplish the demanding task of a highly efficient conversion. Batteries,[10] supercapacitors,[11] RFBs,[12] electrolyzers[13] and FCs[14] are all very actual technologies that play a fundamental role in the energy game. Some of them have reached a higher level of maturity, but also for the most emerging ones always more and more efforts are spent worldwide to further improve their performances, especially in terms of durability and efficiency.

The coupling of two technologies like electrolyzers and FCs is an example of how we can get the most out of renewable energies, minimizing losses and increasing the overall efficiency. A possible practical situation in which electricity production and conversion are integrated in a residential building is shown in Fig. **I.1**.
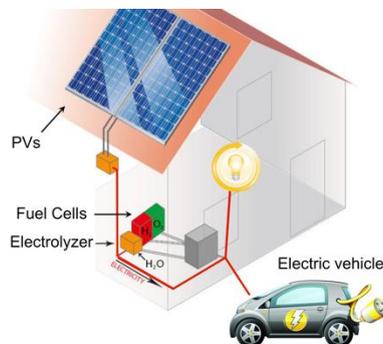


**Figure I.1:** proposed combination of photovoltaics, electrolyzers and fuel cells in a self-powered house that operate as a power station or gas station depending on the time of day. During daytime PVs produce electricity used to fuel production in an electrolyzer, and to the batteries of an electric car. During nightime the fuels produced during the day are converted to electricity (or heat) thanks to FCs. Adapted from www.dailytech.com

Electricity produced by photovoltaics is stored in the forms of hydrogen molecules in an electrolyzer, where $H_2$ and $O_2$ are evolved respectively at the cathode (reduction reaction, Eq. **I.1a**) and the anode (oxidation reaction, Eq. **I.1b**) from the splitting of water, Eq. **I.1c**. The produced $H_2$ can than be compressed, stored and transported far away from the production site, or it can be reused directly at the source as a fuel in a FC, where electrical energy is obtained basically by the opposite reactions that occur in an electrolyzer (i.e. HOR, ORR, Eq. **I.1d**).

$$4H_2O + 4e^- \rightarrow 2H_2 + 4OH^- \qquad \text{Eq. I.1a}$$
$$2H_2O \rightarrow O_2 + 4e^- + 4H^+ \qquad \text{Eq. I.1b}$$
$$2H_2O \rightarrow 2H_2 + O_2 \qquad \text{Eq. I.1c}$$
$$2H_2 + O_2 \rightarrow 2H_2O \qquad \text{Eq. I.1d}$$

In this way, for example, the extra energy produced during the day by PVs can be stored in the bonds of $H_2$ molecules and then reconverted to electrical energy using a FC during dark hours when solar energy cannot supply the electricity demand. Moreover, the stored $H_2$ can also be used to produce heat by means of stationary CHP systems, the most established market for fuel cells,[15] or as an alternative to natural gas for water heating and gas cooking.[16]

Other than for stationary applications, another actual field where hydrogen is seen to play a very important role is the transportation sector. Vehicles powered by the electricity generated from PEMFCs are thought to get 80% of the entire market (cars and trucks) by 2050.[17] Toyota, the biggest automotive company in the world, is very committed in FCs research, recognizing the need for a big change, and, obviously, the rise of new markets/business. Their first commercial fuel-cell-powered vehicle, the Toyota Mirai, has been launched on September 2015,[18] matching the expectations of the European Commission that in 2008 saw a very similar scenario for the hydrogen/fuel cell road map.[19]

In this context it is evident that hydrogen and related technologies are fundamental elements for the development of low-carbon energy systems, providing a major opportunity to shift the current carbon-based global energy economy, to a cleaner, renewable and sustainable one (the so-called "hydrogen economy").[20] For its near-zero or zero end-use emissions and to be a continually replenished resource, hydrogen can be an ideal sustainable energy carrier. Some of its advantages are: high energy conversion efficiencies, production from water with no emissions,

abundance, different forms of storage (e.g. gaseous, liquid, or in metal hydrides), long-distance transportation, ease of conversion to other forms of energy and two-fold higher HHV and LHV than any other conventional fuel (more heat is produced from $H_2$ combustion, making hydrogen convenient also for heating systems).[16,21]

One of the most attractive, long-term features of the $H_2$-economy is the so-called security of feedstock supply.[22] Water is globally available and above all is not environmentally dangerous. On the other hand, besides the numerous ways for producing $H_2$ many of them are not very mature, resulting in high production costs and/or low efficiencies.[23] Nowadays steam reforming is the most extensive method for $H_2$ production,[24] but water electrolysis is getting more relevance and has a great potentiality to increase its contribution, especially after the recent discovery of very promising cheap and abundant HER and OER electrocatalysts.[25] So far, this technology did not find application on large scale plants, basically for the high cost of the cathode materials. Platinum is the best choice in terms of activity and stability even in very harsh conditions, but the limited availability and high-cost prevented from a widespread diffusion of hydrogen-based systems like electrolyzers and fuel cells, that need Pt-catalysts. However, in the past 5-7 years, there has been a tremendous progress in the field of non-precious, earth-abundant HER[26-28] and ORR catalysts,[29] with comparable performances to those of platinum. There are now effective alternatives to platinum-group metals catalysts, which was not the case just ten years ago, that will give an up-and-coming future to this sustainable technology.[6]

The approach of storing electrical energy coming from renewables in the form of electro-generated fuels is very flexible, and embrace another promising and exciting strategy. As water is the precursor for hydrogen, another potential candidate for the production of useful chemicals and fuels is carbon dioxide ($CO_2$). The electro-reduction of this detrimental greenhouse gas ($CO_2RR$) generates a rich array of hydrocarbon chemistries. Energy-dense molecules like methane, CO, formic acid, ethylene and methanol can be produced, and they can be further utilized as fuels or as commodity chemicals. These chemical fuels possess higher energy densities than some established energy storage technologies, such as Li-ion batteries,[30] providing a valuable way to store energy and to make it available on demand.

The potential products of $CO_2RR$, if obtained by the conversion of the excess energy produced by renewable resources like solar and wind, would also generate an anthropogenic carbon-neutral cycle. It is worth mentioning that the $CO_2RR$ is not only a zero-emission process, but also reduces the total amount of $CO_2$ from the environment, thus moving towards the ultimate goal of a low-carbon society.

The electrochemical conversion back and forth between (renewable) electricity and electro-generated fuels, whether $H_2$ or C-based fuels, is then a key technology to make significant progress in the reduction of fossil fuels utilization, opening new possibilities for a clean energy production and consumption.

Nanotechnology may have a fundamental role to foster this transition, leveraging the potentiality of the actual state-of-the-art materials. The possibility to obtain tailored nanostructures can in fact deeply impact the fields of electrocatalysis and photo-electrocatalysis for energy related applications, like $H_2$ evolution and $CO_2$ reduction. In the present thesis the properties of different nanostructured systems towards HER and $CO_2RR$ photo-electrocatalysis are reported. By electrochemical methods it is shown how the activity of the studied nanocomposites exceeds by far that resulting from the simple sum of the various constituents, highlighting the occurrence of multiple cooperative effects toward the realization of efficient (photo)-electrocatalysis.


## I.1. Electrocatalysis

Electrocatalysis can be considered as a special case of heterogeneous catalysis. They are closely related phenomena, with the added feature for the former to involve charge transfer electrochemical reactions. These charge transfer reactions occur at the surface of an electrode, with their rate depending on the electrostatic potential drop that develops at the interface with the electrolyte. Thus, electrocatalysis, and electrochemistry in general, has the great advantage to have and added and controllable parameter to play with, in order to alter the rate of a redox reaction.[31]

Strictly speaking, electrocatalysis refers to the case in which the electrode material itself acts as a heterogeneous catalyst, highlighting the necessity of a direct interaction between the electrode and the electroactive species (inner-sphere reactions). By contrast, outer-sphere reactions refer to electron transfer reactions

in which the coordination spheres of the species are not involved. This is usually the case of homogenous electro-catalyzed reactions, where the reduction/oxidation of a catalyst at the electrode then induces the catalytic reaction to occur.

For inner-sphere reactions, the need for a specific interaction with the electrode surface is manifested by the huge dependence of the reaction rate upon the electrode material (HER is a typical example, with kinetic constants that differ up to several order of magnitude), but also the selectivity for products formation can be extremely different (e.g. $CO_2RR$, section **I.4.**).

If an electrochemical system is perturbed from equilibrium (in which the electrode has a certain equilibrium potential) a net electric current flows, with the rate of such electrons-flow that depends on how much the system has been perturbed. The magnitude of such perturbation is identified as the overpotential (defined as the difference between $E_{app}$ and the $E_{eq}$, Eq. **I.2**), that is a basic quantity for any treatment regarding reaction rates of electrochemical reactions.

$$\eta = E_{app} - E_{eq} \qquad \text{Eq. I.2}$$

In general, the correlation between the reaction rate (i.e. the observed current) and electrode potential can be described by the fundamental equation of electrode kinetics, the Butler-Volmer equation:

$$i = i_A - i_C = i_0\left[e^{(1-\alpha)F(E_{app}-E_{eq})/RT} - e^{-\alpha F(E_{app}-E_{eq})/RT}\right] \qquad \text{Eq. I.3}$$

that can be written in terms of $\eta$ by substitution of Eq. **I.2** into Eq. **I.3**

$$i = i_0\left[e^{(1-\alpha)F\eta/RT} - e^{-\alpha F\eta/RT}\right] \qquad \text{Eq. I.4}$$

where $i_A$ and $i_C$ refers respectively to the anodic and cathodic current densities, $i_0$ is the exchange current density, $\alpha$ is the electron transfer coefficient (also known as the symmetry factor) and the other terms have their classical physical meaning.[32]

In the case of electrocatalytic reactions that involve specific interactions among reactants and the electrode surface (i.e. inner sphere reactions), additional considerations have to be made. In this situation, not only electrochemical reactions occur, but also chemical reactions such the adsorption/desorption of intermediates are involved and have to be considered in the overall reaction scheme. Therefore, single-step one electron reactions, whose rate is described by Eq. **I.3** and **I.4**, are just a part of a more complex scenario, in which multistep

reactions take place. Changing the electrode potential is then not the only parameter that controls the reaction rate, but also other factors have a great contribution like the surface concentration of reaction intermediates.

To make more clear the situation, it is reported a general example of a multistep reaction with both chemical and electrochemical reaction steps. Equations **I.5a-b** describe a possible situation, in which a first electron transfer reaction (in this case the reduction of A) leads to the formation of an intermediate Y, which subsequently reacts giving B. Let also consider that the conversion of A into Y is the *rds* (in equilibrium) and the rate of this reaction control the overall kinetics. The free energy diagram of Fig. **I.2** describes the same reaction, with reactants A, intermediates Y and products B.

$$A + e^- \underset{k_{-1}}{\overset{k_1}{\rightleftharpoons}} Y \qquad \text{Eq. I.5a}$$

$$Y \xrightarrow{k_2} B \qquad \text{Eq. I.5b}$$
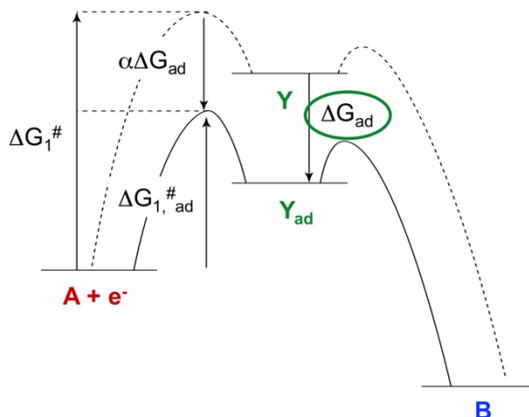


**Figure I.2:** Free energies for Eq. **I.5a** and Eq. **I.5b** in case the intermediate Y does (solid lines) and does not (dashed lines) adsorb at the electrode surface. Adapted from ref. [31].

When there is no interaction between Y and the electrocatalyst, the activation energy for the formation of Y is the highest. By contrast, if an interaction occurs this will stabilize Y and its energy level will be lowered to a new value $Y_{ad}$ ($\Delta G_{ad}$ is negative). The activation barrier will then be smaller and reaction $k_1$ more facile. The reaction rate of $k_1$, Y formation, is described by Eq. **I.6** where is present a contribution of both the chemical adsorption and the electrochemical process.

$$k_1 = k_1^{0'} * e^{-\alpha F\eta/RT} * e^{-\alpha\Delta G_{ad}/RT}$$
<div align="right">Eq. <strong>I.6</strong></div>

From Eq. **I.6** it is evident that not only $\eta$ controls the rate, but also $\Delta G_{ad}$, the adsorption energy of Y. It is worth mentioning that lowering the energy of $Y_{ad}$ has also consequences on the back-reaction $k_{-1}$ and $k_2$, that is B formation.

Without going further into details it is to note that lowering the energy of Y is beneficial and accelerates the forward reaction, but if $\Delta G_{ad}$ is too strong, reaction $k_2$ would become rate-determining and the process more sluggish. For a good catalysis, the right compromise has then to be achieved, with reaction intermediates that should adsorb neither too weakly not too strongly (Sabatier principle). Such "volcano-shaped" dependence of the reaction rate on $\Delta G_{ad}$ is a typical feature of electrocatalysis and will be recalled later in Chapter 1.

The case exemplified above is somehow relatively simple, but it describes many practical situations in which $\Delta G_{ad}$ is the main descriptor of the electrocatalytic activity. Fundamental research in electrocatalysis is then aimed primarily at understanding which properties of the electrode materials affect the most the reactivity by acting on intermediates' stabilization. This concept has been developed in this work, where the dependence of two inner-sphere reactions like HER and $CO_2RR$ on several materials' characteristics is studied by electrochemical methods.

## I.2. Water and $CO_2$ Electrolysis

The potential of electrochemistry as a tool to generate high energy chemicals is known since the 19th century, when Nicholson discovered that hydrogen can be produced from the electrolysis of water. Back in the days, also Jules Verne, recognizing the finite supply of coal and the intrinsic possibilities of $H_2$ derived from water electrolysis, said that "water will be the coal of the future".[17]

Two centuries later, water electrolysis is still an actual topic, and after the discovery that also $CO_2$ can be electrolyzed and transformed at high current densities to fuels and useful chemicals, the electrochemical reduction of $CO_2$ has become a topic of great interest as well.[33]

A schematic representation of an electrolyzer for simultaneous water and $CO_2$ electrolysis is shown in Fig. **I.3**. In this two compartment electrochemical cell, $CO_2$

feed gas and water are reduced at the cathode to chemical gaseous fuels like $CH_4$, $H_2$ and CO, and also possibly to liquid fuels like $CH_3OH$. At the anode, water oxidation takes place and $H^+$ ions are transported across the separator (usually a polymeric membrane) to compensate the build-up of a concentration gradient following $H^+$ consumption. This general design may also incorporate a solar input power to operate the device, ideally able to run electrolysis in a "wireless" fashion if thermodynamics requirements are met.[34] In this case appropriate photoelectrodes have to be used, and such photo-electrochemical approach is discussed in Chapter 3.
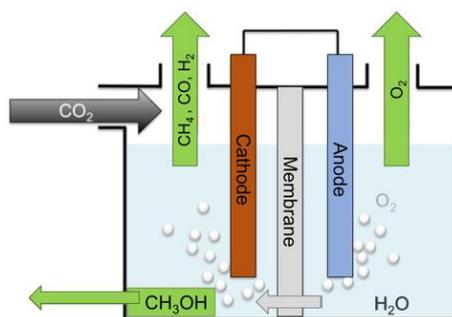
**Figure I.2:** schematic representation of a two compartment apparatus for simultaneous water splitting and $CO_2$ reduction. $CO_2$ feed gas is converted by the cathode to fuels, water is reduced to $H_2$, and in the anodic compartment water is oxidized to $O_2$. A separator allows protons exchange between the compartment.

The free energy change under standard conditions for the water splitting reaction, Eq. **I.1c**, is $\Delta G° = 237.2$ kJ/mol. This corresponds to an electromotive force $E° = -1.23$ V (the negative sign indicating that the opposite reaction, Eq. **I.1d**, is in fact thermodynamically favored) and set the lowest amount of energy needed to evolve $H_2$ and $O_2$ at the two electrodes of an electrolyzer. Unfortunately, the oxidation reaction that leads to oxygen molecules, Eq. **I.1b**, has very sluggish kinetics that cause this reaction to be the bottleneck of the overall process. To drive the anodic reaction is then required an extra-energy (i.e., an overvoltage) that causes the practical need of $E \sim 1.7$ V or more to split water. The cathodic reaction, Eq. **I.1b**, is much easier, has very fast kinetics, but its main limitation in the context of a widespread diffusion of the electrochemical water splitting technology is the nature of the cathodic material. Pt-based cathodes are indeed the best choice for HER electrocatalysis, by virtue of a low overpotential, high turnover frequency and a wide pH range of stability and activity.[35-37] However, Pt scarcity and cost hinder

its employment on large scale, together with its poisoning by water contaminants and the loss of activity at neutral pH.

Commercial electrolyzers usually operate with Pt cathodes and very acid or basic electrolytes (i.e. conditions with the fastest kinetics). However, the engineering and development of electrodes able to tackle efficient electrocatalysis at neutral pH is also desired. This is required for some highly promising technologies such as MECs[38] or PEC water splitting,[39] where the operating conditions are dictated by the stability of the device (i.e. microbes and photoelectrodes) rather then on the performance of the electrocatalyst package.

## I.3. Mechanisms of water reduction

Water reduction proceeds via subsequent elementary steps, that may or may not involve the exchange of electrons at the electrode surface. They are usually known as the Volmer (Eq. **I.7a**), Heyrovsky (Eq. **I.7b**) or Tafel (Eq. **I.7c**) steps.

$$H_2O + 2e^- \rightarrow H_{ads} + OH^-$$  Eq. **I.7a**

$$H_{ads} + e^- + H_2O \rightarrow H_2 + OH^-$$  Eq. **I.7b**

$$2H_{ads} \rightarrow H_2$$  Eq. **I.7c**
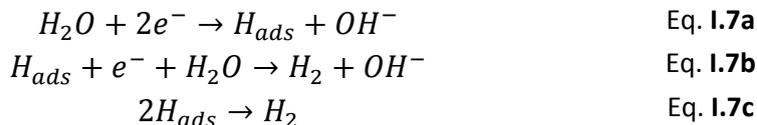
Depending on the pH at which HER is carried out, (acid, pH<5 or base/neutral, pH>5) protons or water molecules are considered as the "true" reactants in the Volmer and Heyrovsky steps. Some recent works, however, claim that both in acid and base HER should proceed via the reduction of protons, produced in base by water dissociation. The same mechanism would then describe HER even at very different pH, with a strong contribution of the $H_{ads}$ intermediate, whose binding energy with the surface referred as the solely descriptor of HER (see also sections **I.1** and **1.0**.[40,41]

From the analysis of HER kinetic currents (i.e. not diffusion limited) is possible to gain insights into the reaction mechanism, possibly identifying which elementary step is the *rds*. Indeed, the slope $b$ in a Tafel plot ($Log\ i = a + b \times \eta$), displays typical values depending on which reaction step (chemical or electrochemical) limit the kinetics of a multistep process, like HER. It is thus possible to discriminate which among the Volmer, Tafel or Heyrovsky step is the *rds.* As derived by the general kinetic equation **A.5** (see Appendix), the coefficient $b$ is defined as:

$$b = \frac{2.3 \times RT}{\vec{\gamma}_i \times F}$$

Eq. **I.8**

where $\vec{\gamma}_i$ is the observable charge transfer coefficient and  is characteristic of a given mechanism (see section **A.1** in the Appendix and ref. [42] for further details]. Slopes of 118, 40 or 30 mV/dec indicate respectively the Volmer, Tafel or Heyrovsky steps as the *rds.* This treatment is based on the assumption of a constant (i.e., potential-independent) surface coverage of $H_{ads}$ and that the electron-transfer coefficient $\alpha = 0.5$.[42]

Usually low Tafel slopes are indications of fast kinetics, with the possibility to reach at a given overpotential higher HER currents than in the case of higher slope values. Other figures of merit of HER electrocatalysis are the exchange current density ($j_0$), the extrapolated current density at the thermodynamic potential E' [$H^+/H_2$] and the onset overpotential. The former is derived by fitting of the kinetic current with the Butler-Volmer equation, while the latter, even if more qualitative, gives a rapid indication about the ability of a certain material to catalyze HER. These descriptors of the electrocatalytic activity here outlined for the case of HER are however general, and apply also to any other electrocatalytic reaction (e.g. HOR, ORR/OER, $CO_2$ Reduction, etc.).[40,43]

A common feature of HER electrocatalysts is the levelling of performances in the pH range from 5 to 9. In Fig. **I.4a** it is shown how the onset overpotential for a Pt disk electrode deviates from the theoretical value in the region 5 < pH < 9. This peculiar behavior is related to the intrinsic mechanism of HER process and it has been rationalized both theoretically and experimentally.[44,45,46]
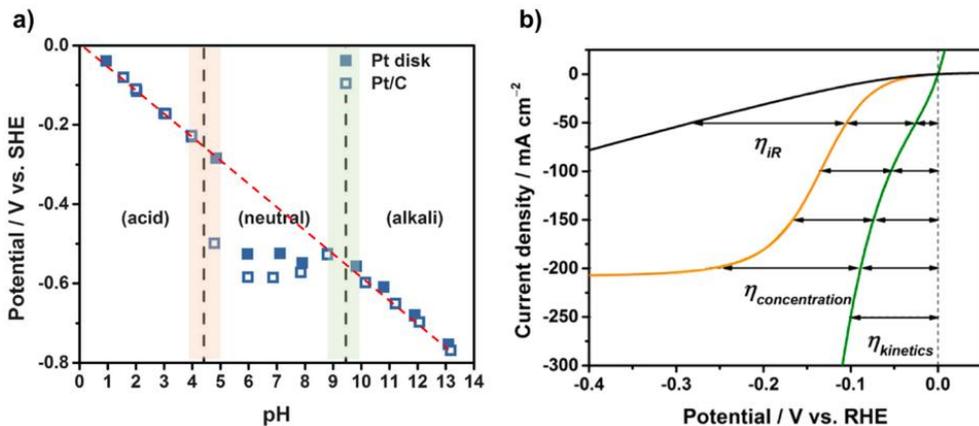
**Figure I.3:** adapted from ref [44] and ref [45] **a)** Effect of the pH on the onset of HER current. It is clear the deviation from the thermodynamic value of 59 mV/pH in the range 5 < pH < 9, where the reactant switching between $H^+$ and $H_2O$ occurs. **b)** Polarization curves for a Pt electrode, rotated at 1600 rpm and dipped in a 1 M PB solution. The contributions to the overall overpotential ($\eta_{tot}$) due to slow kinetics ($\eta_{kin}$), depletion of reactants from the electrode surface ($\eta_{conc}$) and uncompensated resistance ($\eta_{iR}$) are shown.

As outlined by Takanabe,[44,45] and Mayrhofer,[46,47] HER at neutral pH is strongly affected by several factors, like pH changes at the electrode surface (see section **1.0**). A big contribution to the overall rate of HER also comes from concentration overpotentials ($\eta_{conc}$) that may account for up to the 50% of the measured overpotential, $\eta_{tot}$ (see Fig. **I.4b**).[45] Since HER at neutral pH is more limited by "external" factors than the electrocatalyst itself, it is then desirable to develop new systems, more abundant and more scalable than Pt electrodes, able to efficiently sustain HER under these mild conditions.

It has been demonstrated that a key step for the overall HER process at neutral pH is the intermediate formation ($H_{ad}$) via water dissociation and subsequent reduction,[40,41]

$$H_2O \rightleftharpoons H^+ + OH^- \xrightarrow{e^-} H_{ad} + OH^-$$   Eq. **I.9**
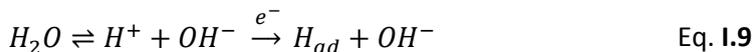
To this end in Chapter 1 it is reported the strategy to improve $H_{ad}$ formation, and then HER efficiency, by integration of a nanometric shell of $TiO_2$ with Pd NPs and multiwall carbon nanotubes, that would promote water adsorption and dissociation at neutral pH. As it will be shown, the nanocomposite shows a peculiar activity for HER that originates from the cooperation between the various building blocks.

## I.4. Electrochemical $CO_2$ reduction reaction ($CO_2RR$)

The effect of an excessive production of carbon dioxide on the future climate of the Earth is being seriously discussed,[48] and $CO_2$ reduction to organic raw materials or fuels would help to reduce this type of atmospheric pollution. For this and other reasons, the reduction of $CO_2$ is a very actual subject, with several attractive features.[49]

Among the known methods for $CO_2$ reduction/conversion (e.g. chemical hydrogenation, thermochemical cycling, biological conversion, etc.), $CO_2RR$ has

several advantages. It operates at ambient temperature and pressure producing very little waste aside from possible wastewater from the electrolyte and it is scalable with a modular design. Moreover, it is usually carried out in the mild conditions of near-neutral aqueous electrolytes (6 < pH < 9).

From a thermodynamic point of view, the direct electrochemical reduction of $CO_2$ is highly endoergic and requires very negative potential to occur (first entry in Table **I.1**). Indeed, the standard potential for radical anion formation (an outer-sphere reaction) is very negative, -1.85 $V_{RHE}$. However, in aqueous solution, $CO_2RR$ does not follow the radical anion formation path, but involves the simultaneous transfer of electrons and protons, in what is called a concerted PCET process. This concerted mechanism lowers the free energy of reaction, that is much more likely to happen, and, as it can be seen in Table **I.1**, entangles the possibility to generate a wide variety of hydrocarbon chemistries ($CH_4$, CO, $CH_3OH$, HCOOH, etc.). Each reaction has a thermodynamic potential much lower than the radical anion formation, and they all reside in a narrow potential region, a fact that somehow implies a general poor control over product distribution.

**Table I.1**. Possible reaction for the electrochemical $CO_2$ reduction in water

| | |
|---|---|
| $CO_2 + e^- \rightarrow CO_2^{\circ-}$ | E = -1.85 $V_{RHE}$ |
| $CO_2 + H_2O_{(l)} + 2\ e^- \rightarrow HCO_2^-{}_{(aq)} + OH^-{}_{(aq)}$ | E = -0.2 $V_{RHE}$ |
| $CO_2 + H_2O_{(l)} + 2\ e^- \rightarrow CO_{(g)} + 2\ OH^-{}_{(aq)}$ | E = -0.1 $V_{RHE}$ |
| $CO_2 + 3\ H_2O_{(l)} + 4\ e^- \rightarrow HCOH_{(l)} + 4\ OH^-{}_{(aq)}$ | E = -0.07 $V_{RHE}$ |
| $CO_2 + 5\ H_2O_{(l)} + 6\ e^- \rightarrow CH_3OH_{(l)} + 6\ OH^-{}_{(aq)}$ | E = 0.02 $V_{RHE}$ |
| $CO_2 + 6\ H_2O_{(l)} + 8\ e^- \rightarrow CH_{4(g)} + 8\ OH^-{}_{(aq)}$ | E = 0.17 $V_{RHE}$ |
| $2\ H_2O_{(l)} + 2e^- \rightarrow H_{2(g)} + 2\ OH^-{}_{(aq)}$ | E = 0 $V_{RHE}$ |

The thermodynamic potentials for each reaction is also reported in the RHE scale (RHE = NHE – 0.059*pH). The hydrogen evolution reaction is a competing process.

In light of the energy-dense products that is possible to obtain, $CO_2RR$ can be seen as a mean for energy storage (e.g. in the conversion of solar to storable chemical energy).[50,51] Of major interest is the conversion of $CO_2$ into fuels such as methane, methanol, formate, carbon monoxide and ethylene. These chemicals can found utilization as precursor for further chemical synthesis (e.g. CO, Ethylene), can be directly burned ($CH_4$), or can be used as fuels in FCs ($CH_3OH$, HCOOH). Formic acid has also been proposed as a convenient mean for hydrogen storage.[52]

Given the complex nature of the $CO_2RR$ process and the variety of possible products, it is very important to develop analytical protocols for the chemical analysis of the reaction products. G.C., I.C., L.C. and NMR, are analytical techniques commonly used to detect gaseous and liquid products. In addition, for a comprehensive understanding of this complex reaction is highly recommended the use of a specific experimental setup, like gas-tight electrochemical cells coupled to G.C. This is required for example for quantification of the Faradaic Efficiencies, then for speculation of the reaction mechanism.

The general low selectivity of $CO_2$ electrocatalysts is one of the major limitations of the electrochemical approach toward $CO_2$ reduction, together with the high overpotentials requested due to kinetic complexity of the reaction.[53] If, from thermodynamics, relatively mild potentials are required to reduce $CO_2$, in practice overpotentials as high as 1 V are needed to generate products with good current densities. This kinetic hindrance arises from several factors: *i)* $CO_2$ is a planar molecule with very strong bonds, and has to undergo substantial conformational modification to be transformed. It thus should not surprise the slow kinetics of this reaction, that translate into high η. Moreover, *ii)* $CO_2$ reduction, except for the direct formation of radical anion, is an inner-sphere reaction that requires a strong interaction with the electrode surface, with electrons flowing after that a specific adsorption takes place. Adsorbed $CO_2$ has then to rearrange on the surface after the addition of multiple proton-electron pairs, forming different reaction intermediates. The stability of these adsorbed species is very sensitive on the chemical environment at the electrode surface and dictates the nature of possible reaction products. This inner-sphere character is also evidenced by the strong dependence of reaction products on the electrode material.[54] It is worth mentioning that water reduction, an inner-sphere heterogeneous reaction as well, is a competing process, with $H_2O$ that rivals with $CO_2$ for free vacant lattice sites on the electrode. Also, *iii)* the poor solubility of $CO_2$ in water, 38 mM at 25°C and 1 atm $CO_2$, limits the maximum expected current densities to values of $\sim$ 10 mA/cm$^2$. Nevertheless, despite these challenges, the possibility to transform a harmful gas into useful products gives tremendous value to the electrochemical $CO_2$ reduction process, motivating research efforts in the field.

Thus far, the bulk of experimental studies has focused on metal electrodes. It has been found that metals like Au, Ag and Pd primarily produce CO, while Sn, In, and

Pb produce formate (HCOO⁻).[33] Cu is by far the most active electrocatalyst, being able to produce a very rich array of products,[55] but up to now its lack of selectivity and its facile poisoning by the electrolyte has limited practical applications. The mechanisms that govern product selectivity in $CO_2$ reduction, especially in the case of Cu, are still an open question. Anyway, it is generally accepted that the selectivity is strongly dependent on the stabilization of the reacting intermediates at the surface, where PCET reactions take place.[53,55,56]

In order to improve the selectivity of $CO_2$ reduction it is then likely needed to optimize the chemistry at the electrode surface, so as to drive and stabilize the adsorption of reaction intermediates, that can in turn lead to the formation of specific products. In Chapter 3 it is highlighted how the integration of nanocrystalline cerium oxide ($CeO_2$) in a carbon-based nanocomposite not only is a valid platform for $CO_2$ adsorption, but also efficiently mediate the electro-hydrogenation of $CO_2$ to formic acid.

## I.5 Photo-electrochemical Hydrogen Evolution (PEC HER)

Energy harvested directly from sunlight offers a desirable approach toward fulfilling the need for a clean energy. Solar energy is a widespread and inexhaustible natural resource. Each day hits the Earth's surface enough solar energy to satisfy the world's population energy demand for the next 16 years at present rates of utilization.[57] However to harness this huge potential remains a big challenge, with scientists that have to leverage the actual state-of-the-art of solar devices, in a way to provide a reliable and economic carbon-free source of electricity or fuels.

To fully utilize solar energy, making its development realistic on the global energy scale, it is very important to overcome the intrinsic limit of a daily and seasonal variability. It is then fundamental to efficiently convert sunlight into chemical fuels, in an equivalent process to what nature does with photosynthesis. The efficient splitting of water into hydrogen (and oxygen), would provide a clean fuel whose only waste product upon utilization is water.[39] Due to similar thermodynamic requirements with water splitting, also the reduction of $CO_2$ to hydrocarbons is a feasible, and even more appealing, process. The ultimate goal of these approaches is the realization of an efficient photo-electrolysis cell that can simultaneously drive

both hydrogen evolution/$CO_2$ reduction and water oxidation, possibly in an unassisted fashion.[34,58,59] To accomplish this new, artificial photosynthesis scheme, an economically viable water splitting cell needs to be developed.[60]

The famous work by Honda and Fujishima in 1970,[61] in which the authors reported electrochemical photolysis of water using $TiO_2$, has been a milestone for the actual energy research. From that paper, altogether with the global energy crisis of the early 1970s, the connection between the potentiality of photo-electrochemistry and solar energy became clear and received worldwide attention. Another, more recent and serious, energy crisis prompted again new efforts in the field, hopefully with the awareness that this is the last train for a big change. As Churchill said ''people and countries can do the right thing once they have exhausted all other alternatives''.[62]

In a PEC device, water splitting can be achieved in a number of different ways. In general, core of the device is the photoactive semiconducting material able to absorb photons and convert them upon generation of a photovoltage. These photoelectrodes can be one (single band gap device) or two (dual band gap device), arranged in different possible configurations (Fig. **I.5**).[39] Regardless of the way they are combined, the liquid/solid junctions in PEC devices present unique challenges to sustain the necessary photovoltages and drive the reduction (at the photocathode) and oxidation (at the photoanode) reactions. In general, PEC devices for water splitting have to harvest efficiently large part of the solar spectrum, to be very stable (i.e. years) and to exhibit rapid charge transfer reactions at the semiconductor/electrolyte interface. It is then very important to address, at the basic research stage, also stability measurements and optical/electrochemical characterization of the devices.[62]



a) n-type photoanode PEC   b) p/n-PEC (tandem cell)
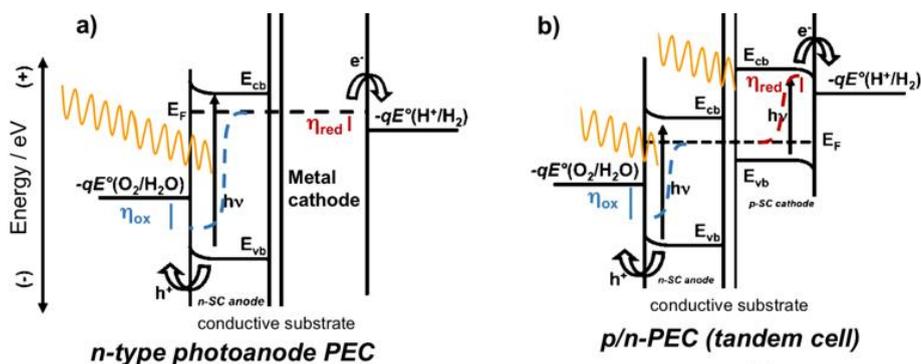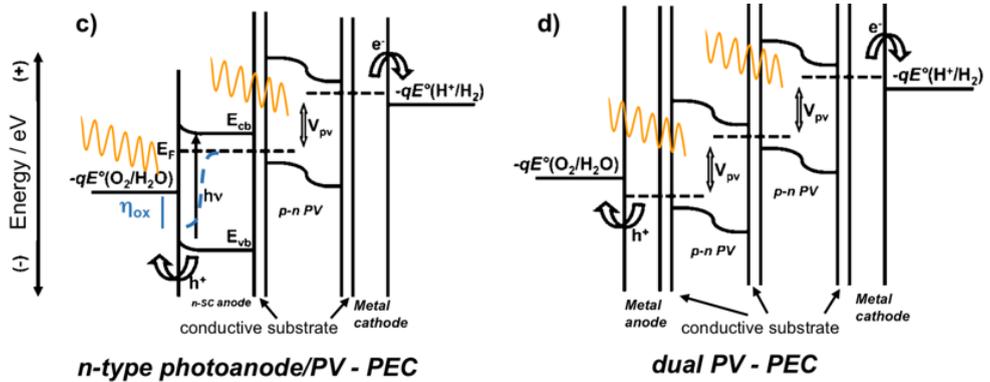
**Figure I.4:** possible semiconductors' configurations for PEC water splitting. In **a)** a *n*-type photo-anode is coupled to a metallic cathode. **b)** *p*-and *n*-type semiconductors are coupled in a tandem device, with HER occurring on the p-type photo-cathode and OER on the n-type photo-anode. In **c)** a *p-n* junction is connected to a *n*-type photo-anode. In this specific case the photovoltage generated by the buried PV, $V_{PV}$, is required to match the energy level of the $H^+/H_2$ couple and promote HER. In **d)** two *p-n* junctions are present, and both are covered by metal electrodes, at which both HER and OER occur. $\eta_{ox}$ and $\eta_{ox}$ represents respectively the overpotentials for OER and HER that originate depending on the band energies of the semiconductors involved.

Usually, a dual band gap configuration is advantageous because it allows to obtain a higher solar energy conversion efficiency to hydrogen (or STH)[63] thanks to a higher obtainable photovoltage. Moreover, it enables to spatially resolve the water splitting half reactions at two different liquid/solid interfaces (fundamental for practical applications to avoid $H_2$ and $O_2$ recombination). Reason of the higher efficiency for dual band gap devices is the possibility to capture more efficiently the incoming sunlight using semiconducting materials with complementary absorption of the solar spectrum. Such systems can approach and also exceed the maximum thermodynamic efficiency of 31% for the conversion of solar energy into electrical free energy, as calculated by Schockley and Queisser for a single absorber.[64]

As previously mentioned, the energy required to split water corresponds to 1.23 eV. Suitable semiconductors have then to absorb photons of energy >1.23 eV, and convert this energy into $H_2$ and $O_2$ (the overall process is 4e$^-$, then 4.92 eV are required). This process to be efficient have to generate photo-excited electron-hole pairs with the right energy. Ideally, a single semiconductor with a band gap ($E_g$) > 1.23 eV can split water if it has conduction band-edge energy ($E_{CB}$) and valence band-edge energy ($E_{VB}$) that straddle with those of the electrochemical potentials of the ($H^+/H_2$) and ($O_2/H_2O$) redox couples (Fig. **I.5**). This fact limits the utilization of single band gap semiconductors because, despite the optimal $E_g$ of some of them

(e.g. 1.4 eV for GaAs, 1.3 eV for InP), poor or no overlap of band energies with the energy of water half-reactions prevent water splitting to occur. Moreover, charge-carrier recombination, and the electron-transfer processes at semiconductor/liquid junctions produce losses (mainly due to slow kinetics) that rise the energy required to drive water splitting to 1.6-2.4 eV for each generated electron-hole pair.[62,65] This practical need for 1.6-2.4 eV motivates the use of multiple semiconductors with different energy gaps, so to increase the output photovoltage.

In addition to an optimal band gap for solar absorption, semiconductor photoelectrodes must have excellent oxidative/reductive stability in contact with aqueous electrolyte solutions. This means that the oxidative and reductive decomposition potentials must be respectively more positive and more negative than the $E_{VB}$ and $E_{CB}$ for water oxidation and water reduction.[32]

A common strategy in PEC water splitting is to study and optimize separately each half reaction. The photoelectrode of interest (-cathode or –anode) is then used as the working electrode in a classical three electrodes cell, where the "other" half reaction occurs at the auxiliary electrode. This configuration allows to evaluate the properties of each electrolyte/semiconductor interface, otherwise impossible in a two-electrodes cell. By varying the potential (i.e. the Fermi energy) at each liquid/solid junction, both in the dark and under illumination, information on the photovoltage, band edge energies, carriers' lifetime and dynamics, surface states, reaction kinetics, etc. can be obtained. The evaluation criteria of PEC water splitting devices originate from the field of photovoltaics/solar cells and many efforts have been spent in order to standardize the protocols for materials' characterization and results' presentation. This is due to avoid misunderstanding and for at-a-glance comparison of the key figures of merit that define the potentiality of a certain material. Several aspects have thus been standardized: from the light source, the broadband solar AM1.5g illumination,[66] to efficiency benchmarking (STH, EQE, etc.).[67]

Coming back to the possible configurations of a PEC device, the situation shown in Fig. **I.5d**, where two p-n photovoltaic modules are connected and coated with metal electrodes, is analogous to connect in series a PV with an electrolyzer. In this approach there is no electrolyte/semiconductor junction and the majority carriers (holes for p-type, electrons for n-type semiconductors) are injected into the

solution through the surface metallic layer which buries and protect the underlying p-n PV cell. If the surface protective layer is thin enough (e.g. nm-thick), also thin films metal oxides, usually not intrinsically conductive, can be adopted for this purpose. Photo-excited electrons may thus flow from the p-n junction to the solution through the nanometric oxide, which completely isolates the semiconductor without affecting light absorption. This strategy has been recently demonstrated to be very promising, especially for the possibility to use classical, well-known, low band-gap semiconductors, like Si or GaAs.[68-70] The protection of these semiconductors, otherwise easy to photo-corrode or photo-passivate in aqueous solutions, enables to obtain high current densities, capitalizing their light absorption capability (their band-gap allow to approach the 31% Schokley-Queisser limit).[37,71] The need for protection layers has been extended not only to "buried" p-n junctions, but also to the most promising new semiconductor materials like $Cu_2O$, $BiVO_4$, InP, $TaO_xN_y$, etc. which are often not intrinsically stable in contact with water.[72]

This approach is thus very flexible, with the possibility to adapt the protective layer to the application of interest and depending on the underlying semiconductor. In Chapter 3, the utilization of a nm-thick protective layer of $SrTiO_3$ oxide on top of a n-p GaAs PV cell for the PEC hydrogen evolution is presented and discussed. The growth of an epitaxial $SrTiO_3$ layer and the optimal band engineering of the device, have shown to drive hydrogen evolution at neutral pH without the need of any catalyst on the surface.

# I.6. Bibliography

1   N. Armaroli, V. Balazni, Solar Electricity and Solar Fuels: Status and Perspectives in the Context of the Energy Transition, *Chem. Eur. J.*, **22**, 32 – 57 (2016).

2   N. Armaroli, V. Balzani, N. Serpone, *Powering Planet Earth—Energy Solutions for the Future* (Wiley-VCH, Weinheim, 2013).

3   N. S. Lewis, D. G. Nocera, Powering the planet: Chemical challenges in solar energy utilization, *PNAS*, **103**, 15729–15735 (2006).

4   OPEC Annual Statistical Bulletin 2015.

5   Mauna Loa Observatory, NOAA/ESRL, USA, www.co2now.org

6   P. C. K. Vesborg, B. Seger, I. Chorkendorff, Recent Development in Hydrogen Evolution Reaction Catalysts and Their Practical Implementation, *J. Phys. Chem. Lett.*, **6**, 951–957 (2015).

7   BP Statistical Review of World Energy 2014 (BP p.l.c.: London, 2014).

8   IEA. World Energy Outlook 2012; International Energy Agency: Paris (2012).

9   H. Hvidtfeldt Larsen, L. Sønderberg Petersen (Eds.), *DTU International Energy Report* 2015.

10  J. Christensen, p. Albertusa, R. S. Sanchez-Carrera, T. Lohmann, B. Kozinsky, R. Liedtkec, J. Ahmeda, A. Kojica, A critical review of Li/air batteries, *J. Electrochem. Soc.,* **159**, R1-R30 (2012).

11  B. E. Conway, *Electrochemical Supercapacitors: scientific fundamentals and technological applications* (Springer Science, New York, 1999).

12  A. Z. Weber, M. M. Mench, J. P. Meyers, P. N. Ross, J. T. Gostick, Q. Liu, Redox flow batteries: a review, *J. Appl. Electrochem.*, **41**, 1137–1164 (2011).

13  K. E. Ayers, E. B. Anderson, C. Capuano, B. Carter, L. Dalton, G. Hanlon, J. Manco, M. Niedzwiecki, Research Advances towards Low Cost, High Efficiency PEM Electrolysis. *ECS Trans,.* **33**, 3– 15 (2010).

14  H. A. Gasteiger, J. Garche, in *Handbook of Heterogeneous Catalysis* (WILEY-VCH Verlag GmbH & Co, Weinheim, Germany, 2008)

15  IPSOS Mori, EST. Homeowners' willingness to take up more efficient heating systems. London, UK: Ipsos MORI and the Energy Saving Trust (EST); (2013).

16  P. E. Dodds, I. Staffell, A. D. Hawkes, F. Li, P. Grunewald, W. McDowall, P. Ekins, Hydrogen and fuel cell technologies for heating: A review, *Int. J. Hydrogen Energy*, **40,** 2065-2083 (2015).

17  J. M. Thomas, Heterogeneous Catalysis and the Challenges of Powering the Planet, Securing Chemicals for Civilised Life, and Clean Efficient Utilization of Renewable Feedstocks, *ChemSusChem*, **7**, 1801 – 1832 (2014).

18  http://www.pressroom.toyota.com

19  European hydrogen and fuel cell road map (European Commission, 2009).

20  J. O. M. Bockris, A hydrogen economy, *Science*, **176**, 1323 (1972).

21 I. Dincer, C. Acar, Review and evaluation of hydrogen production methods for better sustainability, *Int. J. Hydrogen Energy*, **40,** 11094-11111 (2015).

22 R. J. Pearson, M. D. Eisaman, J. W. G Turner, P. P. Edwards, Z. Jiang, V. L. Kuznetsov, K. A. Littau, L. Di Marco, S. R. G. Taylor, *Proc. IEEE*, **100**, 440 (2012).

23 Acar C, Dincer I. Comparative assessment of hydrogen production methods from renewable and non-renewable sources. *Int J Hydrogen Energy*, **39**, 1-12 (2014).

24 N. Z. Muradov, T. N. Veziroglu, From hydrocarbon to hydrogen-carbon to hydrogen economy. *Int J Hydrogen Energy,* **30**, 225-237 (2005).

25 M. S. Faber, S. Jin, Earth-abundant inorganic electrocatalysts and their nanostructures for energy conversion applications, *Energy Environ. Sci.,* **7**, 3519-3542 (2014).

26 J. Kibsgaard, T.F. Jaramillo, F. Besenbacher, Building an appropriate active-site motif into a hydrogen-evolution catalyst with thiomolybdate $[Mo_3S_{13}]^{2-}$ clusters, *Nature Chemistry*, **6**, 248-253 (2014).

27 J. Kibsgaard, Z. Chen, B.N. Reinecke, and T.F. Jaramillo, Engineering the surface structure of $MoS_2$ to preferentially expose active edge sites for electrocatalysis, *Nature Materials*, **11**, 11, 963-969 (2012).

28 T.F. Jaramillo, K. P. Jørgensen, J. Bonde, J. H. Nielsen, S. Horch, I. Chorkendorff, Identification of active edge sites for electrochemical $H_2$ evolution from $MoS_2$ nanocatalysts, *Science*, **317**, 5834, 100-102 (2007).

29 J. Suntivich, K. J. May, H. A. Gasteiger, J. B. Goodenough, Y. Shao-horn, A Perovskite Oxide Optimized for Molecular Orbital Principles. *Science*, **334**, 2010–2012 (2011).

30 Sridhar, N., Hill, D. Carbon dioxide utilization. *Research and Innovation Position Paper – DNV* (2011).

31 K. Krischer, E. R. Savinova, *Fundamentals of electrocatalysis*, in *Handbook of Heterogeneous Catalysis*, *2nd Ed*., Eds. G. Ertl, H. Knozinger, F. Schuth, J. Weitkamp (Wiley-VCH Verlag, Weinheim, 2008).

32 A. J. Bard, L. R. Faulkner, *Electrochemical Methods: Fundamentals and Applications*, (Wiley, New York, ed. 2 ,2001).

33 Y. Hori, K. Kikuchi, S. Suzuki, Production of CO and $CH_4$ in electrochemical reduction of $CO_2$ at metal electrodes in aqueous hydrogen carbonate solution. *Chemistry Letters*, **11**, 1695–1698 (1985).

34 J. Luo, J-H. Im, M. T. Mayer, M. Schreier, M. K. Nazeeruddin, N-G. Park, S. D. Tilley, H. J. Fan, M. Grätzel, Water photolysis at 12.3% efficiency via perovskite photovoltaics and Earth-abundant catalysts, *Science,* **345**, 1593-1596 (2014).

35 N. M. Markovic, B. N. Grgur, P. N. Ross, Temperature-dependent hydrogen electrochemistry on platinum low-index single-crystal surfaces in acid solutions. *J. Phys. Chem. B,* **101**, 5405-5413 (1997).

36  N. M. Markovic, S. T. Sarraf, H. A. Gasteiger, P. N. Ross, Hydrogen electrochemistry on platinum low-index single-crystal surfaces in alkaline solution. *J. Chem. Soc. Faraday Trans.,* **92**, 3719-3725 (1996).

37  R. Mazzaro, A. Boni, G. Valenti, M. Marcaccio, F. Paolucci, L. Ortolani, V. Morandi, P. Ceroni, G. Bergamini, Uniform functionalization of high-quality graphene with platinum nanoparticles for electrocatalytic water reduction. *ChemistryOpen*, **4**, 268 – 273 (2015).

38  Y. Zhang, I. Angelidaki, Microbial electrolysis cells turning to be versatile technology: recent advances and future challenges. *Water Research*, **56,** 11-25 (2014).

39  M. G. Walter, E. L. Warren, J. R. McKone, S. W. Boettcher, Q. Mi, E. A. Santori, N. S. Lewis, Solar water splitting cells, *Chem. Rev.,* **110**, 6446–6473 (2010).

40  J. Durst, A. Siebel, C. Simon, F. Hasché, J. Herranz, H. A. Gasteiger, New insights into the electrochemical hydrogen oxidation and evolution reaction mechanism. *Energy Environ. Sci.,* **7**, 2255-2260 (2014).

41  R. Subbaraman, D. Tripkovic, D. Strmcnik, K-C. Chang, M. Uchimura, A. P. Paulikas, V. Stamenkovic, N. M. Markovic, Enhancing hydrogen evolution activity in water splitting by tailoring $Li^+$-$Ni(OH)_2$-Pt interfaces. *Science,* **334**, 1256-1260 (2011).

42  O'M J. Bockris, A. K. N. Reddy, *Modern Electrochemistry* (Plenum Pr. New York, 1970).

43  W. Sheng, H. A. Gasteiger, Y. Shao-Horn, Hydrogen Oxidation and Evolution Reaction Kinetics on Platinum: Acid vs Alkaline Electrolytes. *J. Electrochem. Soc.* 157, B1529 (2010).

44  T. Shinagawa, A. T. Garcia-Esparza, K. Takanabe, Mechanistic Switching by Hydronium Ion Activity for Hydrogen Evolution and Oxidation over Polycrystalline Platinum Disk and Platinum/Carbon Electrodes, *ChemElectroChem,* **1**, 1497 – 1507 (2014).

45  T. Shinagawa, K. Takanabe, Electrocatalytic Hydrogen Evolution under Densely Buffered Neutral pH Conditions, *J. Phys. Chem. C*, **119**, 20453–20458 (2015).

46  M. Auinger, I. Katsounaros, J. C. Meier, S. O. Klemm, P. U. Biedermann, A. A. Topalov, M. Rohwerdera, K. J. J. Mayrhofer, Near-surface ion distribution and buffer effects during electrochemical reactions, *Phys. Chem. Chem. Phys.*, **13**, 16384–16394 (2011).

47  I. Katsounaros, J. C. Meier, S. O. Klemm, A. A. Topalov, P. U. Biedermann, M. Auinger, K. J. J. Mayrhofer, The effective surface pH during reactions at the solid–liquid interface*, Electrochem. Commun.,* **13**, 634–637 (2011).

48  J. Hansen, D. Johnson, A. Lacis, S. Lebedeff, P. Lee, D. Lind, and G. Russel, Climate impact of increasing atmospheric carbon dioxide, *Science,* **213** 957 (1981).

49    A. M. Appel, J. E. Bercaw, A. B. Bocarsly, H. Dobbek, D. L. Dubois, M. Dubois, G. L. Waldrop, Frontiers, opportunities, and challenges in biochemical and chemical catalysis of $CO_2$ fixation. C*hemical Reviews*, **113**, 6621–6658 (2013).

50    S. Inoue, N. Yamazaki, *Organic and Bioorganic Chemistry of Carbon Dioxide,* (Kodansha Ltd., Tokyo and Wiley, New York, 1982).

51    J. R. Bolton, A. F. Haught, R. T. Ross, in *Photochemical Conversion and Storage of Solar Energy,* Ed. by J. S. Connolly (Academic Pr., New York, 1981).

52    R. Williams, R. S. Crandall, A. Bloom, Using of carbon dioxide in energy storage, *Appl. Phys. Lett.,* **33**, 381 (1978).

53    A. A. Peterson, F. Abild-Pedersen, F. Studt, J. Rossmeisl, J. K. Nørskov, How copper catalyzes the electroreduction of carbon dioxide into hydrocarbon fuels, *Energy Environ. Sci.*, **3**, 1311–1315 (2010).

54    A. J. Bard, Inner-Sphere Heterogeneous Electrode Reactions. Electrocatalysis and Photocatalysis: The Challenge, *J. Am. Chem. Soc.*, **132**, 7559–7567 (2010).

55    M. Gattrell, N. Gupta, A. Co, A review of the aqueous electrochemical reduction of CO2 to hydrocarbons at copper, *J. Electroanal. Chem.*, **594**, 1-19 (2006).

56    A. Verdaguer-Casadevall, C. W. Li, T. P. Johansson, S. B. Scott, J. T McKeown, M. Kumar, I. E. L. Stephens, M. W. Kanan, I. Chorkendorff, Probing the active surface sites for CO reduction on oxide-derived copper electrocatalysts, *J. Am. Chem. Soc.*, 137, 9808-9811 (2015).

57    M. D. Archer, A. J. Nozik, *Nanostructured And Photoelectrochemical Systems For Solar Photon Conversion* (Imperial College Pr., London, 2008).

58    J. Brillet, J. H. Yum, M. Cornuz, T. Hisatomi, R. Solarska, J. Augustynski, M. Graetzel, K. Sivula, Highly Efficient Water Splitting by a Dual-Absorber Tandem Cell. *Nat. Photonics*, **6**, 824–828 (2012).

59    S. Y. Reece, J. A. Hamel, K. Sung, T. D. Jarvi, A. J. Esswein, J. J. H. Pijpers, D. G. Nocera, Wireless Solar Water Splitting Using Silicon-Based Semiconductors and Earth- Abundant Catalysts, *Science*, **334**, 645–648 (2011).

60    N. S. Lewis, Light work with water, *Nature*, **414**, 589- (2001).

61    A. Fujishima, K. Honda, *Nature*, **238**, 37–38 (1972).

62    H-J. Lewerenz, L. M. Peter, *Photoelectrochemical Water Splitting: Materials, Processes and Architectures* (RSC Publishing, Cambridge, 2013).

63    J. R. Bolton, S. J. Strickler, J. S. Connolly, Limiting and realizable efficiencies of solar photolysis of water, *Nature,* **316**, 495 (1985).

64    W. Shockley, H. J. Queisser, Detailed balance limit of efficiency of *p–n* junction solar cells, *J. Appl. Phys.* **32**, 510–519 (1961).

65    J. A. Turner, A realizable renewable energy future, *Science*, **285**, 1493 (1999).

66    http://rredc.nrel.gov/solar/spectra/am1.5/

67    Z. Chen, T. F. Jaramillo, T. G. Deutsch, A. Kleiman-Shwarsctein, A. J. Forman, N. Gaillard, R. Garland, K. Takanabe, C. Heske, M. Sunkara, E. W. McFarland, K.

Domen, E. L. Miller, J. A. Turner, H. N. Dinh, Accelerating materials development for photoelectrochemical hydrogen production: Standards for methods, definitions, and reporting protocols, *J. Mater. Res.*, **25**, 3-16, (2010).

68  L. Ji, M. D. McDaniel, S. Wang, A. B. Posadas, X. Li, H. Huang, J. C. Lee, A. A. Demkov, A. J. Bard, J. G. Ekerdt, E. T. Yu, A silicon-based photocathode for water reduction with an epitaxial $SrTiO_3$ protection layer and a nanostructured catalyst. *Nat Nano*, **10**, 84–90 (2015).

69  S. Hu, M. R. Shaner, J. A. Beardslee, M. Lichterman, B. S. Brunschwig, N. S. Lewis, Amorphous $TiO_2$ coatings stabilize Si, GaAs, and GaP photoanodes for efficient water oxidation. *Science,* **344**, 1005–1009 (2014).

70  M. J. Kenney, M. Gong, Y. Li, J. Z. Wu, J. Feng, M. Lanza, H. Dai, High-Performance Silicon Photoanodes. *Science,* **342**, 836–840 (2013).

71  J. H. Werner, S. Kolodinski, H. J. Queisser, Novel optimization principles and efficiency limits for semiconductor solar cells, J. *Phys. Rev. Lett.* **72**, 3851 (1994).

72  K. Sivula, R. van de Krol. Semiconducting materials for photoelectrochemical energy conversion, *Nat. Rev. Mats.,* **1**, 1-16 (2016).

Chapter 1

# HYDROGEN EVOLUTION REACTION

# Chapter 1

# Hydrogen Evolution Reaction

### 1.0. HER: Introduction & motivation

Lot of work in the field of electrocatalysis is nowadays focused in the development of cheap and abundant materials for the efficient conversion of $H_2O$ into $H_2$ and $O_2$, and vice versa. Much attention is devoted in the field of energy conversion and storage for the great impact that technologies like lithium-air batteries, FCs and water-splitting devices can have to our society. All of them deal with the inter-conversion of $H_2O/H_2/O_2$ at an electrode, where electrons have to be efficiently injected/extracted at the possible highest rate.[1-3]

In this context, electrolyzers and fuel cells play a crucial role for the development of a sustainable society. Renewable hydrogen is seen as the optimal mean to connect these technologies,[3] as it is produced from water electrolysis (HER) and it can be subsequently consumed as fuel in FCs (HOR). On one side, $H_2$ generated from the reduction of $H_2O$ can be linked to renewable electricity (e.g. solar, wind, geothermal), to bio-driven devices (microbial cells, algae plants) or to artificial photosynthesis schemes. On the other end, hydrogen, as carbon neutral energy vector, is pivotal for FCs technology, or it can be used as primary fuel for generators and engines, or as chemical commodity for some major industrial processes like synthetic fertilizer or hydrocarbon productions. Huge research effort on renewable hydrogen economy should aim at an increased electrolytic efficiency coupled with broad flexibility of production and delivery, so to foster a pervasive technology integration.

The turning point is to be sought in the improvement of the electrocatalytic efficiencies for both HER and HOR. HER occurs by reduction of water at the cathode of a water-splitting device. In order to meet the device requirements, the efficiency and modularity of HER are mainly dependent on the electrocatalyst package. Pt is a very well-known, active, and durable catalyst for this reactions under various pH and temperature conditions, however Pt scarcity represents a big hinder for its employment on large scale.[4-7]  Moreover, its huge decrease of performances at neutral pH underlines the need for alternatives. The engineering of innovative

cathode composites able to tackle efficient HER at neutral pH is then required, since these are the operating conditions of some highly promising technologies such as MECs, PEC device or solar water splitting through bio-inspired artificial photosynthesis.[8,9] For these technologies the most suitable pH values are not determined by electrocatalytic performance, but rather by semiconductors' or bacteria' stability, some of which only exhibit strong performances in neutral conditions.

In general, the behavior of electrocatalysts at neutral pH is not well investigated. Also for Pt, the most studied material, only recently have appeared some comprehensive works analyzing HER and HOR activities and kinetics.[10-13]

A common feature of HER electrocatalysts is the levelling of performances in the pH range from 5 to 9. In Fig. **1.1a** it is shown how the onset overpotentials for HER of a Pt disk electrode deflect from the theoretical values between 5 < pH < 9. In this region the $\Delta E'$ shift of -59 mV/pH as derived from Nernst equation is not observed and the overpotentials attain a constant value. At pH above the threshold value, pH = 9, Pt recovers the ideal trend. This behavior has been ascribed to a switching in the intrinsic mechanism of HER, and it has been rationalized both theoretically and experimentally.[12,13]
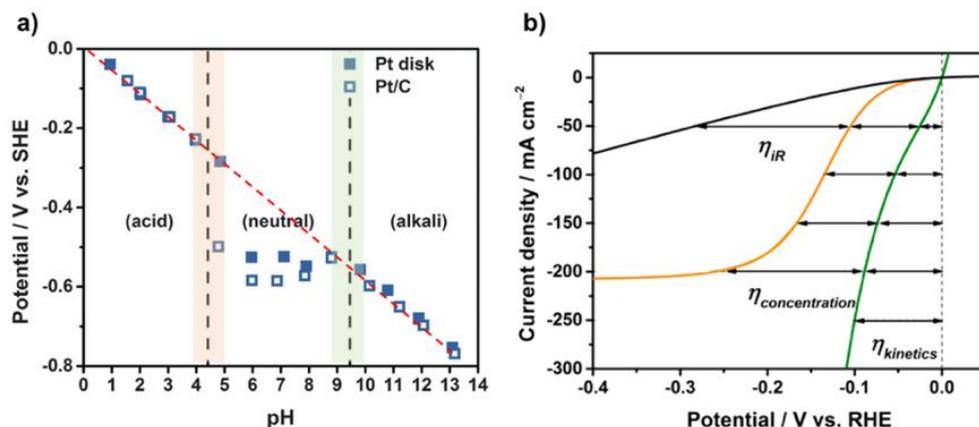


**Figure 5.1**: adapted from ref [12] and ref [13]. **a)** Effect of the pH on the onset of HER current. It is clear the deviation from the thermodynamic value of 59 mV/pH in the range 5 < pH < 9, where the reactant switching between $H^+$ and $H_2O$ occurs. **b)** Polarization curves for a Pt electrode, rotated at 1600 rpm and immersed in a 1 M PB solution. The contributions to the overall overpotential ($\eta_{tot}$) due to slow kinetics ($\eta_{kin}$), depletion of reactants from the electrode surface ($\eta_{conc}$) and uncompensated resistance ($\eta_{iR}$) are shown.

HER proceeds via subsequent elementary steps that may or may not involve the exchange of electrons at the electrode surface. They are usually known as the Volmer (Eq. **1.1a**), Heyrovsky (Eq. **1.1b**) or Tafel (Eq. **1.1c**) steps.

$$H_2O \rightleftharpoons H^+ + OH^- + e^- \rightarrow H_{ads} + OH^- \qquad \text{Eq. } \mathbf{1.1a}$$

$$H_{ads} + e^- + H_2O \rightarrow H_2 + OH^- \qquad \text{Eq. } \mathbf{1.1b}$$

$$2H_{ads} \rightarrow H_2 \qquad \text{Eq. } \mathbf{1.1c}$$
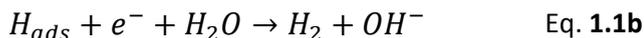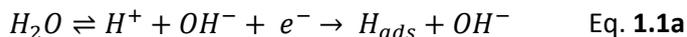
Depending on the pH at which the reaction is carried out, (acidic, pH < 5 or basic/neutral, pH > 5) protons or water molecules are considered as the "true" reactants in the Volmer and Heyrovsky steps. The sharp change of the trend in Fig. **1.1a** at pH = 5 was indeed regarded as a switching of the reactants from $H^+$ to $H_2O$. The former has faster kinetics, while the reduction of the latter is much slower and requires at neutral pH higher overpotential to occur, that are in turn associated to high energy losses. However, other interpretations have been proposed.[14] Despite the simplicity of the reaction (HER is often taken as a model example of electrode kinetics) after decades of studies there is still a debate about the real mechanism of HER at different pH.[15] A recent, very detailed, work based on experimental results, supported the thesis that regardless of the pH, HER should proceed via the reduction of protons, produced in basic solutions by water dissociation (left end of Eq. **1.1a**). The same mechanism would then describe HER even at very different pH, with a fundamental contribution of the $H_{ads}$ intermediate formation, whose binding energy is referred as the unique descriptor of HER.[14]

All the mentioned works, however, share a common point, that is the limited availability of protons at neutral pH at the electrode surface. This obvious fact limits the kinetics and generates high concentration overpotentials ($\eta_{conc}$). As outlined by Takanabe,[12,13] and Mayrhofer,[10,11] HER around neutral pH can be strongly affected by a number of possible factors: local pH changes, $\eta_{conc}$ , and, if the solution is buffered (e.g. PB), also from buffer concentration. In unbuffered electrolytes the reduction of protons/water induces modification of the effective surface pH, i.e. within few micrometers from the surface, then altering the kinetics. The use of buffers can eliminate this effect, but also protonated and deprotonated buffer species are involved in HER and can generate $\eta_{conc}$ as high as 50% of the total amount, $\eta_{tot}$ . $\eta_{tot}$ is defined as ($\eta_{tot} = \eta_{iR} + \eta_{kin} + \eta_{conc}$ ) where $\eta_{kin}$ is the kinetic overpotential and $\eta_{iR}$ is the overpotential due to uncompensated resistance. In Fig.

**1.1b** the contributions of each $\eta_i$ term on $\eta_{tot}$ at neutral pH at a Pt disk electrode are shown. From the plot it is evident how $\eta_{kin}$ is only slightly affecting HER activity, with the highest detrimental effects coming from $\eta_{conc}$ and $\eta_{iR}$.

Since HER at neutral pH is more limited by "external" factors other than the electrocatalyst itself, it is then desirable to develop new systems, more abundant and more scalable than Pt electrodes, that may promote sustainable HER under mild conditions. This task can be accomplished by the rational design of nanostructured materials able to increase the rate of HER improving the formation of intermediate species ($H_{ads}$). A possible strategy is envisaged in the promotion of water dissociation, $H_2O \leftrightarrows H^+ + OH^-$, reaction that precedes the electrochemical step of $H_{ads}$ formation via proton reduction ($H^+ + e^- \rightarrow H_{ads}$). Promoting water dissociation, hence the availability of free protons, would then speed up $H_{ads}$ formation, a key step for the overall HER process. If one succeeds in increasing the availability of protons at the surface at neutral pH, the electrocatalytic HER would be improved. Markovic and coworkers[16] have shown that HER activity on state-of-the-art Pt metal can be increased 8 times thanks to the controlled arrangement of 3D $Ni(OH)_2$ nanoclusters onto the Pt surface that are able to promote water dissociation in alkaline media. The authors related the increased activity to a bifunctional effect of $Ni(OH)_2$, whose edges would promote both water dissociation and the production of $H_{ads}$ intermediates that would then recombine on the nearby Pt surfaces to give $H_2$ in a more efficient way. With an analogous approach, the same group reported also how HOR can benefit from the improved adsorption of reaction intermediates.[17]

In this chapter is presented an innovative strategy to improve the rate of HER at neutral pH by means of a carbon-based mixed organic-inorganic nanocomposite. Taking inspiration from the above works, the electrocatalyst consists of a hierarchical structure in which a mesoporous shell of nanocrystalline titanium dioxide is able to promote the efficient water dissociation reaction, while Pd nanoparticles and multiwall carbon nanotubes cooperate to lead to an overall remarkable activity for HER at neutral pH.

## 1.1 Nanostructures for H$_2$ Evolution Reaction

In order to catalyze HER at near-neutral pH it is here reported the study of carbon-based nanostructures, a particular class of nanocomposite materials. Focus of the work is the electrochemical characterization of these electrocatalysts, that are able to capitalize several advantages of nanotechnology, like the possibility to tailor the design of nanometric assemblies.

This work was developed within the "Nanosolar" project, funded by the Italian Ministry of Education, that aimed at the development of efficient platforms for energy conversion applications. In the project have been involved several research groups, among those the *Carbon Nanotechnology Group (CNG)* of Prof. Maurizio Prato and the *Materials, Environment and Energy (MEE)* group of Prof. Paolo Fornasiero, both at the University of Trieste, that carried out the synthesis and part of the physical characterization of the electrocatalysts herein studied.

A schematic image of the investigated nanocomposites, generically labelled MWCNTs@M/oxide, is given in Fig. **1.2**, together with the design strategy that is basically a combination of ex-situ and in-situ methods.
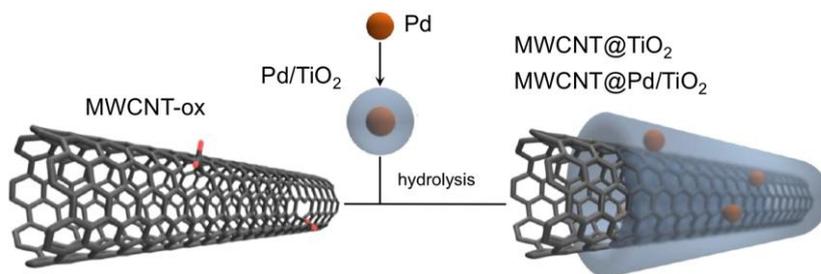


**Figure 1.2**: scheme of the synthetic procedure for the production of the electrocatalyst **MWCNT@Pd/TiO$_2$** and the model systems **MWCNT@TiO$_2$** and **Pd/TiO$_2$**

The synthesis of the resulting MWCNTs@M/oxide structures involved the use of three building blocks, namely oxidized MWCNTs (MWCNTs-ox), functionalized metallic particles and a metal alkoxide, the precursor of the oxide shell.[18] Specifically, the resulting nanocomposite is formed of core–shell metal@oxide particles supported on conducting MWCNTs. This approach is highly flexible and

versatile, and enables to tune both the composition and concentration of all the components, as well as the thickness of the oxide layer surrounding the MWCNTs. By the rational design of these nanostructures metal NPs like Pd and Pt, or oxides like $TiO_2$, $ZrO_2$, $CeO_2$ can be easily grown at choice, depending on the desired properties of the final materials.

In this Chapter the electrochemical activity of **MWCNT@Pd/TiO₂** are reported and discussed, together with those of the two related model systems **Pd/TiO₂** and **MWCNT@TiO₂**. The former model allows to address the effects of MWCNTs, while the latter to specifically discern the activity of the nanocomposite in the absence of Pd NPs, that are the catalytic cores where HER is supposed to occur.

In the next Chapter that focusses on the electrochemical $CO_2$ reduction, will be presented similar nanoarchitectures that contain a different oxide shell, namely $CeO_2$. Changing the oxide from $TiO_2$ to $CeO_2$ strongly affects the properties of the electrocatalyst, that is however also strongly influenced by the interaction of the oxide shells with the wrapped MWCNTs.

The essential idea for the preparation of **MWCNT@Pd/TiO₂** is that the functionalized Pd particles and the MWCNTs bind to the Ti-alkoxide thanks to the presence of carboxyl groups on the MWCNTs that displace the weak alkoxide ligands. In the first step, the $Pd/TiO_2$ building blocks are prepared by reacting Pd particles (1% wt.) with the Ti-alkoxide. The so-formed $Pd/TiO_2$ particles are then connected to the MWCNTs (20% wt.) by reaction of the MWCNTs with the alkoxide linkages that remain available on the $Pd/TiO_2$ particles. This supramolecular ensemble is subjected to a controlled hydrolysis of the remaining alkoxide groups to obtain uniform **MWCNT@Pd/TiO₂** composites, that were finally allowed to dry at 180°C. The method is easy to implement by simply placing the three building blocks in appropriate solvent mixtures (see ref. [18] for further details). The resulting **MWCNT@Pd/TiO₂** present a shell of $TiO_2$ in the order of 10-15 nm, with Pd NPs homogeneously dispersed within the oxide matrix. The mesoporosity of $TiO_2$ allows a good exposure of the Pd catalytic cores to the electrolyte, ensuring an optimal architecture for HER to occur.

As will be outlined later in the Chapter, the effects of a thermic treatment both on the physico-chemical and electrochemical properties will be evaluated. The samples underwent a calcination procedure from RT to a value of 250°C for 5 hours, with a heating ramp at 3°C/min and a cooling down at 4.5°C/min.

Within this thesis, another parameter that involved a change in the synthetic procedure has also been varied, namely a different chemical functionalization of the MWCNTs building block. The carboxyl groups present on MWCNTs are fundamental to template the growth of $TiO_2$, and to this end it was evaluated the effect of a different separation between the carboxylic groups and the carbon nanotubes. This has been accomplished by functionalization of MWCNTs either *i)* with carboxylic groups directly attached on the carbon scaffold, or *ii)* with benzoic functionalities in which the carboxylic groups are separated from the MWCNTs by phenyl moieties.

The first functionalization has been obtained by chemical oxidation of the MWCNTs using a 3:1 mixture of concentrated $H_2SO_4$ and $HNO_3$, while the benzoic moieties have been attached using diazonium chemistry, following the approach proposed by Tour.[19] As mentioned, the carboxylic groups are necessary to template the in-situ growth of the $TiO_2$ shell. Using the "Tour-method" a more uniform functionalization of the MWCNTs was achieved, that in turns gave a more homogenous coverage of the oxide. The effects of such different functionalization are highlighted in section **xxx**.

The various nanocomposites, both **MWCNT@Pd/TiO₂**, the metal-free **MWCNT@TiO₂** and **Pd/TiO₂** have been thoroughly characterized by means of HR-TEM and Raman, XPS, TGA, UV-Vis spectroscopy and BET adsorption, not shown in this work except for some relevant HR-TEM images reported in Fig. **1.3** (further information can be found on ref. [18]) and an Electron Tomography in Fig. **1.4**. Other characteristics of **MWCNT@Pd/TiO₂** such as BET areas and pores' volume and diameters are summarized in Table **1.1**.
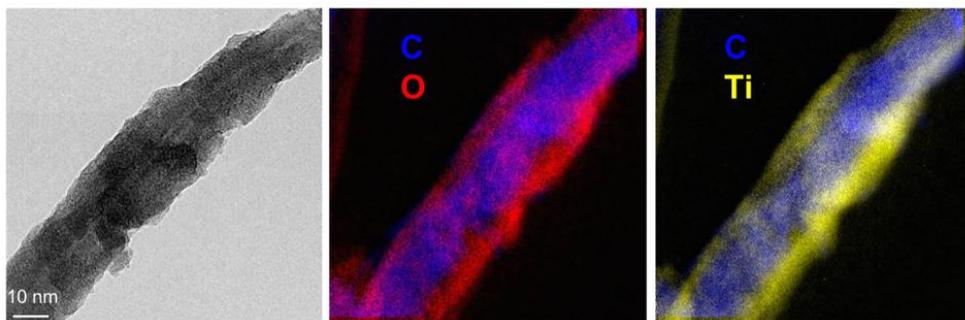
**Figure 1.3**: Representative High-Resolution Transmission Electron Microscopy image of **MWCNT@Pd/TiO₂**. **a)** Zero-Loss Energy-Filtered TEM (EFTEM). **b)** and **c)** EF-TEM images which highlight the chemical composition of the oxide shell around the MWCNTs. Courtesy of Lucia Nasi (IMEM-CNR, Parma).

| Sample | Surface area (m²/g) | Pore Volume (mL/g) | D$_{max}$ (nm) |
|---|---|---|---|
| Pd@TiO₂ | 325 | 0.23 | 3.8 |
| MWCNT@Pd/TiO₂ | 172 | 0.25 | 47 |

**Table 1.1:** characteristics of the nanocomposite **MWCNT@Pd/TiO₂** and the building block **Pd/TiO₂** as determined by BET measurements.
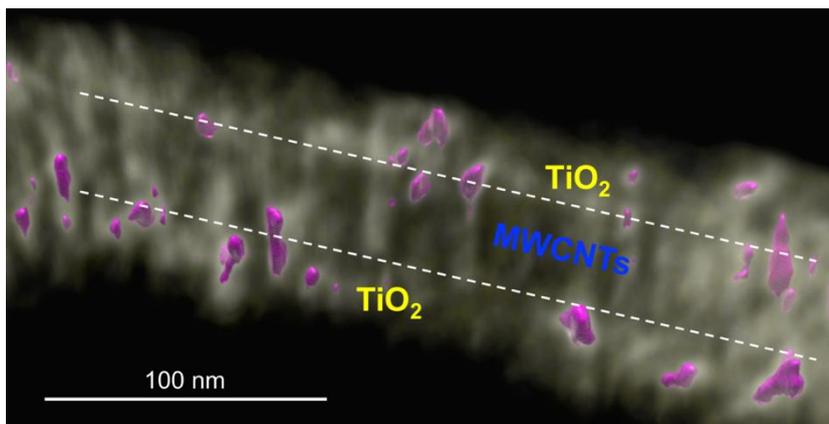


**Figure 1.4**: Electron Tomography image of **MWCNT@Pd/TiO₂**. The purple spots are the Pd NPs embedded within the mesoporous TiO₂ shell. Courtesy of Lucia Nasi (IMEM-CNR, Parma)

Fig. **1.3a** shows a representative HR-TEM image of **MWCNT@Pd/TiO₂** in which is possible to see a homogeneous coverage of the MWCNTs. The chemical nature of the shell has been investigated by EELS analysis (Fig**. 1.3b** and **1.3c**), which revealed

the presence of Ti and O atoms around the C-backbone, confirming the uniform coverage of TiO$_2$. As it will be shown later in the Chapter, the regular coverage of MWCNTs will allow to rationalize the properties of the MWCNTs-TiO$_2$ interface on the basis of EIS results. Such interface is fundamental in governing the electrocatalytic activity of the nanostructures. The electron tomography image of Fig. **1.4** provides an overall picture of the **MWCNT@Pd/TiO$_2$** nanostructure; here the three building blocks are clearly visible, even the Pd NPs embedded within the TiO$_2$ shell.

### 1.1.1. MWCNTs

The electronic properties of MWCNTs are very well known,[20] and their employment in the field of electrocatalysis has been shown to be extremely beneficial. The activity of heterogeneous and homogeneous catalysts (when attached on MWCNTs) can be improved by the interaction with the carbon structure.[21-23] Numerous examples are reported, where the activity for HER,[24] OER,[25] ORR,[26] is promoted by the presence of MWCNTs. However, it is not always clear the way MWCNTs promote the mentioned reactions, whether by simply providing a high specific surface area for the catalysts (then without affecting the reaction rate), or for their high electronic conductivity, or because they can increase the reaction rate (by electronic effects, presence of catalytic impurities, etc.) or finally by a combination of all of the above.[27] In this study, MWCNTs have been originally chosen to increase the conductivity of the nanostructures, since that of the TiO$_2$ shell is not optimal. Moreover, they also play a structural role since they provide during the synthesis the skeleton around which the shell of oxide is grown, and the very high aspect ratio has been shown to be fundamental to achieve mesoporous oxide shells with nanometric thickness. As will be shown, however, the beneficial effects of MWCNTs go well beyond those initially hypothesized, and contribute to improve significantly the electronic properties of TiO$_2$ thus resulting in better performance of the catalytic system.

### 1.1.2. Pd

Platinum is the HER electrocatalyst of choice thanks to its optimum tradeoff between adsorption and desorption of reaction intermediates. In the field of

catalysis it is widely accepted the concept that "*in media stat virtus*" incorporated within the Sabatier's principle. Volcano-shaped plots are commonly used to evidence that the best catalytic activity is achieved when the effects of a given descriptor are rightly balanced.[28,29]

In the case of HER, the binding energy of hydrogen atoms on the electrode surface ($H_{ads}$) is widely accepted as the main descriptor; a neither too weak nor too strong H adsorption is needed to obtain the optimal HER activity. This is valid at any pH and in Fig. **1.5a** the trend of HER current is shown as a function of H binding energy for several metal surfaces in basic solution. As it can be seen from Fig. **1.5b**, the highest activity is found for Pt, with Pd, however, being the best alternative. As mentioned, at these pH values, as well as at neutral pH, $H_{ads}$ formation is a key step of HER. Therefore, optimizing $H_{ads}$ formation is likely to translate in better performances. For this reason, Pd represents an optimal choice and it is chosen as the active catalytic core for the nanostructures studied in this work.
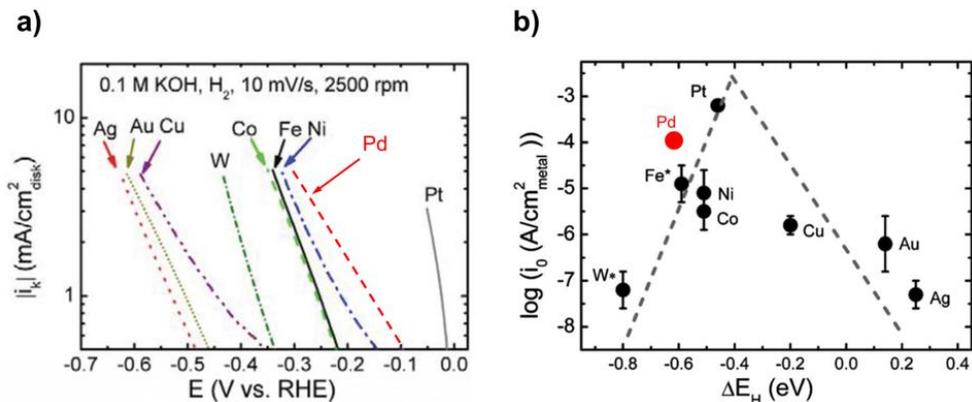


**Figure 1.5**: **a)** Tafel plot in base (KOH) for various metal electrodes. The exchange current density derived by extrapolation at $E_{RHE}= 0V$ are plotted in panel b). **b)** Plot in which the exchange current density for the metals in panel a) is plotted against the binding energy of $H_{ads}$ on the metallic surface. A classical Volcano relation occurs, with Pd, highlighted in red, being the best metal after Pt. Adapted from ref. [30]

This approach has also the advantage to replace Pt with a more abundant metal.[31] Even if still precious and rare, Pd is extensively used in car converters and it can be reconverted from exhausted spare parts. Moreover, it has the additional advantages to be nontoxic or un-allergenic by contrast with other investigated systems, such as Ni-based catalysts.

### 1.1.3. TiO$_2$

As sketched in the previous section, fostering water dissociation at pH in which the availability of free protons in solution is limited, is bound to translate in better HER activity;[16] HER is thought to involve the H$_{ads}$ intermediate at any pH, and a higher local concentration of H$^+$ is clearly expected to allow an easier formation of H$_{ads}$.

Metal oxides are in general rather effective for the water O–H bond cleavage but they are pretty poor in promoting the recombination of the resulting H$_{ads}$ intermediates to H$_2$.[32-34] Therefore, optimal HER catalysts can be designed by combining metal oxides with the catalytic proficiencies of metals, creating bi-functional M/MOx systems.[35,36] With this respect, core idea of this work is to improve HER increasing water dissociation onto the TiO$_2$ shell. Water adsorbs both dissociatively and molecularly on TiO$_2$ surfaces, with the binding that occurs at the acidic fivefold coordinated Ti$^{4+}$ sites.[37] The bonding with the surface weakens the water O-H bonds thus favoring the release of protons in solution. This situation would generate a higher local concentration of H$^+$ that together with the concomitant presence of Pd NPs where H$_{ads}$ formation can easily occur, would give to the nanostructures desirable attributes. It is also not to exclude that the TiO$_2$ surface itself may vehicle protons to the Pd NPs in a sort of spill-over mechanism.

### 1.2 Electrochemical characterization of MWCNT@Pd/TiO$_2$

The electrocatalyst **MWCNT@Pd/TiO$_2$** as well as the model systems **MWCNT@TiO$_2$** and **Pd/TiO$_2$** have been characterized in a neutral PB 0.1 M aqueous solution. The solutions have been freshly prepared before each experiment by mixing appropriate amounts of the mono- and di-hydrogen phosphate salts Na$_2$HPO$_4$ and NaH$_2$PO$_4$·2H$_2$O. The pH of the resulting solutions is pH = 7.4.

Electrochemical experiments have been carried out in a three electrode PTFE cell at the bottom of which is placed the working electrode, usually a SPE. As counter electrode a platinum spiral is used, and as reference electrode a Ag/AgCl (3M). Potentials, if not otherwise specified, are always reported in the Reversible Hydrogen Electrode scale (E$_{RHE}$ = E$_{Ag/AgCl}$ - 0.21 V -0.059*7.4 = E$_{Ag/AgCl}$ -0.65 V). The SPE electrode is properly isolated from the external with on O-ring that is tightened into the body of the PTFE cell with two connecting screws. Before each measurement the solutions have been degassed for at least 20 minute with Ar to

ensure a complete removal of dissolved $O_2$. When a GC working electrode was used a standard three-electrode electrochemical cell was employed.

Thin films of **MWCNT@Pd/TiO₂**, **MWCNT@TiO₂** and **Pd/TiO₂** are prepared by drop-cast of the respective powders from methanol suspensions (1.6 mg/ml) directly on the SPE substrates. 100 μl of the various suspensions are deposited with 10x10 μl aliquots, resulting in a total catalyst loading of 80 μg (the electroactive area of the SPE does not account for the entire area of the substrate) and 0.8 μg of Pd.

For the sake of simplicity, the electrochemical characterization has been divided into two main sections that report respectively the effects of *i)* a different functionalization of the MWCNTs skeleton and *ii)* a thermic treatment of the samples.

## 1.2.1 Effect of a different MWCNTs-functionalization on the electrochemical properties of MWCNT@Pd/TiO₂.

The nanocomposites contained MWCNTs that were functionalized via either chemical oxidation or the "Tour-method"; they are labelled **Ox-MWCNTs@Pd/TiO₂** and **Tour-MWCNTs@Pd/TiO₂** respectively. Their electrochemical characterization by LSV under conditions of HER is reported in Fig. **1.6**, where the behavior of the **Pd/TiO₂** model system and of the bare GC electrode are also shown. As it can be seen in Fig. **1.6a**, the observed electrocatalytic activity is related to the different organic functionalization, highlighting the importance of the MWCNT/TiO₂ interface. The catalytic onset for the HER at the **Ox-MWCNTs@Pd/TiO₂** and **Tour-MWCNTs@Pd/TiO₂** electrode is located, respectively, at ∼ -0.15 $V_{RHE}$ and ∼ -0.25 $V_{RHE}$, while overpotentials of -0.33 V and -0.37 V are needed to reach an arbitrary cathodic current threshold of 1.25 mAcm⁻² (corresponding to a hydrogen evolution rate of 80 μmol·h⁻¹·cm⁻²).

The CA experiments in Fig. **1.6b** reveal steady state currents that increase exponentially with the applied potentials; the integrated charge obtained from such CA experiments were used to estimate the TOF for the various systems under investigation (see section **1.2.1.3.**). In Fig. **1.6b** CA for **Ox-MWCNTs@Pd/TiO₂** and the metal-free model system **Ox-MWCNTs@TiO₂** are reported. A comparison of the two systems enables to decouple the contribution of Pd NPs to HER by integration of the "net" current.
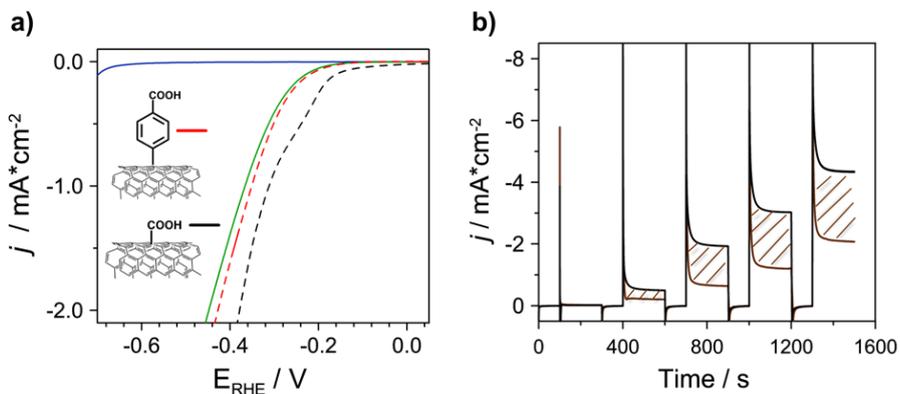
**Figure 1.6**: **a)** LSV at 2 mV/s for **ox-MWCNT@Pd/TiO₂** (black dashed line), **Tour-MWCNT@Pd/TiO₂** (red dashed line), **Pd/TiO₂** (green solid line) and a bare GC electrode (blue solid line) in an Ar-saturated PB 0.1 M, pH=7.4. **b)** CA of **Ox-MWCNT@Pd/TiO₂** (black line) and **Ox-MWCNT@TiO₂** (brown) in the same electrolyte at increasing potentials: -0.5, -0.98, -1.16, -1.23 and -1.3 V vs. Ag/AgCl 3M. Potentials are iR-corrected. The net contribution due to Pd NPs is highlighted by the brown stripes.

In order to realize a comparative description of the intrinsic activity of different catalytic systems, possibly characterized by very different surface extensions, it is opportune to use a procedure that is insensitive to topological factors and that focusses as much as possible on the properties of the active sites. In homogeneous catalysis comparison of catalysts' activity is usually done by measuring the TON (number of catalytic cycles sustained by a catalyst) and TOF (an indicator of the rate at which the reaction proceeds). TON is usually determined by quantification of the reaction products, normalized then by the amount of catalyst present, while TOF is simply the TON/time, indeed a frequency. In the field of heterogeneous catalysis, it is more common to report mass-normalized and/or surface-normalized activities that have the disadvantage to measure a "bulk" quantity. However, this approach is not always the best choice for nanostructured systems, where the high anisotropy and the possible presence of cooperative effects may give rise to local different activities, whose presence would not be detected with the mentioned methods. For this reasons, *in-situ* methods of surface characterization have been developed and are particularly useful to characterize surfaces' reactivity.

In electrocatalysis it is common to report geometric current densities. This approach even if easy and straightforward is not good to discern information about the real activity of the catalytic sites because it neglects the contribution of surface roughness, and then should be discarded. For a first evaluation, a geometric area

normalization can be used, as in Fig. **1.6a**, but more accurate methodologies are recommended.

To this end for examples the activity of Pt-based catalysts like Pt/C is often reported taking into account the so-called ECSA, Electrochemical (Active) Surface Area, usually measured by integration of adsorption/desorption processes on Pt. Normalization by ECSA can give much more information then simple mass-normalization and reveal for example that only about 20% of the total amount of Pt present on a state-of-the-art Pt/C catalyst is electrochemically active. The remaining Pt is not "seen" by the solution and then useless to drive HER/HOR.[38]

Given the difficulty to find a unique and valid methodology for nanostructured electrocatalytic systems, in these work it has been developed a new approach for TON and TOF calculation that is particularly suited to compare the materials studied in the present thesis. Doing this, it has been possible to get information about the role of each building block and to evaluate the effects of the various treatments (calcination and different functionalization). The strategy here adopted is entirely electrochemical, and the derivation of the various factors that influence the TOF is simply obtained by classical CV and CA techniques, together with a SECM-based approach to determine the Faradaic Efficiency.

The TON (=moles of product/moles of catalyst) and TOF (=TON/time) are calculated relating the "moles of product" to the charge exchanged during each potential step in the CA experiments, and the "moles of catalyst" to the amount of electroactive catalyst. The moles of products considered are those produced only by the active Pd sites, and this is the reason why at the top of Eq. **1.2a** is considered the contribution of the metal-free model system **Ox-MWCNTs@TiO₂** and its charge subtracted from that of **Ox-MWCNTs@Pd/TiO₂**. The same apply for **Tour-MWCNTs@Pd/TiO₂** and **Tour-MWCNTs@TiO₂**. The so-obtained turnover number is weighed for the F.E. of the HER as determined by SECM. The procedure is explained in detail in the next section. Doing this, it is possible to normalize the activity on an electroactive area basis, like the ECSA previously mentioned, obtaining an intrinsic descriptor of the electrocatalytic activity.

$$TON_n = \frac{Q^{H_2}_{n,MWCNT@Pd/TiO_2}(C) - Q^{H_2}_{n,MWCNT@TiO_2}(C)}{Q_{Pd}(C)}(F.E.) \qquad \text{Eq. } \textbf{1.2a}$$

$$TOF_n(h^{-1}) = \frac{TON_n}{time\ (h)} \qquad \text{Eq. } \textbf{1.2b}$$

where $Q^{H_2}_{n,MWCNT@Pd/TiO_2}$ is the charge integrated from CA experiments with **MWCNTs@Pd/TiO₂** at each potential n, $Q^{H_2}_{n,MWCNT@TiO_2}$ is the contribution of the metal-free **MWCNTs@TiO₂** and $Q_{Pd}$ is the normalization factor for the amount of electroactive **Pd** as determined by CV (integration of the redox peak related to the reaction: Pd + 2OH⁻ → PdO + H₂O + 2e⁻). Time is the duration of each potential step and $(F.E.)$ is the Faradaic Efficiency for hydrogen evolution, revealed to be constant at different applied potentials.

## 1.2.1.1. Faradaic efficiency (F.E.) quantification.

The evaluation of the TON and TOF for the various electrocatalysts studied in this work can be directly evaluated from the cathodic currents measured at the conducting substrate, once the faradaic efficiency of the process is known.

In order to determine the F.E. of the cathodic process, it is taken advantage of an experimental procedure based on the use of the SECM, operated in the so-called SG (substrate generator)/TC (tip collection) mode. This setup has ben recently described for the rapid and high throughput screening of various electrocatalysts,[39] e.g. for ORR.[40] For our purpose, the main advantage of this technique is the ability to position with micrometric precision an ultramicroelectrode (UME) probe tip very close to the electrode surface (the substrate, i.e. the various electrocatalysts) and therefore the possibility of investigating electrocatalytic surfaces of very small extension.[41] In this case the probe is a Pt UME anode, biased at 0.2 V (vs Ag/AgCl) so as to measure the hydrogen evolved from the underlying substrate by HOR (H₂ → 2H⁺ + 2e⁻), in a typical generator-collector configuration.[42] To highlight the effectiveness of the H₂-probe, in Fig. **1.7a** is reported the simultaneous detection at the tip of the hydrogen evolved at the substrate during a voltammetric scan. It can be seen that the setup is able to capture H₂ also when it is dynamically generated during CV, but for a more rigorous quantification it is preferred to measure F.E. under steady conditions. For the purpose of this work, the substrate was then biased at η = -0.4 V in order to promote substantial HER, but F.E. have also been obtained at lower overpotentials.

From the ratio between the current density measured at the tip (j_tip, HOR current) and at the substrate (j_sub, HER current), the F.E. is then obtained using specific

working curves, that define the maximum collection efficiency (CE_max) for different experimental set-up (Eq. **1.3**).[40]

$$FE = \frac{j_{tip}/j_{sub}}{CE_{max}}$$

Eq. **1.3**

Some important geometric parameters cooperate together to define the working curve CE_max (Eq. **1.4**), such as the tip radius ($a$), the substrate radius ($b$) and the tip-substrate distance ($d$). Another very important parameter is the RG of the tip, i.e. the ratio between the diameters of outer glass tube and of the inner Pt disc UME. This parameter makes the expression of CE_max clearly dependent on the specific experimental set-up used (i.e. dimension of the used tip). In this specific case, a Pt disc UME ($a$ = 15 µm) embedded in glass ($\emptyset_{EXT}$ = 110 µm, RG = 3.66) was located at a given tip-substrate distance above the center of the substrate electrode in an Ar-saturated PB (pH 7.4) where it was used to collect the electrogenerated hydrogen. The substrate electrode (generator) was a disc UME (radius 12.5 µm) on which films of the electrocatalysts were deposited by drop-cast. This ensemble is embedded in a PDMS membrane and tightened at the bottom of a Teflon cell with an O-ring.

$$CE_{MAX} = 103.38 - 2.1681 * \left(\frac{d}{a/b}\right) + 0.02585 * \left(\frac{d}{a/b}\right)^2 - 0.0001485 * \left(\frac{d}{a/b}\right)^3 +$$
$$0.000000322 * \left(\frac{d}{a/b}\right)^4$$

Eq. **1.4**

It is to note that the coefficients of Eq. **1.4** have been optimized for SECM tips with an RG ratio between 3 and 6, as in our specific case (3.66).[40] While ($a$) and the RG ratio of the probe are easily obtained by optical inspection of the UME, an experimental procedure has to be devised in order to measure the substrate radius ($b$). This is required for the fact that the MWCNTs films extend laterally beyond the area of the underlying UME Pt disc on which they are deposited and ($b$) will therefore also depend on the porosity and conductivity of such films, i.e., on the percolation length of the nanotubes network. A first estimation of the electroactive surface area was then obtained by comparing the steady state current relative to the oxidation of 1 mM ferrocenemethanol (FcMeOH) measured at the substrate electrode before and after deposition of the electrocatalyst films. In Fig. **1.7b** the corresponding CVs are shown. The presence of the nanostructured film caused an

increase of the stationary currents by more than 20 times. Given the proportionality between current and electrode surface area, this correspond to a ~4-fold increase of the "electrode diameter", resulting in an effective radius for the substrate electrode ($b$) = 50 μm.
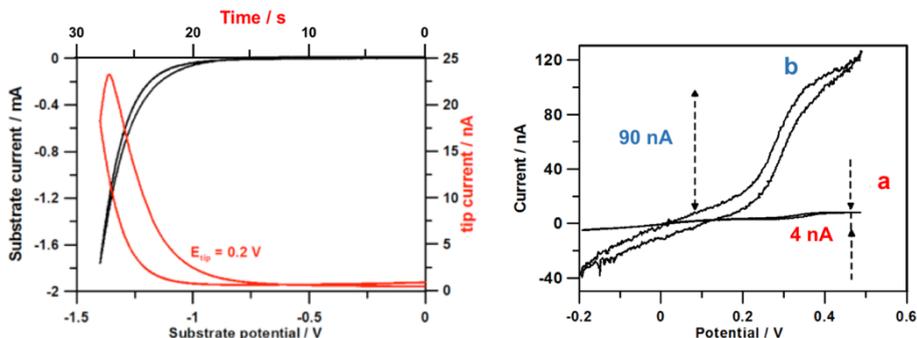


**Figure 1.7. a)** On-line detection of the Hydrogen evolved at the substrate during a CV scan (black curve) by the application of a constant potential at the tip ($E_{tip}$ = 0.2 V). The resulting i-t curve for the tip is plotted in red. **b)** CV curves of 1 mM Ferrocenemethanol for the substrate electrode ($\varnothing$ = 25 μm) before (a) and after (b) the modification with **f-MWCNT@Pd/TiO$_2$** in 80 mM LiClO$_4$ Ar-saturated aqueous solution. Scan rate 0.05 Vs$^{-1}$. Potentials are reported vs. Ag/AgCl/KCl 3M.

This is however just a crude approximation, since the electrical conductivity of the film depends on percolation paths that are not necessarily isotropically distributed, and the electrode area may in fact assume much more asymmetric shapes. Since this would affect the maximum tip collection efficiency, the electroactive surface area was therefore independently investigated by SECM, again in a SG/TC mode, to obtain an electrochemical image of the substrate electrode and confirm the circular shape of the substrate. The Pt tip (15 μm) is then positioned *via* feedback mode (see section **A.4.1.2** in the Appendix) in a 1 mM FcMeOH aqueous solution at about 25 μm above the sample (Fig. **1.8a**) and then scanned parallel to the substrate.
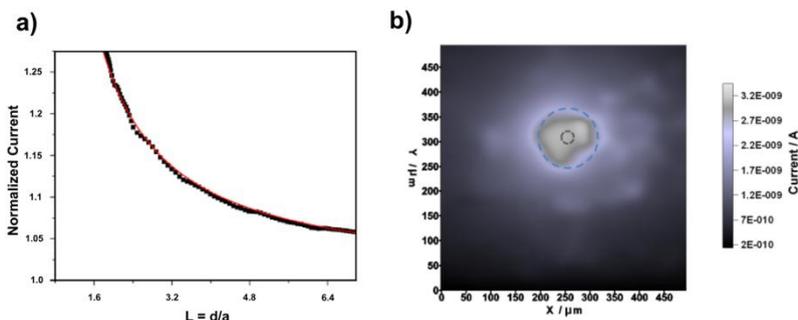
**Figure 1.8. a)** Approach curve in a feedback mode for the platinum tip microelectrode ($a$ = 15 μm ) in 1mM Ferrocenemethanol/80 mM LiClO$_4$ Ar-saturated aqueous solution. E$_{tip}$ = 0.4 V (vs. Ag/AgCl/KCl 3M). **b)** SG/TC in the same conditions that display the real substrate geometry after the deposition of **MWCNT@Pd/TiO$_2$**

The electrochemical image of the surface is obtained by oxidizing FcMeOH at the substrate (E$_{sub}$= 0.45 V vs Ag/AgCl) and applying at the tip a bias of 0 V (vs. Ag/AgCl), so as to detect the continuously generated FcMeOH$^+$. In Fig. **1.8b** is shown an image of the electroactive area where a nanostructured film is deposited on the substrate. As expected, and in line with the results of the above CV investigation, such area exceeds that of the underlying UME contact (indicated by the grey dashed circle with radius 12.5 μm) as a consequence of the very good conductivity of MWCNTs films. Moreover, the area individuated by SECM is quite symmetric and may be adequately approximated by an equivalent disc with radius 50 μm (indicated by the blue dashed circle), in very good agreement with the estimate by CV.

In order to determine the F.E. of the HER process on the electrocatalytic films, the SECM Pt tip ($a$ = 15 μm) was finally positioned above the center of the underlying electroactive area and then approached *via* feedback mode (using FcMeOH 1 mM as a redox mediator in 80mM LiClO$_4$) to a z-distance of about 25 μm from the film (corresponding to 50% of the bulk current). Subsequently, the solution was replaced with phosphate buffer, rinsed at least 10 times before the next measure, and the H$_2$ generated at the substrate (usually at E$_{sub}$ = -0.4 V$_{RHE}$) finally detected at the tip (as schematically shown in Fig. **1.9a**). The intensity of the current collected at the tip, as explained above, is affected by two factors: (*i*) CE$_{max}$ , which entirely depends on geometric characteristics of the SECM detection setup, and (*ii*) the F.E. of HER. CE$_{max}$ is calculated using Eq. **1.4** and compared to the measured J$_{tip}$/J$_{sub}$ ratio.

In Fig. **1.9b**, $CE_{max}$ (black dots and line) and the experimental collection efficiency obtained in SG/TC experiments (red dots and line) are reported as a function of the characteristic geometric parameter *d/(a/b)*. A comparison of the two functions allows to evaluate the F.E. of **MWCNT@Pd/TiO₂** for HER, that results to be in the order of 94 ± 3% for all the studied nanocomposites.
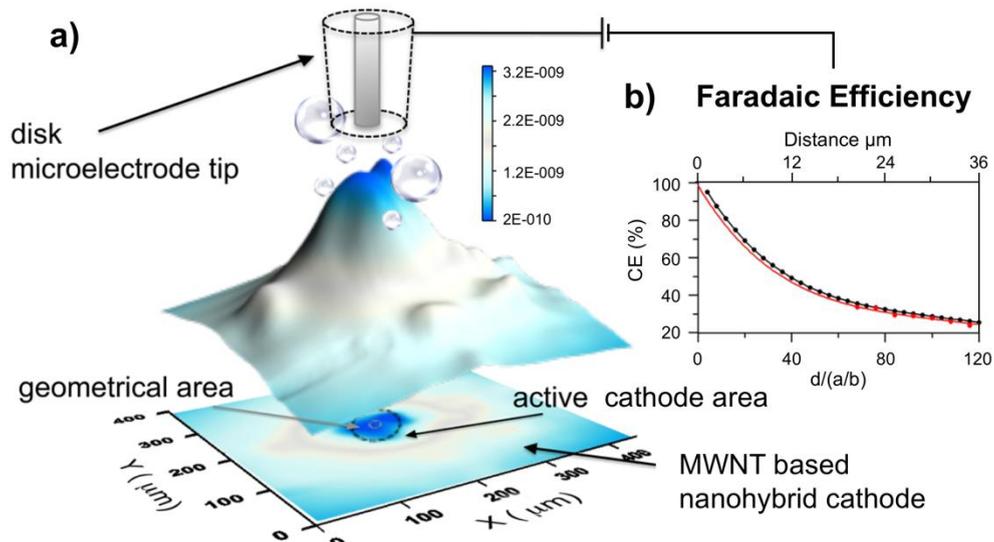


**Figure 1.9.** (**a**) schematic representation of the SG/TC experiment used to evaluate the faradaic efficiency of the cathodic process. Relevant geometric parameters: d = 25 μm is the distance between the tip and the substrate, a = 15 μm is the radius of the Pt SECM tip (embedded in a glass tube with an outer diameter of 110 μm, not in scale), b = 50 μm is the radius of the electroactive area of the MWCNT film. The underlying UME, used to contact the MWCNT film, is indicated in light grey. (**b**) experimental CE values (red dots) compared to the corresponding $CE_{max}$ values obtained from Eq. **1.4** (black dots and line). Experimental conditions: Ar-saturated PB solution (pH=7.4), $E_{tip}$ = +0.2 $V_{RHE}$, $E_{sub}$ = -0.4 $V_{RHE}$.

### 1.2.1.2. Palladium quantification ($Q_{Pd}$)

As previously described, in order to have a quantitative description of the catalytic activity through the calculation of the TOF, data needs to be normalized by the amount of electroactive Pd, the active site for HER. This entity has been estimated by CV in a 2 M NaOH aqueous solution. Scanning the potential within an appropriate potential window induces the formation of a surface Pd-oxide layer onto the Pd NPs, that in the present conditions occurs easily (Eq. **1.5**). The charge related to this process is then associated to the amount of Pd that is able to sustain a redox reaction. The classical H-UPD coulometry[43] in the case of nanoparticulate

systems does not always give defined peaks, so the PdO procedure has been chosen.

$$Pd + OH^- \rightleftharpoons PdO + H_2O + 2e^-$$  Eq. **1.5**
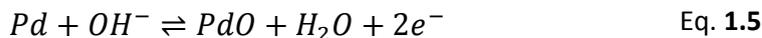
Integration of the charge underneath the PdO reduction peak (labelled with I in Fig. **1.10**) reveals the amount of electrochemically active Pd. The obtained charge for each electrocatalysts studied, is then used for TOF calculation and reported in Table **1.2**.
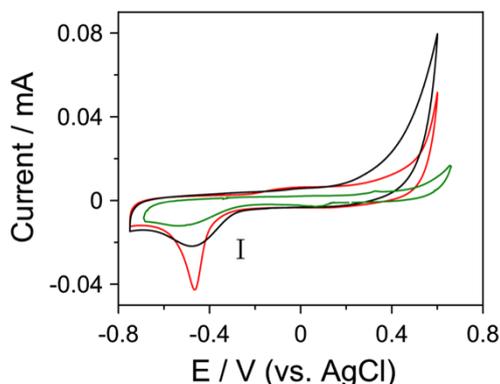


**Figure 1.10.** Representative CVs for Pd quantification in Ar-saturated NaOH 2 M at a scan rate of 20 mV/s. Films of **Ox-MWCNT@Pd/TiO₂** (black signal), **Tour-MWCNT@Pd/TiO₂** (black signal) and **Pd/TiO₂** (green signal) are drop-casted on SPEs with Ø = 4 mm. Peak I, the reduction of PdO, is integrated to get the charge of electroactive Pd.


### 1.2.1.3. TON/TOF determination.

By measuring for each electrocatalyst the above parameters, $Q_{Pd}$, F.E. and the charges from CA, the respective TON values at different applied potentials were then calculated by Eq. **1.2a**. The obtained values for **Tour-MWCNTs@Pd/TiO₂**, **Ox-MWCNTs@Pd/TiO₂** and **Pd/TiO₂** are summarized in Fig. **1.11**, which reports the potential dependence of the TON in the three cases. The Tafel-like behavior for all electrocatalysts demonstrates the good stability of the catalytic films and a well-behaved ohmic contact to the underlying conducting SPE substrate. Furthermore, extrapolation of the TON-η semi-logarithmic plots to zero overpotential provides the TOF₀ intercept value. The TOF₀ descriptor, i.e., the catalytic rate in the absence of any driving force, was introduced by Savèant et al. as an optimal descriptor of the intrinsic catalytic activity for homogenous catalysts.[44] The same concept is

here extended and applied to the case of heterogeneous catalytic materials with the procedure previously described. In a way, the $TOF_0$ resembles the exchange current density ($J_0$), a classical figure-of-merit in electrocatalysis that is also measured by extrapolation of Tafel plots.[45] The various fittings and $TOF_0$ values are also highlighted in Fig. **1.11** (colored circles).
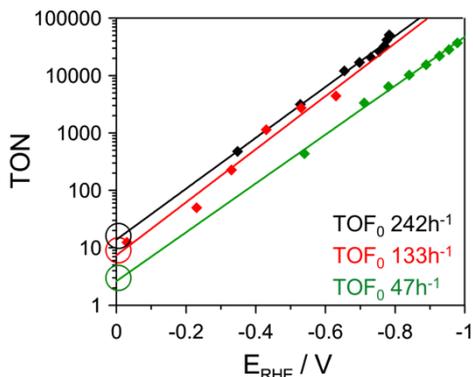


**Figure 1.11**: **a)** TON as a function of overpotential for **Ox-MWCNT@Pd/TiO₂** (black diamonds), **Tour-MWCNT@Pd/TiO₂** (red diamonds) and **Pd/TiO₂** (green diamonds). $TOF_0$ values are extrapolated at $E_{RHE} = 0$ V and are obtained from TON/time.

The TON and $TOF_0$ values for **Tour-MWCNTs@Pd/TiO₂** ($TOF_0 = 133$ $h^{-1}$) and **Ox-MWCNTs@Pd/TiO₂** ($TOF_0 = 242$ $h^{-1}$) are not very dissimilar, even if the activity of **Ox-MWCNTs@Pd/TiO₂** remains consistently higher in the entire potential region. Their behavior is similar to what observed by LSV (Fig. **1.6a**), where **Ox-MWCNTs@Pd/TiO₂** was the most active displaying lower overpotential ( ~70 mV) at a given threshold current. However, after taking into account all the various factors previously outlined, the performance gap between the two nanocomposites is not that high. The different activity seen by LSV likely arise from a lower availability of Pd in the **Tour-MWCNTs@Pd/TiO₂** samples. A simple normalization by the geometric area does not remove this possible intrinsic incongruence, whose contribution is finally overcome with this approach and lead to a reduction of the gap with **Ox-MWCNTs@Pd/TiO₂**. In the case of **Pd/TiO₂**, however, the much lower performances than the C-based nanostructures observed by LSV still persist, and a significantly lower $TOF_0$ value of 47 $h^{-1}$ is measured. This fact is a first indication of the important role played by the carbon backbone in promoting the catalytic activity of the metal nanoparticles. This fundamental contribution of the MWCNTs will be exhaustively investigated in the next section

by EIS. Finally, films obtained from physical mixtures of **MWCNTs@TiO₂** and **Pd/TiO₂** led to much worse electrocatalytic activities accompanied by significantly higher capacitive currents (not shown), thus highlighting the synergic effects and advantages deriving from the nanoscale integration of the two components in both the **Tour-** and **Ox-MWCNTs@Pd/TiO₂** nanohybrids.

### 1.2.1.4. Mott-Schottky analysis: introduction and theory

Electrochemical Impedance Spectroscopy is a powerful tool to study the properties of the electrode/electrolyte interface. With this technique the potential is sinusoidally varied at different frequencies around a mean value, and the measured current is evaluated from its in-phase or out-of-phase response with respect to the perturbation wave.

Such phase response is induced by the physical processes present in an electrochemical cell (accumulation of charge, charge transfer, diffusion, resistances, etc.). These processes are embodied by different electrical elements (resistors, capacitors, inductor, etc.), whose parallel and series combination completely define an electrochemical system.

For the purpose of this work EIS has been used to study the variation of the electrode capacity (a differential capacity, $dQ/dV$) as a function of the applied potential (Mott-Schottky analysis).

M-S analysis is typical in the field of semiconductor electrochemistry and is here applied in the case of **MWCNTs@Pd/TiO₂** for the semiconducting nature of the titania shell. Indeed, TiO₂ is a wide band gap semiconductor and when electrons are transferred in or out of the surface, charged regions, region of "space charge" result. The build-up of a space charge region is peculiar of semiconductors and is at the basis for the possibility to evaluate the potential dependence of the electrode capacity.

The excess charge in the space charge region may result from both immobile ions or mobile carriers (electrons or holes) and readily occurs when a semiconductor is dipped into a solution. In the case of TiO₂, a $n$-type semiconductor, as a result of the electric field that build-up at the interface, the valence and conduction bands bend "upwards" as highlighted in Fig. **1.12**. The magnitude of the bending is $V_{SC}$ the potential of the space charge and depends on several factors. However, $V_{SC}$ can be

controlled by the application of an external voltage and in principle different forms of space charge layer can be produced. For example, it is possible to accumulate or deplete the surface from majority carriers, so that accumulation or depletion layers would result. This has a great impact on the rate of electrochemical processes, since if the bands are bent such as to move majority carriers to the surface high currents can flow. However, if the voltage is reversed and majority carriers are drawn away from the surface, the barrier height $V_{SC}$ is increased and negligible currents will flow.
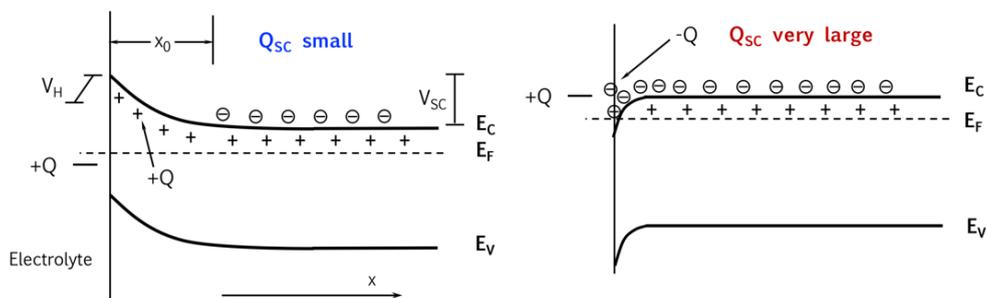


**Figure 1.12:** representation of possible space charge regions for an *n*-type semiconductor like $TiO_2$. **a)** Formation of a depletion layer in which majority carriers (electrons) are drawn away from the semiconductor/electrolyte interface (on the left). **b)** Accumulation layer formed when the semiconductor is forward biased ($E_{app}$ is made more negative and $V_{SC}$ is reduced).

If the Fermi energy of the semiconductor electrode is made enough negative (for *n*-type) or positive (for *p*-type), the depletion layer that usually forms after equilibration with the solution is progressively reduced until is reached a situation where the bands are completely flat ($V_{SC} = 0$ V). At that point substantial variations in the space charge capacity take place and they can be easily detected by EIS.[46]

In a depletion layer (Fig. **1.12b**) the capacity is very low because of the large distance between conducting ions and mobile carriers (electrons for $TiO_2$ that are away from the surface). By contrast, when an accumulation layer is formed the space charge capacity is much higher since the distance between ions in solution and mobile charges that accumulate at the surface is small (Fig. **1.12b**). The transition between these opposite scenarios can be observed experimentally recording EIS spectra at different applied potentials. The classical Mott-Schottky equation (Eq. **1.6**) describes quantitatively the relation between the space charge capacity ($C_{SC}$) and the applied potential (*E*). From the interpretation of the C/E data (also known as "Mott-Schottky plot") two important parameters can be derived:

the flatband potential, $E_{FB}$ (when $V_{SC}$ = 0 V), and the density of charge in the space charge region ($N_{SC}$). $E_{FB}$ is determined by extrapolation, while $N_{SC}$ is measured from the slope of the Mott-Schottky plot. In this specific case, where an *n*-type semiconductor is analyzed, $N_{SC}$ is referred to $N_D$, the donor density in the conduction band.

$$\frac{1}{C_{SC}^2} = \frac{2}{\varepsilon\varepsilon_0 N_D}\left(E - E_{fb} - \frac{k_B T}{e}\right)$$
Eq. **1.6**

(where $\varepsilon$ is the relative dielectric constant, $\varepsilon_0$ the permittivity of vacuum, *e* the electronic charge, $k_B$ the Boltzmann constant).

It is important to mention that the possibility to get very useful information from measurements of the differential capacitance derives from the peculiar properties of the semiconductor-electrolyte interface. In most semiconductors, any change in the electrode potential appears across the space-charge ($V_{SC}$) and not on the double-layer potential ($V_H$), see Appendix. Variations of $E_{app}$ during a Mott-Schottky analysis are therefore directly translated into different barrier heights $V_{SC}$.

The build-up of a space charge layer in semiconductors contributes to the overall capacitance with a term $C_{SC}$ that is additive to those of the electrical double-layer (the Helmholtz double-layer, $C_H$) and the Gouy-Chapman layer in solution ($C_G$, that has a negligible contribution). Their series combination is expressed by Eq. **1.7**:

$$\frac{1}{C_{TOT}} = \frac{1}{C_{SC}} + \frac{1}{C_H} + \frac{1}{C_G}$$
Eq. **1.7**

When $E_{app}$ is varied only $V_{SC}$ (and $C_{SC}$) changes ($C_G$ and $C_H$ remain unaffected), then M-S analysis is appropriate for a direct evaluation of the potential dependence of $C_{SC}$, that resemble the overall electrode capacity.

## 1.2.1.5. Mott-Schottky analysis: results

In Fig. **1.13**, the $C_{sc}$ values obtained from stepped potentiostatic electrochemical impedance spectroscopy (SPEIS) are plotted according to the Mott-Schottky equation (Eq. **1.6**)[47] for both **Ox-** and **Tour-MWCNTs@Pd/TiO₂**. For comparison, also the behavior of **Pd/TiO₂** and a GC electrode are shown. In these measurements the systems have been perturbed at the frequency of 1 kHz, previously determined from classical EIS at OCP to be an optimal value at which the contribution of the capacitive elements was higher.
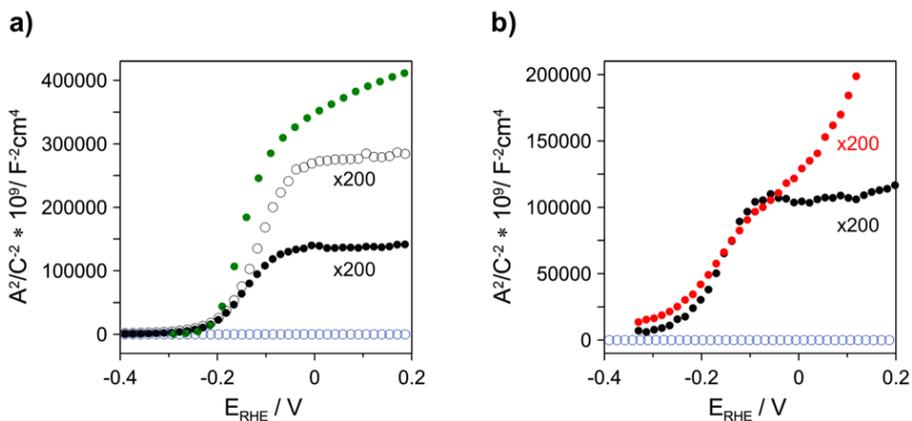
**Figure 1.13**: **a)** Mott-Schottky plots ($C_{SC}^{-2}$ vs. E) for **Pd/TiO₂** (green dots), the "standard" **Ox-MWCNT(20%wt.)@Pd/TiO₂** (black dots), **Ox-MWCNT(15%wt.)@Pd/TiO₂** (the sample with a lower amount of MWCNTs, empty black dots) and the inert GC substrate (blue empty dots). The plots have been obtained in Ar-saturated PB, pH= 7.4, at a fixed frequency of 1 kHz. Note the magnification for the **Ox-MWCNTs@Pd/TiO₂** samples. **b)** Comparison of **Ox-MWCNT@Pd/TiO₂** (black dots) and **Tour-MWCNT@Pd/TiO₂** (red dots). The GC substrate (blue dots) is also reported.

SPEIS investigations of the nanohybrids evidences remarkable changes in the electronic structure of TiO₂ caused by its integration with MWCNTs. Changes that will in turn favorably contribute to the general better electrocatalytic properties of these two nanostructures with respect to the **Pd/TiO₂** core-shell system. An increase of *(i)* the number of free electrons in the titania conduction band and *(ii)* surface defect density are in fact highlighted by the analysis of the interfacial capacity of **MWCNTs@Pd/TiO₂** compared to pristine **Pd/TiO₂** (Fig. **1.13a**). From analysis of the narrow E-dependent linear region (E ~0 V), a flat-band potential $E_{fb}$ = ~ -0.2 $V_{RHE}$ is obtained for all systems, in good agreement with reported values for TiO₂ at neutral pH.[48] By contrast, on passing from **Pd/TiO₂** to **MWCNTs@Pd/TiO₂**, the apparent donor density $N_D$, and hence the amount of free electrons in the TiO₂ conduction band, is increased by ~600 times. In this potential region both **Ox-** and **Tour- MWCNTs@Pd/TiO₂** behave similarly, displaying the same $E_{FB}$ and very comparable $N_D$ (Fig. **1.13b**). A similar behavior ascribed to the presence of MWCNTs has been observed in a ZnO-MWCNTs nanocomposite,[49] where the integration of oxide nanowires with MWCNTs resulted in a two-order of magnitude increase of $N_D$.

In light of the strong contribution coming from the MWCNTs on $N_D$, it has also been studied the effect of different MWCNTs loadings. For this purpose samples of **Ox-**

**MWCNTs(15%wt.)@Pd/TiO₂** have been prepared according to the above synthetic procedure, and compared with "standard" **Ox-MWCNT(20%wt.)@Pd/TiO₂** (Fig. **1.13a**). It has been found that $N_D$ further depends also on the Ox-MWCNTs concentration and increases by increasing the content of MWCNTs in the structure (Table **1.3**). Again $E_{FB}$ is unaffected, but $N_D$ for (MWCNT15%) are reduced by half the value of (MWCNT20%). The larger availability of free electrons at the **TiO₂/Pd** interface induced by the integration with MWCNTs is expected to play a favorable effect on the HER kinetics, especially at low overpotentials.

Finally, analysis of the M-S plots at higher potentials, where the capacity attains a constant value, evidences the presence of extended surface states, whose density is proportional to $C_{SC}$[46] and largely increases on passing from **Pd/TiO₂** to **Ox-MWCNT@Pd/TiO₂** (Fig. **1.13a**). Such defects on the surface of the titania shells (oxygen vacancies and incompletely coordinated Ti atoms)[37] that would be mostly localized at the interface with MWCNTs, may provide efficient catalytic sites for the adsorption and catalytic dissociation of water molecules, a fundamental step for the promotion of HER in neutral and alkaline media. As a matter of fact, as the kinetic studies of the electrocatalytic behavior show (Tafel slope analysis, see later), water dissociation and adsorbed hydrogen formation would represent the rate determining step of HER in the present conditions. It is interesting to note that in the case of **Tour-MWCNT@Pd/TiO₂** $C_{SC}$ does not attain a constant value (red dots Fig. **1.13b**) thus excluding the the presence of extended surface states. Recalling the lower performances of this nanocomposite (Fig. **1.6a** and **1.11a**) it may be inferred that surface states play a major role in promoting the electrocatalytic activity. In spite of the fact that Tour functionalization brings a more uniform and homogenous coverage of the MWCNTs, the generation of a lower amount of surface states at the interface MWCNTs-TiO₂ would be detrimental towards the catalytic activity.

| Catalyst | $\eta$@-1.25 mAcm$^{-2}$ (V) [a] | $Q_{Pd}$ [b] ($\mu$C) | $TOF_0$ [c] (h$^{-1}$) | $E_{FB}$ (V$_{RHE}$) | $C_{ss}/A$ [d] (Fcm$^{-2}$) | $N_D$x10$^{15}$ (cm$^{-3}$) [e] |
|---|---|---|---|---|---|---|
| Pd/TiO₂ | -0.39 | 22 | 47 | -0.22 | 200 | 1.1 |
| Ox-MWCNT@Pd/TiO₂ | -0.33 | 28 | 242 | -0.23 | 8200 | 640 |
| Ox-MWCNT(15%)@Pd/TiO₂ | -0.35 | 25 | 86 | -0.23 | 1200 | 330 |
| Tour-MWCNT@Pd/TiO₂ | -0.37 | 28 | 133 | -0.27 | - | 670 |

**Table 1.3**: Characteristic properties of the various electrocatalysts obtained from LSV, TOF and SPEIS analysis. **a)** overpotential for HER in Ar-saturated PB (pH = 7.4), measured at a current threshold of -

1.25 mAcm$^{-2}$; **b)** Charge related to electroactive Pd as determined by CV in NaOH solutions. **c)** TOF determined by extrapolation at η = 0 V. **d)** Surface states capacitance and **e)** donor densities obtained from the Mott-Schottky plots.

## 1.2.2 Effects of a thermal treatment on the electrochemical properties of MWCNT@Pd/TiO$_2$.

As outlined at the beginning of this Chapter, the effects of a thermic treatment on both **Ox-MWCNT@Pd/TiO$_2$** and **Tour-MWCNT@Pd/TiO$_2$** have been addressed. Once the powders have been synthetized, they underwent calcination in air at ambient pressure. The samples were heated at a rate of 3°C/min from RT to 250°C, where they are kept for 5 hours, and then allowed to cool down at the rate of 4.5°C/min. The electrochemical characterization revealed the huge effects that such calcination procedure had on the electrocatalytic performance of the various nanocomposites. In view of a rigorous comparison, the samples were tested under the same conditions and following the same protocols used above on the pre-calcination samples.

LSVs of calcinated and untreated electrocatalysts are compared in Fig. **1.14a**. As clearly seen, calcination strongly improves the electrocatalytic properties of the films towards HER, evidenced by the positive shift of the overpotential to an outstanding value of -0.20 V at 1.25 mAcm$^{-2}$ for both **Ox-MWCNT@Pd/TiO$_2$** and **Tour-MWCNT@Pd/TiO$_2$** (*vis-à-vis* -0.39 V in the case of core-shell **Pd/TiO$_2$**). It is worth mentioning that under the above conditions, protons are reduced on massive platinum electrodes at about -0.10 V and that, at this pH, about 50% of the total overpotential is due to concentration overpotential.[12] Notice that the above η$_{conc}$ contribution was determined under controlled convective mass transport regime (RDE), while the present results were obtained under less favorable conditions, i.e. stationary electrodes in unstirred solutions. As the almost identical electrochemical response of **Ox-MWCNTs@Pd/TiO$_2$** and **Tour-MWCNTs@Pd/TiO$_2$** suggest, it is likely that after calcination the two originally different materials merge into a similar structure, likely via an effective removal of the organic functionalities, which consequently increases the interactions between MWCNTs and TiO$_2$.

Also in the case of the calcinated materials it is very evident how much the presence of MWCNTs fosters electrocatalytic HER. In Fig. **1.14b** is shown a comparison between the nanocomposites **CALC-Ox-MWCNTs@Pd/TiO$_2$** and **CALC-Pd/TiO$_2$**.

The current transients, measured during CA experiments in which the cathode potential is stepped back and forth between 0 V and various negative values, are highly stable and reproducible. The stable CA signal lasting more than 45 hours (Fig. **1.14c**), demonstrates the substantial chemical and mechanical integrity of the catalyst films under HER conditions, with a less than 15% decrease of cathodic HER current. Notice that the calcinated samples display cathodic currents also at potential positive of 0 $V_{RHE}$ (see Fig. **1.14d**). These weak currents obviously are not HER-related, and may be otherwise associated to the absorption of H ($H_{abs}$) into the Pd lattice.[50-52] This contribution however was taken into account  (and excluded) in the determination of the exchange current density ($J_0$, see later). This enhanced hydrogen absorption is correlated to the higher $Q_{Pd}$ values found in these case (Table **1.4**), meaning that calcination increases protons accessibility to the Pd NPs in both **CALC-Ox-MWCNT@Pd/TiO₂** and **CALC-Tour-MWCNT@Pd/TiO₂**.
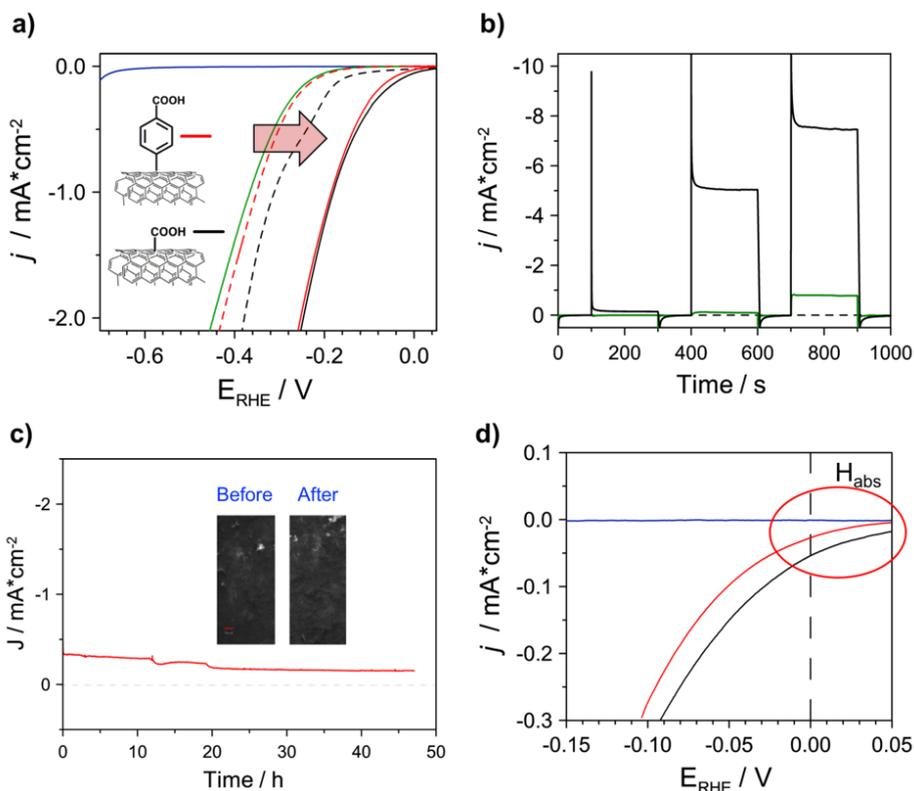


**Figure 1.14**: Electrochemical characterization of the calcinated samples in Ar-saturated PB solution, pH=7.4. **a)** LSV for all the various nanostructured catalyst, with highlighted the great improvement obtained after calcination. The i/V curves of **CALC-Ox-MWCNTs@Pd/TiO₂** (black solid line) and **CALC-**

**Tour- MWCNTs@Pd/TiO₂** (red solid line) result positively shifted by 200mV. **b)** CA of **CALC-Pd/TiO₂** (green line) and **CALC-Ox- MWCNTs@Pd/TiO₂** (black line) at potentials of -0.06, -0.38 and -0.55V vs. RHE. **c)** CA at $E_{RHE}$ = -0.15V for over 45 h after the deposition of **CALC-Tour-MWCNT@Pd/TiO₂**. The inset shows optical images of the SPE electrode surface before and after extended electrolysis. **d)** enlargement of panel a) in the region of low overpotentials with highlighted the current of hydrogen absorption for **CALC-Ox** and **CALC-Tour-MWCNT@Pd/TiO₂**.

A more quantitative evaluation of the catalytic behavior was then carried out by determining the TOF following the approach described earlier (Fig. **1.11a**). Such an approach minimizes in fact possible overestimation of the catalytic properties arising from the possible increase of catalytic sites and/or by a better accessibility to the Pd NPs after calcination. As evidenced in Fig. **1.15a**, the TONs and $TOF_0$ of **CALC-Ox-MWCNTs@Pd/TiO₂** by far exceed those of the untreated samples, reaching TOF values in the order of 150.000 $h^{-1}$ at $\eta$ as low as 50 mV. The negligible differences between **CALC-Ox-MWCNTs@Pd/TiO₂** and **CALC-Tour-MWCNTs@Pd/TiO₂** already seen by LSV are also revealed by TOF analysis (not shown). As hypothesized above, the thermal treatment induced changes in the nanostructures morphology that brings about a generalized improved accessibility of the catalytic Pd sites. Indeed, the respective integrated $Q_{Pd}$ charges (i.e., the electroactive Pd) increase, however the HER rate, as determined by TOF that is normalized by accessible Pd sites, is considerably higher. These findings reveal the key role played by the MWCNTs-TiO₂ interface in driving the HER, its contribution being even more important than the mere amount of active catalyst within the nanostructure.
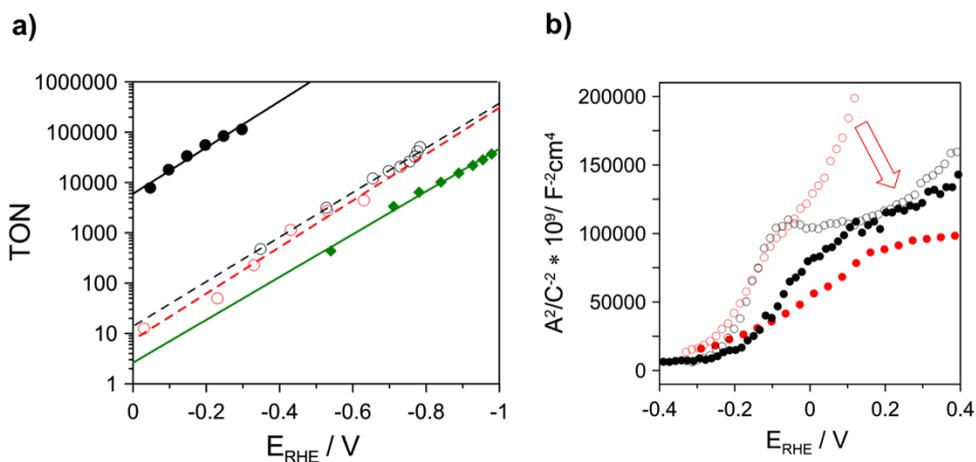


**Figure 1.15**: **a)** TON as a function of overpotential for **CALC-Ox-MWCNT@Pd/TiO₂** (black filled dots) and the untreated samples (see legend of Fig. **1.11a**). TOF values are obtained from TON/time. **b)**

Mott-Schottky plots ($C_{SC}^{-2}$ vs. $E_{app}$) for **CALC-Ox-MWCNT@Pd/TiO₂** (black filled dots), **Ox-MWCNT@Pd/TiO₂** (black empty dots), **CALC-Tour-MWCNT@Pd/TiO₂** (red filled dots) and **Tour-MWCNT@Pd/TiO₂** (red empty dots). The plots have been obtained in Ar-saturated PB, pH = 7.4, at a fixed frequency of 1 kHz (previously chosen by EIS at OCP).

To further investigate the role of MWCNTs and to look for possible effects on the electronic properties of $TiO_2$, M-S analysis was performed also in the case of the calcinated samples (Figure **1.15b**).

A common feature in the Mott-Schottky analysis of the calcinated samples is the expected invariance of the flatband potentials (Table **1.4**). By contrast, the observed decrease of the slope of the linear region would suggest a sizeable increase of donor density, in turn resulting in an increased electron availability at the interface (and thus faster charge transfer kinetics). Furthermore, at higher potentials the Mott-Schottky plot for **CALC-Tour-MWCNT@Pd/TiO₂** did show a remarkable region of constant capacitance that was not observed in the untreated **Tour-MWCNT@Pd/TiO₂** samples, and is attributed to the presence of extended surface states. After calcination, both **CALC-Tour-MWCNT@Pd/TiO₂** and **CALC-Ox-MWCNT@Pd/TiO₂** do show then very similar electrochemical properties and electrocatalytic performance thus highlighting the decisive role played by the MWCNTs-$TiO_2$ interface in governing the catalytic activity.

| Catalyst | η@-1.25 mAcm$^{-2}$(V) [a] | $Q_{Pd}$ [b] (μC) | $TOF_0$ [c] (h$^{-1}$) | $E_{FB}$ ($V_{RHE}$) | $C_{ss}$/A [d] (Fcm$^{-2}$) | $N_D$ x10$^{15}$ [e] (cm$^{-3}$) |
|---|---|---|---|---|---|---|
| Pd/TiO₂ | -0.39 | 22 | 47 | -0.22 | 200 | 1.1 |
| Ox-MWCNT@Pd/TiO₂ | -0.33 | 28 | 242 | -0.23 | 8200 | 640 |
| Tour-MWCNT@Pd/TiO₂ | -0.37 | 28 | 133 | -0.27 | - | 670 |
| **CALCINATION** | | | | | | |
| Ox-MWCNT@Pd/TiO₂ | -0.20 | 51 | 60000 | -0.21 | 8000 | 990 |
| Tour-MWCNT@Pd/TiO₂ | -0.20 | 77 | 58000 | -0.28 | 8600 | 1600 |

**Table 1.4**: Characteristic properties of the various electrocatalyst. **a)** overpotential for HER in PB (pH = 7.4), measured at a current threshold of -1.25 mAcm$^{-2}$; **b)** Charge related to electroactive Pd as determined by CV in NaOH solutions. **c)** TOF determined by extrapolation at η = 0 V. **d)** Surface states capacitance and **e)** donor densities obtained from the Mott-Schottky plots.

## 1.3. HER mechanism: Tafel analysis

The mechanism of HER classically comprises three possible step-reactions (Eq. **1.1a-c**). Coupling of reaction (**1.1a**) with either (**1.1b**) or (**1.1c**) results in the so-called Volmer-Heyrovsky or Volmer-Tafel routes. Elucidation of the prevailing mechanism is usually based on the inspection of the slopes in a $\eta$/Log(i) plot, known as "Tafel plots", that display characteristic values depending on the rate-determining step (*rds*). Useful information can also be obtained from log(i)/pH plots where changes in the reaction mechanism can be devised by different pH-dependency (see Fig. **1.1**). Unfortunately, if the Volmer step is the *rds*, it is impossible to determine the complete mechanism, but simply recognize that $H_{ads}$ formation is limiting HER. This is exactly the case for water reduction at neutral pH, where a key step of HER is $H_{ads}$ formation via water dissociation ($H_2O + e^- \rightarrow H_{ads} + OH^-$) that gives a theoretical Tafel slope of 118 mV/dec.[53]

In Fig. **1.16** the Tafel plots are reported for all the nanostructured systems studied in this work, calcinated and untreated **Ox-MWCNT@Pd/TiO₂** (black squares) and **Tour-MWCNT@Pd/TiO₂** (red squares), as well as the model system **Pd/TiO₂** (green dots). The corresponding exchange current densities ($J_0$ at $\eta$ = 0 V) and the Tafel slopes (derived by fitting) for the various systems are summarized in Table **1.5**.
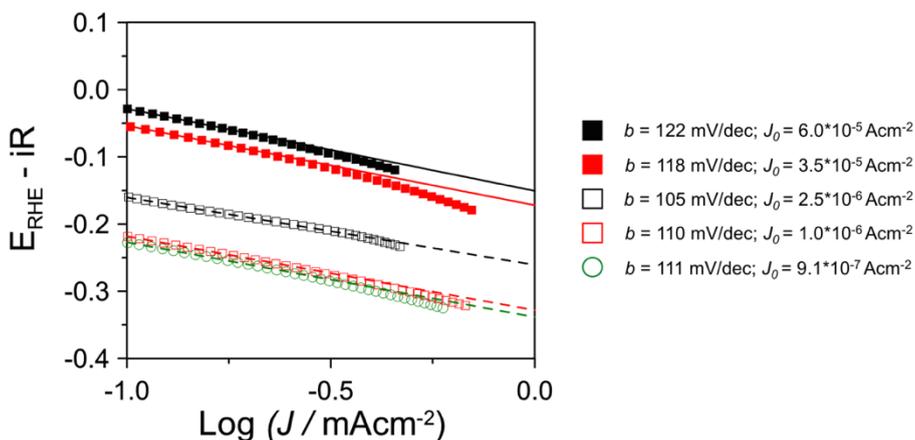


**Figure 1.16**: Tafel plots for **CALC-Ox-MWCNT@Pd/TiO₂** (black squares), **CALC-Tour-MWCNT@Pd/TiO₂** (red squares), **Ox-MWCNT@Pd/TiO₂** (black empty squares), **Tour-MWCNT@Pd/TiO₂** (red empty squares) and **Pd/TiO₂** (green empty dots). Analysis of the Tafel slopes is focused in the narrow potential region at which the various materials begin to display HER cathodic currents.

61

The observed Tafel slopes in the range 110-120 mV/dec are in good agreement with literature values for HER on Pd electrodes,[54] and, combined with the unitary slope found in the log(i)/log[H⁺] plot, emphasize the role of the Volmer step as the *rds*.[14] The latter plot has been obtained by titration of a water-free acetonitrile solution with a proton donor (Fig. **1.17**). As the proton source was used the triflate salt of protonated dimethylformamide 1:1 mol/mol [DMFH]OTf/DMF, prepared accordingly to a reported procedure.[55] As the CVs of Fig. **1.17** show, the reduction of protons occurs at $E_{1/2}$ = -0.29 V vs. Ag/AgCl, with a shape that is typical of a diffusion-controlled process. The inset of the same figure highlights the linear relation between the intensity of the current and H⁺ concentration.
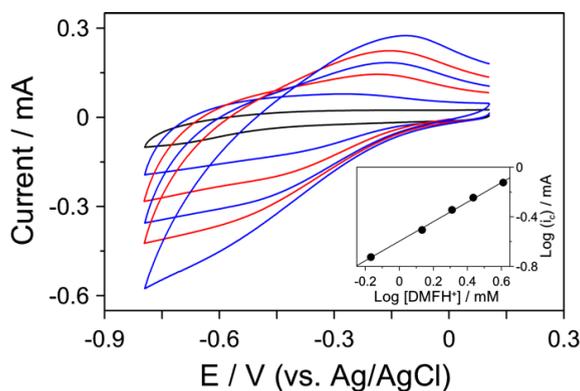


**Figure 1.17**: CVs for **MWCNT@Pd/TiO2** drop-casted onto an ITO electrode in pure CH₃CN (black line) and after increasing additions of a specific proton source, namely 1:1 mol/mol [DMFH]OTf/DMF (resulting [DMFH]⁺ = 0.68, 1.36, 2.04, 2.72, 4.08 mM) in CH₃CN/ 0.08 M TBAPF₆ Ar-saturated solution. Inset: linear relationship between the peak cathodic current and [DMFH⁺] concentration. Scan rate = 0.05 Vs⁻¹. The diameter of the electroactive surface (ITO) is 8 mm.

Given the identical Tafel slopes for all composites, it is likely that the Pd catalytic active cores operate within the different nanostructures according to the same mechanism. The arrangement of different morphologies at the nanometric scale do not seem to affect significantly the mechanism, which is always dominated by $H_{ads}$ formation.    Indeed, dissociation of water and formation of reacting intermediates limit the kinetics for all the studied electrocatalysts at the neutral pH values of the present study. The Tafel slopes reported in literature for Pd-based systems are usually obtained at basic pH (mostly KOH 0.1-1 M), however the same slopes found in alkaline solutions and in this work would confirm the similarity of the catalytic mechanisms in the two environments. Unfortunately, the lack of experimental reports in neutral solutions makes the evaluation of the performance

of the present Pd-based electrocatalysts very difficult.[56] However, the availability of free protons in neutral and alkaline media is critical and in such a scenario the synergic combination of the three building blocks in **CALC-Ox-MWCNT@Pd/TiO$_2$** and **CALC-Tour-MWCNT@Pd/TiO$_2$** seems to be essential to drive HER at a good rate.

For what concerns the exchange current densities, the observed $J_0$ reflect qualitatively the same trend found for the TOF$_0$, with a two order of magnitude increase on going from **Pd/TiO$_2$** to **CALC-Ox-MWCNT@Pd/TiO$_2$**. The lack of studies at neutral pH makes difficult to evaluate the catalysts performance also on the basis of $J_0$ values. However, a tentative discussion can be done setting side by side the activity of the studied nanostructures with those of Pd-based catalysts, both in acid and in basic solution. It is well known that HER activity in acid for any electrocatalyst is orders of magnitude higher than in base. The reasons for that are still under debate, but experimental data agree to this point.[57] Pd electrodes in HCl have $J_0$ in the order of $2*10^{-4}$ Acm$^{-2}$, while in NaOH $J_0$ is reduced to $3*10^{-6}$ Acm$^{-2}$.[58] Pd NPs supported on Carbon has been found to have $J_0$ in the order of $10^{-3}$ Acm$^{-2}$ in HClO$_4$ 0.1 M and $J_0$ of $6*10^{-5}$ Acm$^{-2}$ in KOH 0.1 M.[14] Since at neutral pH (from 5 to 9) HER is usually more sluggish than at any other pH value,[12] $J_0$ values in the order of 4-$7*10^{-6}$ found for the optimized samples are reasonably in line to the situation of an inhibited HER. As mentioned in the previous section the contribution of H absorption for the calcinated samples is excluded from $J_0$ determination and the observed trend is not biased by that process.

| Catalyst | η@-1.25 mAcm$^{-2}$ (V) | Tafel slope (mV/dec) | $J_0$ (Acm$^{-2}$) |
|---|---|---|---|
| Pd/TiO$_2$ | -0.39 | 111 | $9.1*10^{-7}$ |
| Ox-MWCNT@Pd/TiO$_2$ | -0.33 | 105 | $2.5*10^{-6}$ |
| Tour-MWCNT@Pd/TiO$_2$ | -0.37 | 110 | $1.0*10^{-6}$ |
| **CALCINATION** | | | |
| CALC-Ox-MWCNT@Pd/TiO$_2$ | -0.2 | 122 | $6.0*10^{-5}$ |
| CALC-Tour-MWCNT@Pd/TiO$_2$ | -0.2 | 118 | $3.5*10^{-5}$ |

**Table 1.5:** Typical figures of merits of electrocatalysis for the nanostructured systems studied in this work. Tafel slope values have been derived by fitting of the respective Tafel plots in the low overpotential regime (0 < η < 0.2), while ($J_0$) are obtained by extrapolation at E = 0 V$_{RHE}$.

## 1.4. Conclusion & Outlooks

In the challenging context of HER electrocatalysis at neutral pH, the general good electrochemical activity of the class of nanocomposites studied, **MWCNT@Pd/TiO₂**, is associated to the strong cooperation of the various constituents, MWCNTs, Pd NPs and TiO₂. One of the key advantage of nanotechnology is the possibility to create structures in which the ensemble possesses properties that go beyond those of each singular unit. This peculiarity is evident in the class of nanocomposites here studied, where the various building blocks clearly interact sinergically and the advantages of nanostructuring the electrocatalysts is capitalized.

MWCNTs not only provide an optimal electrical conductivity and high specific surface area, but it is here proved that they modify the electronic properties of the TiO₂ shell in which they are wrapped. Specifically, by comparison with the model core-shell system Pd/TiO₂, a higher donor density is found in the presence of MWCNTs, and their absolute value correlate with MWCNTs concentration in the nanocomposites.

For what concerns TiO₂, the metal oxide shell is designed to promote the adsorption of water molecules and their dissociative adsorption at the boundaries with the Pd clusters, where HER occur. At basic/neutral pH the low availability of protons is a main drawback for HER and intermediates adsorption ($H_{ads}$) following water dissociation is thought to control the rate of the overall process. The results here obtained (Tafel plot) confirm the importance of water dissociation and $H_{ads}$ formation. The synergic effects of TiO₂ and Pd NPs translate in the very high electrocatalytic activity of **MWCNT@Pd/TiO₂**.

From our studies it was also evidenced that the benefits deriving from cooperation between metal nanoparticles and metal oxides are further increased for the strong contribution coming from carbon nanotubes. Combination of EIS (Mott-Schottky analysis) and classical electrochemical characterization, revealed that MWCNTs induce surface states defects in TiO₂ thus contributing to HER activity. The best performing materials, **CALC-Ox-MWCNT@Pd/TiO₂** and **CALC-Tour-MWCNT@Pd/TiO₂**, are obtained when the samples undergo a thermal treatment (calcination). After calcination the highest $TOF_0$ and $J_0$ values were achieved, revealing the importance of the interface MWCNTs-TiO₂ that is the main feature that govern the electrochemical activity of the nanostructures.

To this end it will be very interesting to study if the combination of other carbon nanostructures has the same beneficial effect on HER activity, possibly utilizing also other combinations of oxides or metal nanoparticles.

## 1.5. Bibliography

1   P. V. Kamat, Meeting the clean energy demand: nanostructure architectures for solar energy conversion, *J. Phys. Chem. C*, **111**, 2834–2860 (2007).
2   T. Bak, J. Nowotny, M. Rekas, C. C. Sorrell, Photo-electrochemical hydrogen generation from water using solar energy. Materials- related aspects. *Int. J. Hydrogen Energy* **27**, 991–1022 (2002).
3   J. O. M. Bockris, A hydrogen economy, *Science*, **176**, 1323 (1972).
4   N. M. Markovic, B. N. Grgur, P. N. Ross, Temperature-dependent hydrogen electrochemistry on platinum low-index single-crystal surfaces in acid solutions. *J. Phys. Chem. B,* **101**, 5405-5413 (1997).
5   N. M. Markovic, S. T. Sarraf, H. A. Gasteiger, P. N. Ross, Hydrogen electrochemistry on platinum low-index single-crystal surfaces in alkaline solution. *J. Chem. Soc. Faraday Trans.,* **92**, 3719-3725 (1996).
6   K. Zeng, D. Zhang, Recent progress in alkaline water electrolysis for hydrogen production and applications, *Prog. Energy Combust. Sci.*, **36**, 307–326 (2010).
7   A. Wieckowski, J. K. Nørskov, *Fuel Cell Science: Theory, Fundamentals and Biocatalysis* (John Wiley & Sons, Inc., Hoboken, 2010).
8   T. Hisatomi, J. Kubota, K. Domen, Recent advances in semiconductors for photocatalytic and photoelectrochemical water splitting, *Chem. Soc. Rev.*, **43**, 7520-7535 (2014).
9   B. E. Logan, B. Hamelers, R. Rozendal, U, Schroder, J. Keller, S. Freguia, P. Aelterman, W. Verstraete, K. Rabaey, *Environ. Sci. Technol.*, **40**, 5181–5192 (2006).
10  M. Auinger, I. Katsounaros, J. C. Meier, S. O. Klemm, P. U. Biedermann, A. A. Topalov, M. Rohwerdera, K. J. J. Mayrhofer, Near-surface ion distribution and buffer effects during electrochemical reactions, *Phys. Chem. Chem. Phys.*, **13**, 16384–16394 (2011).
11  I. Katsounaros, J. C. Meier, S. O. Klemm, A. A. Topalov, P. U. Biedermann, M. Auinger, K. J. J. Mayrhofer, The effective surface pH during reactions at the solid–liquid interface*, Electrochem. Commun.*, **13**, 634–637 (2011).
12  T. Shinagawa, K. Takanabe, Electrocatalytic Hydrogen Evolution under Densely Buffered Neutral pH Conditions, *J. Phys. Chem. C*, **119**, 20453–20458 (2015).

13  T. Shinagawa, A. T. Garcia-Esparza, K. Takanabe, Mechanistic Switching by Hydronium Ion Activity for Hydrogen Evolution and Oxidation over Polycrystalline Platinum Disk and Platinum/Carbon Electrodes, *ChemElectroChem,* **1**, 1497 – 1507 (2014).

14  J. Durst, A. Siebel, C. Simon, F. Hasché, J. Herranz, H. A. Gasteiger, New insights into the electrochemical hydrogen oxidation and evolution reaction mechanism. *Energy Environ. Sci.,* **7**, 2255-2260 (2014).

15  T. Shinagawa, A. T. Garcia-Esparza, K. Takanabe, Insight on Tafel slopes from a microkinetic analysis of aqueous electrocatalysis for energy conversion, *Sci. Rep.,* **5**:13801 (2015).

16  R. Subbaraman, D. Tripkovic, D. Strmcnik, K-C. Chang, M. Uchimura, A. P. Paulikas, V. Stamenkovic, N. M. Markovic, Enhancing hydrogen evolution activity in water splitting by tailoring $Li^+$-$Ni(OH)_2$-Pt interfaces, *Science,* **334**, 1256-1260 (2011).

17  D.Strmcnik, M. Uchimura, C. Wang, R. Subbaraman, N. Danilovic, D. van der Vliet, A. P. Paulikas, V. R. Stamenkovic, N. M. Markovic, Improving the hydrogen oxidation reaction rate by promotion of hydroxyl adsorption, *Nat. Chem.,* **5**, 300-306 (2013).

18  M. Cargnello, M. Grzelczak, B. Rodrı́guez-Gonzaĺez, Z. Syrgiannis, K. Bakhmutsky, V. LaParola, L. M. Liz-Marzań, R. J. Gorte, M. Prato, P. Fornasiero, Multiwalled Carbon Nanotubes Drive the Activity of Metal@oxide Core–Shell Catalysts in Modular Nanocomposites, *J. Am. Chem. Soc.*, **134**, 11760-11766 (2012).

19  J. L. Bahr, J. M. Tour, Highly Functionalized Carbon Nanotubes Using in Situ Generated Diazonium Compounds, *Chem. Mater.*, **13**, 3823–3824 (2001).

20  D. S. Su, G. Centi, S. Perathoner, Nanocarbons for the Development of Advanced Catalysts, *Chem. Rev.,* **113**, 5782-5816 (2013).

21  F. M. Toma, A. Sartorel, M. Iurlo, M. Carraro, P. Parisse,  C. Maccato, S. Rapino, B. Rodriguez Gonzalez, H. Amenitsch, T. Da Ros, L. Casalis, A. Goldoni, M. Marcaccio, G. Scorrano, G. Scoles, F. Paolucci, M. Prato, M. Bonchio, Efficient water oxidation at carbon nanotube–polyoxometalate electrocatalytic interfaces, *Nat. Chem.*, **2**, 826-831 (2010).

22  F. M. Toma, A. Sartorel, M. Iurlo, M. Carraro, S. Rapino, L. Hoober-Burkhardt, T. Da Ros, M. Marcaccio, G. Scorrano, F. Paolucci, M. Bonchio, M. Prato, Tailored functionalization of carbon nanotubes for electrocatalytic water splitting and sustainable energy applications, *ChemSusChem*, **4**, 1447-1451 (2011).

23  E. S. Andreiadis, P. A. Jacques, P. D. Tran, A. Leyris, M. Chavarot-Kerlidou, B. Jousselme, M. Matheron, J. Pécaut, S. Palacin, M. Fontecave, V. Artero, Molecular engineering of a cobalt-based electrocatalytic nanomaterial for $H_2$ evolution under fully aqueous conditions, *Nat. Chem.*, **5**, 48-53 (2013).

24   M. Gong, W. Zhou, M-C. Tsai, J. Zhou, M. Guan, M-C. Lin, B. Zhang, Y. Hu, D-Y. Wang, J. Yang, S. J. Pennycook, B-J. Hwang, H. Dai, Nanoscale nickel oxide/nickel heterostructures for active hydrogen evolution electrocatalysis, *Nat. Comm.*, **5**, 4695 (2014).

25   M. Gong, Y. Li, H. Wang, Y. Liang, J. Z. Wu, J. Zhou, J. Wang, T. Regier, F. Wei, H. Dai. An Advanced Ni–Fe Layered Double Hydroxide Electrocatalyst for Water Oxidation, *J. Am. Chem. Soc.*, **135**, 8452–8455 (2013).

26   Y. Liang, H. Wang, P. Diao, W. Chang, G. Hong, Y. Li, M. Gong, L. Xie, J. Zhou, J. Wang, T. Z. Regier, F. Wei, H. Dai. Oxygen Reduction Electrocatalyst Based on Strongly Coupled Cobalt Oxide Nanocrystals and Carbon Nanotubes, *J. Am. Chem. Soc.*, **134**, 15489-15857 (2012).

27   P. Serp, J. L. Figueiredo, *Carbon materials for catalysis* (J. Wiley and sons, Hoboken, 2009)

28   S. Trasatti, Work function, electronegativity, and electrochemical behavior of metals. 3. Electrolytic hydrogen evolution in acid solutions, *J. Electroanal. Chem.*, **39**, 163–184 (1972).

29   J. Suntivich, K. J. May, H. A. Gasteiger, J. B. Goodenough, Y. Shao-horn, A Perovskite Oxide Optimized for Molecular Orbital Principles. *Science*, **334**, 2010–2012 (2011).

30   W. Sheng, M. Myint, J. G. Chen, Y. Yan, Correlating the hydrogen evolution reaction activity in alkaline electrolytes with the hydrogen binding energy on monometallic surfaces, *Energy Environ. Sci.,* **6**, 1509-1512 (2013).

31   N. N. Greenwald, A. Earnshaw, *Chemistry of the elements* (Pergamon press, 1985).

32   P. A. Thiel, T. E. Madey, The interaction of water with solid surfaces: fundamental aspects, *Surf. Sci. Rep.*, **7**, 211 (1987).

33   V. E. Henrich, P. A. Cox, *The Surface Science of Metal Oxides* (Cambridge Univ. Press, Cambridge, 1994).

34   M. A. Henderson, The interaction of water with solid surfaces: fundamental aspects revisited, *Surf. Sci. Rep.*, **46**, 1 (2002).

35   J. A. Rodriguez, S. Ma, P. Liu, J. Hrbek, J. Evans, M. Pérez, Activity of $CeO_x$ and $TiO_x$ Nanoparticles Grown on Au(111) in the Water-Gas Shift Reaction, *Science,* **318**, 1757 (2007).

36   Q. Fu, H. Saltsburg, M. Flytzani-Stephanopoulos, Alkali-Stabilized $Pt-OH_x$ Species Catalyze Low-Temperature Water-Gas Shift Reactions, *Science*, **301**, 935 (2003).

37   U. Diebold, The surface science of titanium dioxide, *Surf. Sci. Rep.*, **48**, 53-229 (2003).

38   Values obtained analyzing data reported in the Supporting Information of ref. [14]

39 G. Wittstock, M. Burchardt, S. E. Pust, Y. Shen, C. Zhao, Scanning Electrochemical Microscopy for Direct Imaging of Reaction Rates, *Angew. Chem. Int. Ed.*, **46**, 1584-1617 (2007).

40 M. C. Sanchez-Sanchez, J. Rodriguez-Lopez, A. J. Bard, Scanning Electrochemical Microscopy. 60. Quantitative Calibration of the SECM Substrate Generation/Tip Collection Mode and Its Use for the Study of the Oxygen Reduction Mechanism, *Anal. Chem.*, **80**, 3254-3260 (2008).

41 A. J. Bard, M. V. Mirkin, in *Scanning Electrochemical Microscopy* (Marcel Dekker Inc., New York, 2001).

42 S. Amemiya, A. J. Bard, F. F. Fan, M. V. Mirkin, P. R. Unwin, Scanning Electrochemical Microscopy, *Annu. Rev. Anal. Chem.*, **1**, 95-131 (2008).

43 M. Hara, U. Linke, T. Wandlowski, Preparation and electrochemical characterization of palladium single crystal electrodes in 0.1 M $H_2SO_4$ and $HClO_4$: Part I. Low-index phases, *Electrochim. Acta*, **52**, 5733-5748 (2007).

44 C. Costentin, S. Drouet, M. Robert, J-M. Savéant, Turnover numbers, turnover frequencies, and overpotential in molecular catalysis of electrochemical reactions. cyclic voltammetry and preparative-scale electrolysis. *J. Am. Chem. Soc.*, **134**, 11235–11242 (2012).

45 W. Sheng, H. A. Gesteiger, Y. Shao-Horn, Hydrogen Oxidation and Evolution Reaction Kinetics on Platinum: Acid vs Alkaline Electrolytes, *J. Electrochem. Soc.,* **157**, B1529-B1536 (2010).

46 N. Sato, *Electrochemistry at metal and semiconductor electrodes* (Elsevier Science B. V., Amsterdam, 1998).

47 A. J. Bard, L. R. Faulkner, *Electrochemical Methods: Fundamentals and Applications*, (Wiley, New York, ed. 2 ,2001).

48 L. Kavan, M. Grätzel, S. E. Gilbert, C. Klemenz, H. J. Scheel, Electrochemical and photoelectrochemical investigation of single-crystal anatase, *J. Am. Chem. Soc.*, **116**, 6716-6723 (1996).

49 W-D. Zhang, L-C. Jiang, J-S. Ye, Photoelectrochemical study on charge transfer properties of ZnO nanowires promoted by carbon nanotubes, *J. Phys. Chem. C.,* **113**, 16247–16253 (2009).

50 S. Štrbac, M. Smiljanić, Z. Rakočević, Electrocatalysis of hydrogen evolution on polycrystalline palladium by rhodium nanoislands in alkaline solution, *J. Electroanal. Chem.,* **755**, 115-121 (2015).

51 M. Smiljanić, I. Srejić, B. Grgur, Z. Rakočević, S. Štrbac, Catalysis of hydrogen evolution on different Pd/Au(111) nanostructures in alkaline solution, *Electrochim. Acta*, **88**, 589–596 (2013).

52 A. Lasia, On the mechanism of the hydrogen absorption reaction, *J. Electroanal. Chem.*, **593**, 159–166 (2006).

53    K. Krischer, E. R. Savinova, *Fundamentals of electrocatalysis*, in *Handbook of Heterogeneous Catalysis*, *2nd Ed*., Eds. G. Ertl, H. Knozinger, F. Schuth, J. Weitkamp (Wiley-VCH Verlag, Weinheim, 2008).

54    B. Conway, B. V. Tilak, Interfacial processes involving electrocatalytic evolution and oxidation of $H_2$, and the role of chemisorbed H, *Electrochimica Acta*, **47**, 3571-3594 (2002).

55    A. Le Goff, V. Artero, B. Jousselme, P. D. Tran, N. Guillet, R. Métayé, A. Fihri, S. Palacin, M. Fontecave, From Hydrogenases to Noble Metal–Free Catalytic Nanomaterials for $H_2$ Production and Uptake, *Science,* **326**, 1384-1387 (2009).

56    Y-X. Huang, X-W. Liu, X-F. Sun, G-P. Sheng, Y-Y. Zhang, G-M. Yan, S-G. Wang, A-W. Xu, H-Q. Yu, A new cathodic electrode deposit with palladium nanoparticles for cost-effective hydrogen production in a microbial electrolysis cell, *Int. J. Hydrogen Energ.*, **36**, 2773-2776 (2011).

57    W. Sheng, Z. Zhuang, M. Gao, J. Zheng, J. G. Chen, Y. Yan, Correlating hydrogen oxidation and evolution activity on platinum at different pH with measured hydrogen binding energy, *Nat. Commun.*, **6**:5848 (2015).

58    N. Pentland, J. O. M. Bockris, E. Sheldon, Hydrogen evolution reaction on copper, gold, molybdenum, palladium, rhodium and iron. *J. Electrochem. Soc.*, **104**, 18-194 (1957).

# ELECTROCHEMICAL CO$_2$ REDUCTION

# CHAPTER 2

# Electrochemical CO$_2$ reduction

## 2.0. Introduction & motivation

The continuous growth of CO$_2$ emissions in the atmosphere is a major problem for our planet, and the awareness to limit the accumulation of this greenhouse gas is generally felt. An exciting strategy comes from the transformation of CO$_2$ into energy-dense molecules, like low-weight hydrocarbons, possibly produced with the aid of renewable energies. The electrochemical reduction of CO$_2$ has two-fold utility: it reduces the build-up of CO$_2$ and allows to store electrical energy in the form of free energy (i.e. chemical bonds of the formed products).

Non-noble metals play a major role in CO$_2$ electroreduction with copper being the most active material,[1] but its high activity is usually paired with a poor selectivity towards a single/few product. This lack of selectivity is historically one of the main drawbacks of electrochemical CO$_2$ conversion, with very few materials, mainly metals, that are particularly selective and active at the same time.[2] Among the various products that can be generated from CO$_2$ reduction, see section **I.4**,[3] of growing interest is the production of formic acid. Formic acid can be utilized either as fuel in Direct Formic Acid Fuel Cells,[4] as chemical for further chemical synthesis or as preservative in the textile and food industry, with the latter having the biggest share in its total worldwide consumption.[5] In the context of a hydrogen economy outlined in the introduction, it is fundamental to develop easy and viable hydrogen storage systems. In light of its high volumetric hydrogen density, low toxicity and liquid nature, formic acid is a promising candidate also for this kind of application.[6] Formic acid is nowadays produced mainly by the combination of methanol and CO with the aid of a strong base.[7] Another possibility comes from the homogeneous hydrogenation of CO$_2$, usually carried out in alkaline solutions with the aid of transition metal catalysts to overcome thermodynamic and kinetic limitations or at elevated pressure.[8,9] There are also examples of CO$_2$ hydrogenation in acidic solutions that has the advantage to avoid the base neutralization at the end of the reaction to yield HCOOH.[6,10] In this context, the electro-reduction or electro-hydrogenation of CO$_2$ in acidic media can be an appealing solution for formic acid

synthesis. Eq. **2.1a-c** describe $CO_2$ reduction to formic acid, via the formation of the $CO_{2\ (ads)}$ adsorbate.

$$CO_2 \rightarrow CO_{2(ads)}$$ Eq. **2.1a**

$$CO_{2(ads)} + e^- \rightarrow CO_{2(ads)}^-$$ Eq. **2.1b**

$$CO_{2(ads)}^- + HA + e^- \rightarrow HCO_2^- + A^-$$ Eq. **2.1c**
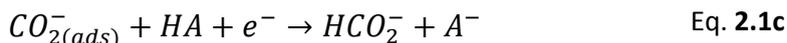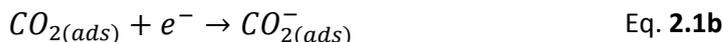
This mechanism has been proposed for formic acid production on metal electrodes and it holds as a general case with HA being a proton donor, whether $H_2O$ or $H_3O^+$, and $A^-$ being the respective deprotonated species. Early studies in aqueous solutions showed that p-block metals including Sn,[11] In[12] and Pb[13] reduce $CO_2$ to formic acid, or formate depending on the pH. However, a major drawback of these materials is the absolute overpotential required, in general greater than 1 V. More recently Kanan and coworkers have reported the selective production of formic acid on Pd/C electrodes at potentials very close to the thermodynamic value for [$CO_2/HCO_2^-$].[14] The ability of Pd to generate formate was known since the 90s,[15-18] but again with the need of high overpotential that ended up in low Faradaic Efficiencies. The poor selectivity was related to the competitive reaction of water reduction following Pd-hydride formation. When these side-reactions are minimized by the application of a very low overvoltage, formate are quantitatively produced accordingly to an electro-hydrogenation mechanism. The authors, indeed, ascribed the large discrepancy of Faradaic Efficiency to a different mechanism that would lead from $CO_2$ to $HCO_2^-$. Unlike other metals, on Pd the process would not involve a direct electron transfer to $CO_2$, highly endoergonic (Eq. **2.1b**), but would proceed via the electrochemically generated Pd-H species, a more easy-to-form intermediate. The entire process (Fig. **2.1**) requires much less driving force to happen, and would explain the almost quantitative formate production at low applied voltages.
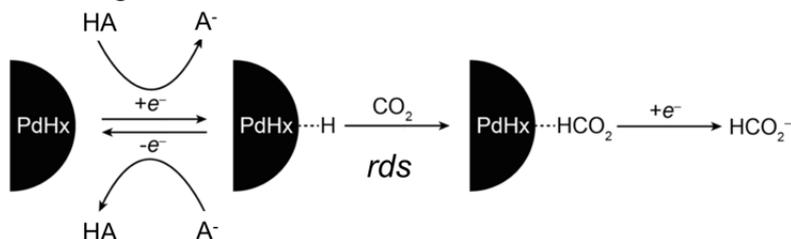


**Figure 2.1:** Proposed electro-hydrogenation mechanism for $CO_2RR$ on Pd NPs at very low overpotentials. The reductive adsorption of hydrogen atoms on Pd is the first step for formate synthesis, which then occurs via hydrogenation of $CO_2$ (*rds*). Adapted from ref. [14].

The particularity of the reaction that leads to formate was also observed by Koper and coworkers on copper electrodes.[19] They found that the production of formate peaks in a potential region where other $CO_2$ reduction products like ethylene and methane are absent; vice versa, when the latter are present formate is not. The authors correlate this fact to the presence of a distinct reaction pathway for formate production. The formation of a CO intermediate, which is known to be the precursor for making methane and ethylene,[20,21] occurs but it is likely to happen at more negative potentials. These observations suggest that the process for formate/formic acid can be very selective if the parallel and competitive hydrogen evolution reaction could be suppressed.

Starting from this general picture and knowing the potential role of formic acid in the future of FCs, it is here highlighted a possible approach towards the selective electrochemical reduction of $CO_2$ to formic acid by the rational design of a nanostructured material. If, in the previous examples, electrocatalysis was played by metal electrodes, in the following section carbon-based nanocomposite materials, **MWCNT@CeO₂** and **MWCNT@Pd/CeO₂** will be the main actors. They consist of functionalized multiwall carbon nanotubes, MWCNT, mutually integrated with cerium oxide, $CeO_2$, with/without Pd nanoparticles into a single nanostructure. Their electrochemical characterization, together with their activity towards $CO_2$ reduction, are herein reported.

## 2.1 Nanostructures for $CO_2$ reduction

The nanocomposites **MWCNT@CeO₂** and **MWCNT@Pd/CeO₂** have been synthetized at the University of Trieste by collaborators in the network of the PRIN/FIRB "Nanosolar" project.[22] The *CNG* group of Prof. Maurizio Prato and the *MEE* group of Prof. Paolo Fornasiero performed the synthesis of the nanostructures, as was the case for the electrocatalysts presented in Chapter 1.

The architecture of these nanocomposites is analogous to the systems described in the previous Chapter, where a backbone of functionalized multiwall carbon nanotubes (f-MWCNTs) was embedded inside a mesoporous layer of $TiO_2$. Since the synthetic strategy is rather flexible and allows to some extent to change the nature of the oxide material. In the case of $CO_2RR$ of major interest is the application of a uniform $CeO_2$ shell around the MWCNTs. The motivation for the choice of $CeO_2$ is two-fold: cerium oxide has been shown to adsorb $CO_2$ stably on

different crystal facets[23,24] and furthermore it has the ability to form hydrides species.[25] In the context of electrochemical $CO_2RR$ to formate/formic acid, where the presence of hydride species is deemed fundamental in driving the reaction at low overpotentials, the use of $CeO_2$ is therefore highly promising.

## 2.1.1 Synthesis of the nanostructures

As building blocks for the synthesis of **MWCNT@CeO₂** and **MWCNT@Pd/CeO₂**, oxidized MWCNTs (MWCNT-ox), functionalized Pd NPs (with 11-mercaptoundecanoic acid) and cerium alkoxide, in a combination of ex-situ and in situ methods were used. The resulting hierarchical nanocomposites are formed of onion-type core–shell Pd@CeO₂ particles supported on conducting MWCNTs (Scheme **2.1**).[22]
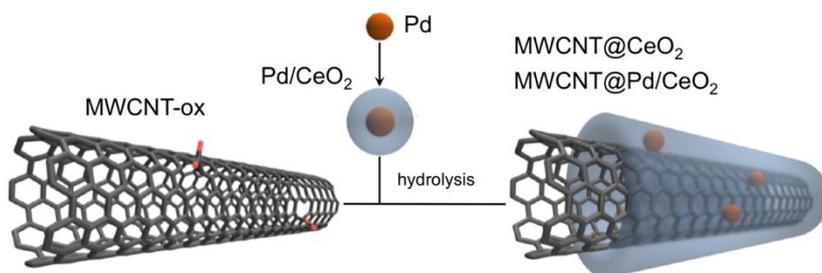


**Scheme 2.1:** Schematic representation of **MWCNT@CeO₂** and **MWCNT@Pd/CeO₂** synthesis. Adapted from ref. [22]

The synthetic strategy for the preparation of the nanocomposites is analogous to what reported in Chapter 1, but in this case, Pd NPs and MWCNTs-ox bind to cerium alkoxide. More in detail, first the Pd/CeO₂ building block is prepared by reacting the Pd NPs particles with cerium alkoxide. This assembly is then connected to the MWCNTs by reaction of the carboxyl groups of the MWCNTs with the alkoxide linkages that are available on Pd/CeO₂ particles. The MWCNTs induce crystallization of the oxide layer at room temperature, and after hydrolysis of the remaining alkoxide groups uniform composites are obtained (see Ref. [22] for further details).

As it can be seen in Fig. **2.2**, HR-TEM and EELS images of the samples reveal the uniform and regular formation of a mesoporous CeO₂ shell around the carbon nanotubes. The thickness of the oxide shell is in the order of 10 nm and, as mentioned in section **1.1,** it can be tuned by varying the content of MWCNTs-ox

and the alcoxide precursors. However, in this study the amount of MWCNTs-ox in the reagent mixture for both **MWCNT@CeO$_2$** and **MWCNT@Pd/CeO$_2$** was kept constant to the value of 15% by weight.
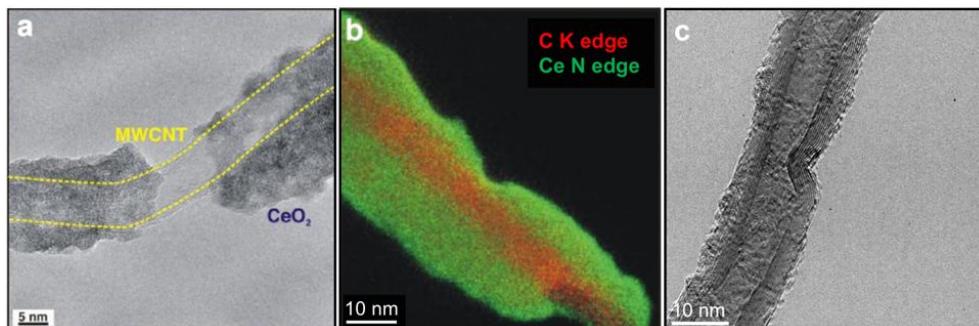


**Figure 2.2:** HR-TEM images for **MWCNTs@CeO$_2$**. **a)** representative image of a selected area showing partially exposed MWCNTs. **b)** The EELS mapping of C and Ce atoms confirms the uniform coverage of the MWCNTs with a shell of CeO$_2$. **c)** HR-TEM of a uniformly covered sample where it is evident the MWCNTs-backbone, as well as the nanocrystalline nature of the oxide shell. Adapted in part from ref. [22].

### 2.1.2. MWCNTs

As already pointed out in section **1.1.1,** the electronic properties of MWCNTs have been shown to be extremely beneficial for catalytic applications. MWCNTs have high specific surface areas and a very high conductivity for charge transport. These features are very compelling, especially for the field of electrocatalysis in which a good mobility of free charge is essential.[26]

In this study it is taken advantage of the peculiar electron mobility of MWCNTs to create a nanometric texture where charges can percolate, being accessible for electron transfer reactions. As it is shown, MWCNTs has the fundamental role to increase the electrons availability at the surface of CeO$_2$. In **MWCNT@CeO$_2$** and **MWCNT@Pd/CeO$_2$** the nanometric-thick CeO$_2$ shell is thin enough to allow efficient charge transport to the surface, otherwise limited in thicker and more insulating films.

### 2.1.3. CeO$_2$

Cerium oxide, ceria, is the fully oxidized, stoichiometric, oxide of cerium, the second lanthanide metal. At ambient pressure and from room temperature to 2500 °C (m.p.) fully oxidized CeO$_2$ adopts the ideal cubic fluorite crystal structure. A

remarkable feature of this oxide is the ability to maintain the same crystallographic structure (or phase) even when a very high concentration of lattice defects (oxygen vacancy) is present.[27] Indeed, under reducing conditions portion of the $Ce^{4+}$ atoms convert to the 3+ oxidation state, and the charge of the resulting electrons is balanced by oxygen vacancies. Furthermore, these oxygen vacancies have a very high mobility that combined with a moderate electron mobility, especially at high temperature, make ceria a suitable material for catalytic and electro-catalytic applications.[28] For these reason ceria is often used as a support for oxidative catalysis, like the oxidation of CO in automotive exhaust catalysts and in the water–gas shift reaction.[29]

For its peculiar mixed ionic and electronic conductivity, $CeO_2$ is also commonly studied as electrolyte in SOFCs[30,31] and has emerged as an attractive redox active material for two-step thermochemical cycling, displaying rapid kinetics that mainly arise from the presence of mixed-valence oxidation states.[32]

In the context of electrochemical $CO_2$ reduction, it is here investigated the role of $CeO_2$ as a valid platform for the simultaneous $CO_2$ adsorption and hydride formation. Several recent works have reported about the interaction of $CO_2$ on ceria surfaces,[23,24] partially motivating this study. The adsorption of $CO_2$ generates adsorbed carbonaceous species that have been identified both experimentally and theoretically. In general, the adsorption energy mainly depends on the crystal facet of the oxide and it was found to be higher in the case of reduced ceria, $CeO_{2-x}$,[33] species that is likely to be generated at the electrodes during $CO_2$ reduction.

## 2.1.4. Pd

The flexibility of the synthetic protocol allows to easily build nanostructures where the metal Pd nanoparticles are present or not. Thanks to the possibility to generate ex-situ the various constituents, simply by preparing the $Pd/CeO_2$ or its metal-free analogous $CeO_2$, it is possible to synthetize **MWCNT@CeO$_2$** or **MWCNT@Pd/CeO$_2$**. Either ways do not affect the total coverage of the MWCNTs, nor the crystallinity of $CeO_2$, whose mesoporosity makes the Pd nanoparticles accessible. With such integrated architectures it is possible to unravel the effect of Pd nanoparticles on the electrochemically driven $CO_2$ reduction. As previously outlined, the generation of Pd-hydrides favors formate production at low overpotential on carbon supported Pd NPs.[14] The same concept is applied in this study, where smaller Pd

NPs are embedded in a complex nanocomposite. The overall effect on the catalytic activity stems from their combination together with MWCNTs and the rich surface chemistry of $CeO_2$.

## 2.2. MWCNT@CeO₂: Electrochemical characterization and CO₂ reduction.

To study the electrochemical properties of both **MWCNT@CeO₂** and **MWCNT@Pd/CeO₂** (the latter reported in the next paragraph) the following procedure was adopted in order to prepare the electrodes. Thin compact films of **MWCNT@CeO₂** are prepared by drop casting 100 µl of the respective methanol suspension (1.6 mg powder : 1 ml $CH_3OH$) on bare GC disc electrodes (Ø = 3 mm). The suspensions are stirred for at least 48 hours before deposition, drop-cast in ten aliquots and then allowed to dry for 24 hours to remove any possible residual solvent. The amount of **MWCNT@CeO₂** deposited on the GC electrode surface is estimated to be 40 µg, with a contribution of $CeO_2$ of 34 µg. Before each drop-cast the GC electrodes have been meticulously polished with an alumina paste of subsequent finer grain size: 1 µm, 0.3 µm and 0.05 µm. During the cleaning procedure the electrodes are rinsed with doubly distilled water, sonicated with a bath sonicator and rinsed again with water and acetone.

The electrochemical characterization of the so-prepared nanostructured films has been performed in a custom made three electrodes electrochemical cell specifically designed for the aim of this work (see Appendix for a detailed project and description of the cell). The electrochemical characterization has been done in different aqueous electrolytes, namely PB 0.1 M, Bicarbonate Buffer 0.5 M and an acid $HNO_3$ solution 0.1 M. Depending on the scope of the experiments, Ar or $CO_2$ have been bubbled into the solutions for at least 25 minutes before doing any characterization.

Each measurement has been done with a Ag/AgCl 3M reference electrode, whose potential have been validated before and after each set of experiments with a Standard Calomel Electrode ($E_{SCE}$ = +0.246 vs. NHE) in use for this specific purpose. Depending on the measurements, potentials are reported versus Ag/AgCl 3M, or in he RHE scale ($E_{RHE}$ = $E_{NHE}$ - 0.059*pH) scale. All $J$ values are calculated on a geometric area basis. The contribution of the real electroactive surface is taken into account in the calculation of the TOF (see later for a comprehensive description). Unless

otherwise specified, all chemicals have been used as received, without any further purification step.

## 2.2.1 Electrochemical characterization in Phosphate Buffer

The activity of **MWCNT@CeO₂** towards electrochemical $CO_2$ reduction in PB 0.1 M is shown in Fig. **2.3**, where representative CVs of a $CO_2$-saturated solution are reported. Despite the large cathodic current observed during the first scans, the voltammetric response decreases with potential cycling, and after 20 cycles almost no faradaic current is present anymore. This sort of deactivation of the electrode surface is a systematic feature, seen throughout a series of different samples prepared from different batch suspensions, hence has to deal with an effect of the electrolytic solution.
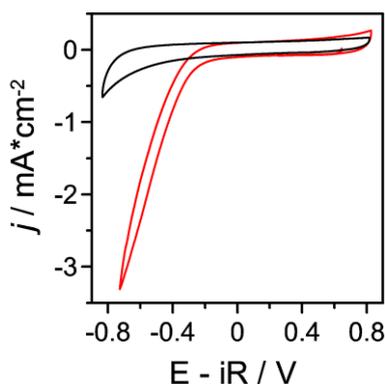


**Figure 2.3:** Electrochemical activity of **MWCNT@CeO₂** for $CO_2$ reduction. 1st (red line) and 20th (black line) CV scans of **MWCNT@CeO₂** in PB 0.1 M, scan rate 50mV/s. Potentials are reported vs. RHE and are corrected for the uncompensated resistance $R_S$ ($R_S$ determined by EIS).

In a comprehensive paper, Cummings *et al.*[34] reported about the rich electrochemical activity of nanoparticulate $CeO_2$ films in PB. The authors correlate the peculiar electrochemical behavior of $CeO_2$ to several chemical reactions that occur at the electrode surface (Eq. **2.2**, **2.3**).

$$2CeO_{2(surface)} + 2e^- + 2H^+ \rightarrow Ce_2O_{3(surface)} + H_2O \qquad \text{Eq. } \mathbf{2.2}$$

$$Ce_3(PO_4)_{4(surface)} + 3e^- + 3H^+ \rightleftharpoons 3CePO_{4(surface)} + H_3PO_4 \quad \text{Eq. } \mathbf{2.3}$$
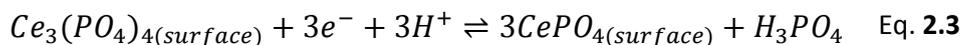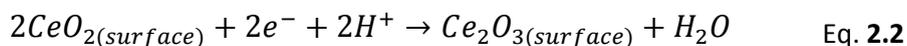
When $Ce^{4+}$ is reduced to $Ce^{3+}$ (Eq. **2.2**) in the presence of phosphate, a slow chemical equilibrium that lead to $CePO_4$ formation takes place (Eq. **2.3**). Reduction of $Ce^{4+}$ to $Ce^{3+}$ (E ≤ +0.3 $V_{RHE}$)[35] can be easily obtained under conditions of cathodic

polarization (i.e. the same of electrochemical $CO_2$ reduction) and the slow build-up of a $CePO_4$ layer finally lead to electrode passivation. The formation of this surface equilibrium involving phosphate anions is however a major drawback with respect to the electrochemical $CO_2$ conversion in this particular electrolyte. Both $Ce^{4+/3+}$ reduction and $CO_2$ reduction occur in the scanned potential window, but after complete formation of surface $CePO_4$ also $CO_2$ reduction is suppressed.

The occurrence of the processes described by Eq. **2.3** can be monitored and quantified by CV through the detection of the redox peak (Eq. **2.3**) with $E_{1/2} = +0.5$ V vs. AgCl[34] (process "A" in Fig. **2.4a**) and evaluation of the corresponding charge.

a)                          b)
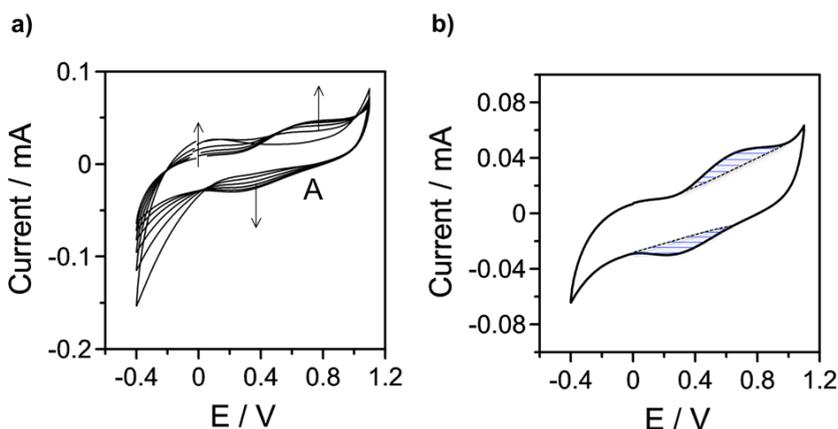
**Figure 2.4: a)** CVs in Phosphate Buffer of **MWCNT@CeO$_2$**. The scans n° 1-4-7-10-13 and 16 are plotted. **b)** Plot of the 16th cycle, with highlighted the integrated charge attributed to the process of Eq. **2.3**. Potentials are reported vs. Ag/AgCl 3M. Scan rate = 50 mV/s, PB 0.1 M, pH = 6.8.

Therefore, while the formation of such species leads to surface passivation (Fig. **2.3**) and is detrimental vis-à-vis the electrocatalysis of $CO_2$ reduction, the quantification of process A in Fig. **2.4a** allows to estimate the amount of electrochemically active cerium oxide, a piece of information needed for the turnover frequency (TOF) determination (see section **2.2.2.1**). The integration of the corresponding voltammetric peaks (Fig. **2.4b**) resulted to a charge of 43 µC, indicating that ~20% of the total amount of $CeO_2$ deposited on the GC electrode can be reduced/oxidized electrochemically.


## 2.2.1.1 Comparison with nanocrystalline CeO$_2$

A striking difference can be observed when comparing the CVs in PB for **MWCNT@CeO$_2$** and nanocrystalline **CeO$_2$** (Fig. **2.5a**). Films of nanocrystalline **CeO$_2$**

are prepared with the same procedure as for **MWCNT@CeO₂**, adjusting the amount of the drop-cast in a way that the same nominal coverage of cerium oxide is present on the electrode. In this way is possible to directly compare the electrochemical behavior of **MWCNT@CeO₂** and **CeO₂**. Comparison of the CVs (Fig. **2.5a**) shows how the redox process "A" at $E_{1/2}$ = +0.5 V vs. Ag/AgCl cannot be observed in **CeO₂** films. Moreover, the overall capacitive current is much lower in the latter case (see also Fig. **2.5b**). The suppression of any faradaic current is somehow surprising but reveals the fundamental role played by MWCNTs in promoting the charge transfer from the underlying glassy carbon electrode, through the nanocomposite film, to the surface of $CeO_2$ where electrons are available for electron transfer reactions.
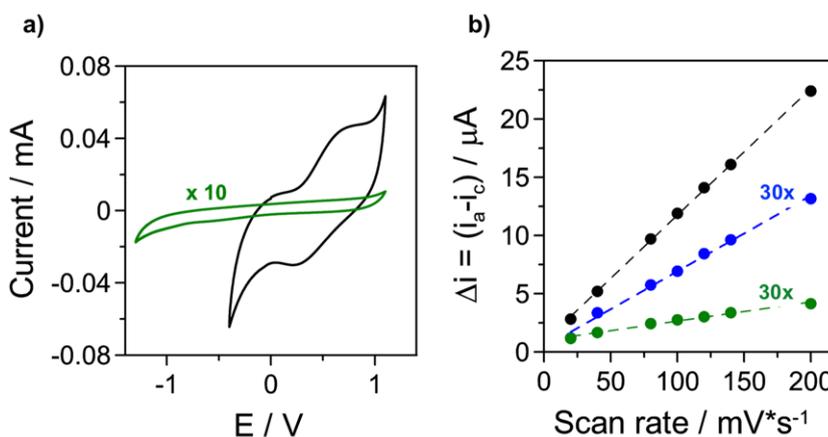


**Figure 2.5: a)** comparison between the CVs for **MWCNT@CeO₂** (black curve), **CeO₂** (green curve) in a potential region where $Ce^{4+/3+}$ reduction and the following slow chemical conversion to $CePO_4$ occur. Scan rate = 50 mV/s, PB 0.1 M, pH = 6.8. **b)** Capacitive currents for **MWCNT@CeO₂** (black dots), **CeO₂** (green dots) and a bare **GC** electrode (blue dots) in Ar-sat. solutions. Potentials are reported vs. Ag/AgCl 3M.

Thick films of nanocrystalline **CeO₂** are therefore unable to sustain redox processes at the surface, while in the case of **MWCNT@CeO₂** the oxide shell around MWCNTs is thin enough to enable electron transfer. Up to now it is not completely clear the reason for this remarkable behavior, whether the induction of electronic defects in the oxide shell (as observed in the case of **MWCNT@Pd/TiO₂** in Chapter 1), an increased efficiency of electron tunneling, or other possible explanations.

The huge decrease of electrical capacity (C) observed in the CVs of **CeO₂** films with respect to **MWCNT@CeO₂** was attributed mainly to the higher specific surface area

of the latter. A more detailed analysis of the capacitive behavior for the two systems is given in Fig. **2.5b**, where the capacitive currents ($\Delta i$) are evaluated as a function of the scan rate ($v$). The capacitive contributions $\Delta i$ have been determined by CV at OCP from the difference of the anodic and cathodic currents registered when the potential was scanned positive (+30 mV) or negative (-30 mV) of the OCP. By scanning the potential at various scan rates in a region where only capacitive currents are present (i.e. no faradaic reactions occur) it is possible to determine the electrode capacity via the evaluation of the $\Delta i/v$ slope, that resulted to be 1.6 mF/cm$^2$ and 9 µF/cm$^2$ for **MWCNT@CeO$_2$** and **CeO$_2$** respectively. As can be seen in Fig. **2.5b**, the capacity of **CeO$_2$** is even lower than that of a bare **GC** electrode (32 µF/cm$^2$). This general behavior for CeO$_2$ is then not only related to a reduction of the electroactive area, but also reflects changes in the electronic properties of the oxide film. It is well known that layers of insulators (e.g. oxide, self-assembly monolayer, etc.) on top of metallic electrodes reduce the capacitive current.[36] It is likely that with thick films of un-doped nanocrystalline **CeO$_2$** the insulating behavior prevails and the surface capacitance is reduced by an increased distance between the regions of excess charge ($C_{dl} = \frac{\varepsilon\varepsilon_0}{d}$, accordingly to the Helmholtz model of the electrical double layer).

Again, the essential role of MWCNTs to provide a good electrical conductivity and accessibility of CeO$_2$ in the nanostructure is demonstrated.


## 2.2.2 Electrochemical characterization in Nitric Acid

Due to the detrimental absorption of phosphate anions at the surface of partially reduced CeO$_{2-x}$ that inhibits CO$_2$ reduction, a different electrolyte with a much lower interaction with Ce$^{3+}$ lattice sites is preferred. Nitrates are more innocent toward complexation with Ce$^{3+}$, and for this reason aqueous solutions of HNO$_3$ 0.1 M have been chosen to characterize the activity of **MWCNT@CeO$_2$** for CO$_2$ reduction.

The absorption and interaction of CO$_2$ on **MWCNT@CeO$_2$** in HNO$_3$ 0.1 M was investigated by electrochemical impedance spectroscopy (EIS) and by CV, following the different behavior of the surface capacitance in the presence or absence of dissolved CO$_2$ in solution. With CV, the method previously described was applied, based on the evaluation of capacitive currents at various scan rates. In Fig. **2.6a** are

reported representative CVs for **MWCNT@CeO₂** from which the capacitive currents at different scan rate have been derived and plotted in Fig. **2.6c** to estimate the total capacitance. A clear higher double-layer capacitance is present when the electrolyte is saturated with $CO_2$ (4.1 mF/cm²) rather than with argon (2.4 mF/cm²). Analogously, significant changes in the EIS spectra upon saturation with $CO_2$ were present. From the Bode plot of Fig. **2.6d** it is possible to observe two different time constants in the absence of dissolved $CO_2$, that merge in a single one when $CO_2$ is present. It is also possible to notice that the solution resistance (Log|Z| values at high frequencies) under $CO_2$ saturation increases by almost 50 Ohm (78 Ω vs. 123 Ω). This effect is probably caused by the surface absorption of $CO_2$ molecules that increases the electrode's resistivity.
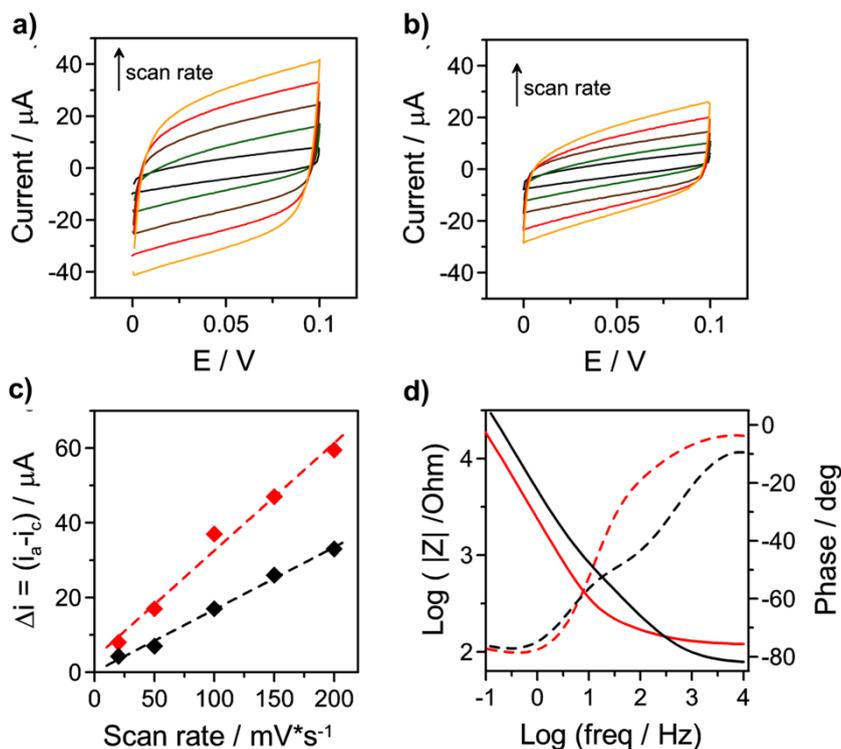


**Figure 2.6:** representative CVs of **MWCNT@CeO₂** in **a)** CO₂-sat. and **b)** Ar-sat. HNO₃ 0.1 M solution. The CVs were recorded in the potential range +/- 50 mV vs. OCP ($E_{OCP}$ = +0.05 V AgCl) at a scan rate of 20, 50 100, 150 and 200 mV/s. Potentials are reported vs. Ag/AgCl. **c)** Capacitive currents as a function of the scan rate, calculated as $\Delta i = (i_a - i_c)$ and derived from CVs in a) and b). $CO_2$ (red) or argon (black) saturated solution. **d)** EIS spectra (Bode plot) for **MWCNT@CeO₂** at OCP in $CO_2$ (red) or Ar (black) saturated solution. Dashed lines refer to variations in the phase angle, while changes in the real component of impedance are displayed by continue lines. Electrolyte: HNO₃ 0.1 M.

Importantly, a quite different behavior is observed when cerium oxide is not supported on MWCNTs. As in the case of PB solutions, films of nanocrystalline **CeO₂** (again with the same nominal coverage of **MWCNT@CeO₂**) show much lower capacitance, which, additionally, is almost insensitive on the presence of $CO_2$ (Fig. **2.7a** and **2.7b**). Moreover, also in PB electrolyte the capacitance of **CeO₂** is lower than that of a corresponding bare GC electrode. As previously outlined, such behavior is attributed to a decrease in the electrochemically accessible **CeO₂** surface, associated with a much higher resistivity of the **CeO₂** nanocrystals in the absence of MWCNTs.
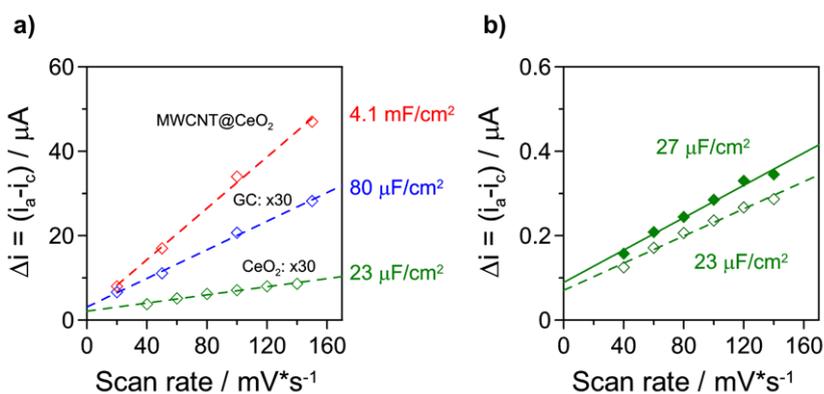


**Figure 2.7**: **a)** capacitive currents for **MWCNT@CeO₂** (red), **CeO₂** (green) and a bare **GC** electrode (blue) in CO2-sat. solutions. Note the magnification for **GC** and **CeO₂** plots (30x for both). **b)** capacitive currents for **CeO₂** in $CO_2$- (empty diamonds) and Ar- (filled diamonds) saturated $HNO_3$ solutions. Electrolyte: $HNO_3$ 0.1 M.

To study the activity of **MWCNT@CeO₂** toward $CO_2$ reduction LSV and CA experiments have been performed. LSV for **MWCNT@CeO₂**, the model system **CeO₂** and a bare **GC** electrode in a $CO_2$ saturated solution are displayed in Fig. **2.8a**.
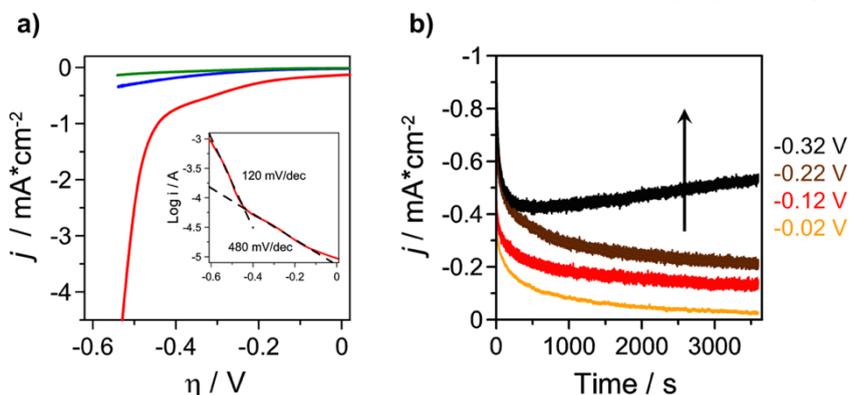
**Figure 2.8: a)** LSV for the nanostructured catalyst **MWCNT@CeO$_2$** (red line) the bare GC electrode (blue line) and **CeO$_2$** (green line) in a CO$_2$-saturated solution. Scan rate 2 mV/s. Potentials are reported vs. E' [CO$_2$/HCO$_2$H] = -0.2 V$_{RHE}$. Electrolyte: HNO$_3$ 0.1 M **b)** CA for **MWCNT@CeO$_2$** at different overpotentials. From orange to black, $\eta$ = -0.02 V, -0.12 V, -0.22 V, -0.32 V. Integration of these CA curves gives the charge of CO$_2$RR then used for the F.E. determination.

**MWCNT@CeO$_2$** displays much higher cathodic currents than both CeO$_2$ and GC, with the difference being already notable at $\eta$ as low as 150 mV. By contrast, the nanocrystalline oxide **CeO$_2$** does not shows any significant faradaic current in the entire potential range. Notice that in the plots of Fig. **2.8a** (and following) the overpotential is reported with respect to the standard potential for the reduction of CO$_2$ to formate/formic acid, i.e., $\eta$ = E$_{app}$ – E' [CO$_2$/HCO$_2$H] (with E' [CO$_2$/HCO$_2$H] = -0.2 V$_{RHE}$).[14] Importantly, the current associated to CO$_2$ reduction remains stable over repetitive cycling (up to 25 cycles), meaning that surface passivation by complexation of Ce$^{3+}$ does not occur in this acidic electrolyte. The two distinct slopes of the polarization curve for **MWCNT@CeO$_2$** may reflect the occurrence of different processes (inset of Fig. **2.8a**). At more negative potentials HER is the predominant process. As explained in the previous section, the reduction of cerium oxide to its partially reduced form CeO$_{2-X}$ is easily obtained (E $\leq$ 0.3 V$_{RHE}$) and it is thought to be involved in the mechanism of CO$_2$ reduction. The cathodic current at low overpotentials is then likely to arise from multiple concomitant processes that involve electron transfer to the oxide and to CO$_2$. Recent DFT calculations have shown that the binding energy of CO$_2$ adsorption on Ce$^{3+}$ sites is much higher than on stoichiometric CeO$_2$ (Ce$^{4+}$ sites only).[23,24] This is notably, since Ce$^{4+}$/Ce$^{3+}$ reduction takes necessarily place at the applied potentials and it is therefore possible the occurrence of a virtuous cycle where the *in-operando* generation of the non-stoichiometric oxide (richer in Ce$^{3+}$ atoms) can actively promote CO$_2$ conversion.

To confirm these hypotheses and especially the actual production of formate/formic acid, analysis of the reaction products has been performed and the results are reported in the following section. To generate detectable amount of products and to address the long-term stability of the nanocomposite, potential-controlled electrolysis of 1 hour were performed in a three electrode cell specifically designed for this work, as described in the Appendix. In such cell, the counter electrode was separated from the bulk solution by a porous frit so as to

avoid degradation of the generated products. In Fig. **2.8b** CA experiments at various applied potentials are shown.

The production of formic acid by $CO_2$ reduction is confirmed by ionic chromatography analysis of the liquid phase after potentiostatic electrolysis (see Appendix for details). After each electrolysis, small amounts of the solution (2 ml) were extracted from the electrochemical cell and immediately analyzed.

| | Analysis #1 / a.u. | Analysis #2 / a.u. |
|---|---|---|
| # 1 ($\eta$ = -0.02 V) | 3.041 | 3.085 |
| # 2 ($\eta$ = -0.12 V) | 2.872 | 2.891 |
| # 3 ($\eta$ = -0.22 V) | 2.137 | 2.133 |
| # 4 ($\eta$ = -0.32 V) | 0.335 | 0.258 |

**Table 2.1:** formic acid detection by I.C. after potentiostatic electrolysis for **MWCNT@CeO₂**. The mean value of two subsequent analyses, converted to concentration of formic acid, has been used for the calculation of faradaic efficiency and turnover frequency (see later). $\eta$ are referred to the relevant thermodynamic potential E′ [$CO_2$/$HCO_2H$].

Product analysis revealed increasing amounts of formic acid as $E_{app}$ is made less and less negative thus approaching the thermodynamic value. This is noteworthy since it confirms what reported by Kanan and coworkers[14] who could detect the highest amounts of formate (almost quantitative production) on Pd NPs at very low overpotentials. The hypothesis is that the mechanism that lead to formate synthesis is somehow similar to what suggested by Kanan. In that paper the formation of hydride species is thought to be a key step in $CO_2$ electro-hydrogenation; also in this case the same situation may hold, with cerium dioxide as the source of hydrides. Cerium hydride is a very reducing species, usually obtained at high temperatures under $H_2$ pressure. Its possible formation under the conditions of the experiments reported above could mediate $CO_2$ reduction via an electro-hydrogenation mechanism. The very high Tafel slope (i.e., slow kinetics) in this potential region may be an indication of the rather slow formation of Ce-hydride (which involves hydrogen absorption).

On the basis of our results, **MWCNT@CeO₂** would then behave similarly to the enzyme formate dehydrogenase,[37] since it would be able to drive the conversion of $CO_2$ to formic acid very close to the thermodynamic threshold.

## 2.2.2.1 Determination of Faradaic Efficiency and Turnover Frequency for formic acid production.

The determination of F.E. for formic acid production is obtained by comparing the amount of detected product with the charges exchanged by the nanocomposite electrode **MWCNT@CeO₂** during electrolysis (Eq. **2.4**). The F.E. at overpotential $n$ is thus defined as follows:

$$(F.E.)_n(\%) = \frac{x_{HCO_2H,n} * F * m}{Q_{tot,n}} \qquad \text{Eq. } \textbf{2.4}$$

where $x_{HCO_2H,n}$ are the moles of formic acid produced as determined by I.C., $F$ is the Faraday constant, $m$ the number of electron needed to produce one molecule of formic acid and $Q_{tot,n}$ the total amount of charge integrated from the CA experiments. Representative CA for **MWCNT@CeO₂** whose integration gives $Q_{tot,n}$ are reported in Fig. **2.8b**. The obtained values are plotted in Fig. **2.9a**. The calculated F.E. for formic acid production reaches values as high as 55 % at overpotentials as low as -0.02 V. It is worth mentioning that the calculated F.E. cannot ever reach 100% due to the contribution from $Ce^{4+}/Ce^{3+}$ reduction to the overall cathodic charge $Q_{tot,n}$ recorded from CA. Higher F.E. values may be foreseen on longer time scales and/or by maximizing the contribution of electroactive $CeO_2$ via an appropriate improvement of the surface morphology. The drastic drop of F.E. for formic acid synthesis at more negative potential occurs for the concomitant increasing contribution of HER, a kinetically favored process especially in acidic solutions.

The TON (moles of product per moles of catalyst) and TOF (TON/time) are usually considered as figures of merit for catalytic systems and a way to describe the ability of a catalyst to speed up the process. A possible approach to estimate the TOF of the heterogeneous catalyst **MWCNT@CeO₂** for formic acid synthesis is to relate the "moles of product" to the charge exchanged during electrolysis, and the "moles of catalyst" to the amount of electroactive material, rather than to the total amount of catalyst present. All the charges are of course weighted for the F.E. for formic acid production. Doing this, it is possible to normalize the activity on an electroactive area basis, obtaining an intrinsic descriptor of the electrocatalytic activity. TOF is then a more accurate way for comparisons than other approaches, very common in the electrochemical community, based on geometric current

densities. It is indeed a valuable tool to compare materials with very different surface areas and with catalytic sites of different nature. Eq. **2.5a** and **2.5b** give a better idea of this approach, that also enable to relate the TON/TOF to the applied overpotential.

$$TON_n = \frac{Q_{n,red}^{CO_2}(C)}{Q_{CeO_2}(C)} * (F.E.)_n \qquad \text{Eq. } \textbf{2.5a}$$

$$TOF_n(h^{-1}) = \frac{TON_n}{time\ (h)} \qquad \text{Eq. } \textbf{2.5b}$$

where $Q_{n,red}^{CO_2}$ is the charge integrated from CA experiments at the potential $n$, $Q_{CeO_2}$ is the normalization factor for the amount of electroactive **MWCNT@CeO$_2$** as determined by CV, *time* is the length of each electrolysis (usually one hour long) and $(F.E.)_n$ is the faradaic efficiency for formic acid production at each potential $n$. The obtained TOF$_n$ values (Fig. **2.9b**) reflect the opposite trends of F.E., that increases, and integrated charges, that decreases, when E$_{app}$ is made more positive. At low $\eta$ the charge $Q_{n,red}^{CO_2}$ is the lowest, but it is predominantly associated to formic acid production rather than to HER as in the high overpotential region. These opposite trends result in TOF values around 100-200 h$^{-1}$ in the entire potential window.
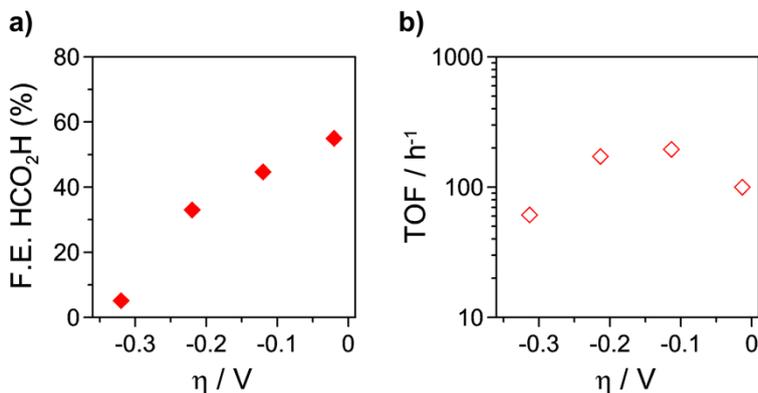


**Figure 2.9: a)** Faradaic Efficiency of **MWCNT@CeO$_2$** for formic acid production as a function of the overpotential (η) where η = E$_{app}$ - E' [CO$_2$/HCO$_2$H]. E' [CO$_2$/HCO$_2$H] = -0.2 V$_{RHE}$. **b)** Turnover Frequency for HCO$_2$H production calculated as in Eq. **2.5b** at different overpotentials η.

The observed decrease in F.E. for HCO$_2$H production at high overpotential (Fig. **2.9a**) is also evidenced by the change of the slope in a Tafel plot (Fig. **2.10** and inset of Fig. **2.8a**). Currents data in Fig. **2.10** are derived both from LSV (red solid line) or from steady-state CA measurements (red diamonds). In the potential region close

to the thermodynamic value E' [$CO_2$/$HCO_2H$], both methods are consistent and give the same slope. As the potential is made more cathodic, the change of the slope reflects a transition between a kinetic limited region with slope of 480 mV/dec, where the production of formic acid is higher, to one with more facile kinetics, slope of 120 mV/dec, associated to a predominant HER. In the "low overpotential" region, the occurrence of multiple coupled simultaneous processes that cooperate together toward $CO_2$ reduction (i.e. adsorption of $CO_2$/$H^+$ on $CeO_2$ and $Ce^{4+}$/$Ce^{3+}$ reduction) limits the kinetics, but is responsible of the highest production of formic acid. This results in a higher Tafel slope, that may also result from the non-optimal distribution of active sites onto the catalyst surface, associated to the presence of different redox states of $CeO_2$ and to multiple surface redox couples/functional groups.[38] In the "high overpotential" region hydrogen evolution becomes the dominant process: the corresponding Tafel slope of 120 mV/dec, suggests several possible rate-limiting steps with kinetics limited by a slow Volmer adsorption step ($H^+ + e^- \rightarrow H_{ads}$), plausible with the competition between $H_{ads}$ and $CO_{2(ads)}$ for the same sites on the oxide surface.
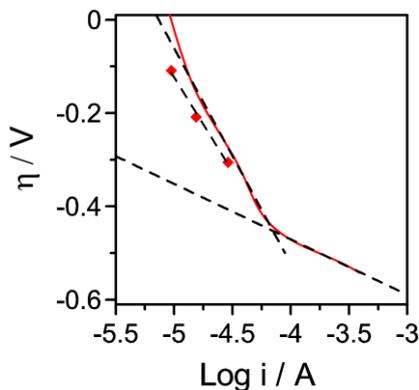


**Figure 2.10:** Tafel plot for **MWCNT@CeO₂** extracted from the LSV data of Fig. **2b** (red solid line), scan rate = 2 mV/s. Red diamonds refers to current data obtained from CA experiments. Electrolyte: $HNO_3$ 0.1 M. $\eta = E_{app}$-E' [$CO_2$/$HCO_2H$], where E' [$CO_2$/$HCO_2H$] = -0.2 $V_{RHE}$.

As pointed out previously the F.E. obtained with the proposed approach would never reach a value of 100 %, due to the initial contribution of $Ce^{4+/3+}$ reduction to the overall charge, $Q_{n,red}^{CO_2}$. One possibility to limit this artifact is to increase the time scale of electrolysis, or to subtract the charge related to $Ce^{4+/3+}$ reduction. The latter is not a straightforward approach, because it is not clear at this time if $Ce^{3+}$, besides enhancing the local $CO_2$ concentration, plays also an active role in the catalytic

cycle. If $Ce^{3+}$ would donate electrons to absorbed $CO_2$, it would also become available again for further reduction, generating a positive feedback of charge that at the end reduce the F.E. Further investigations are thus needed to clarify the role of $Ce^{3+}$ and to determine the precise contribution of $CeO_2$ reduction to the overall charge, and then to accurately determine the F.E. Higher faradaic efficiencies may also be obtained reducing surface inhomogeneity and maximizing the activity of $CeO_2$ to absorb and convert $CO_2$.

## 2.2.3 Electrochemical characterization in Bicarbonate buffer

The ability of **MWCNT@CeO₂** to generate formic acid has also been studied at near-neutral pH in bicarbonate buffer solutions. This also allowed to correlate the efficiency of $CO_2$ conversion to formic acid with the availability of protons in solution and the possible involvement of hydrides formed in the ceria layer.

In light of the passivation of **MWCNT@CeO₂** in PB, bicarbonate buffer was chosen to study the electrochemical $CO_2$ reduction at neutral pH. When $CO_2$ is purged in solution in the presence of an alkaline electrolyte, or simply a bicarbonate salt, the formation of a bicarbonate buffer occurs. This buffer has the peculiarity to act as a reservoir for aqueous $CO_2$, even in the absence of dissolved $CO_2$ for the presence of the following equilibria:

$$CO_2 \rightarrow CO_{2(aq)} + H_2O \rightleftharpoons H_2CO_3$$

$$H_2CO_3 + H_2O \rightleftharpoons HCO_3^- + H_3O^+ \qquad \text{p}K\text{a}_1 = 6.35$$

$$HCO_3^- + H_2O \rightleftharpoons CO_3^{2-} + H_3O^+ \qquad \text{p}K\text{a}_2 = 10.33$$
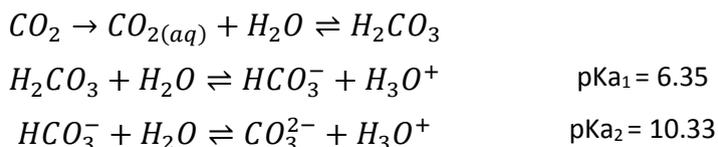
Adjusting the concentration of the salts, the pH of a bicarbonate buffer can be varied in the range 6 < pH < 10 (pH = 7.3 in this work where $[KHCO_3]$ = 0.5 M in a $CO_2$-saturated solution).

In a recent work on Sm-doped $CeO_2$ it has been reported how the electrochemical $CO_2$ reduction at high temperature proceeds via a stable carbonate intermediate, the coverage of which is coupled to the surface $Ce^{3+}$ concentration. The authors were able to shed light into the reaction mechanism thanks to an *in-operando* XPS study.[39] Following those findings, it is interesting to see also at RT and in aqueous solutions if and how $CO_2$ reduction is affected by the presence of carbonaceous species that may interact with partially-reduced cerium oxide.

As in the case of $HNO_3$ acid solutions, the F.E. for formate production has been evaluated by analysis of the electrolyzed solution by I.C. 2 mL aliquots have been collected from the electrochemical cell at the end of one-hour electrolysis at different $E_{app}$, while the gas phase has been analyzed during each measurement by online G.C. to determine the F.E. for gas products. During each electrolysis the gas phase is analyzed four times (one injection each 20 minutes, and the mean value are used for F.E. calculation)

As clearly seen in Fig. **2.11a** the F.E. for formate/formic acid production in $KHCO_3$ buffer 0.5 M is much lower than in the case of acidic solutions (2-3% vs. >40%). It is important to underline the presence of the same trend observed in acid, i.e. higher F.E. at the most positive potentials, that however in this case is shifted towards higher overpotentials (almost 400 mV more negative). Indeed, as evidenced in the CVs of Fig. **2.11b** the overpotential required for HER and/or $CO_2RR$ are rather negative (the dashed line refers to E' of $CO_2/HCO_2H$) and only small cathodic currents are detected. The intense cathodic peak observed in Fig. **2.11b** during the first scan and that disappears completely during the second one, is ascribed to $Ce^{4+/3+}$ reduction. The process occurs quite easily and one potential cycle is enough to reduce completely the electroactive $CeO_2$ on the electrode.
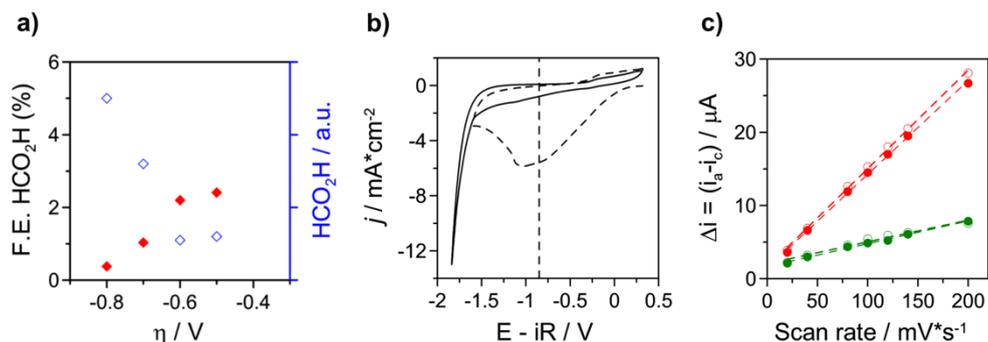


**Figure 2.11: a)** Faradaic Efficiency of formate production in $CO_2$-sat. $KHCO_3$ buffer solution for **MWCNT@CeO₂**. Each point corresponds to analysis of the liquid phase after 1-hour potentiostatic electrolysis at different overpotentials. $KHCO_3$ 0.5 M. **b)** Representative CVs for **MWCNT@CeO₂** in $KHCO_3$. The first (dashed line) and second (solid line) cycle are reported. Potentials vs. Ag/AgCl 3M and corrected for the uncompensated resistance. Scan rate = 50 mV/s. **c)** Double layer capacitance for **MWCNT@CeO₂** (black) and **CeO₂** (green) in Ar- (empty dots) and $CO_2$- sat (filled dots) $KHCO_3$ 0.5 M solutions.

Again, the reduction of F.E. for formate at more negative potentials is paralleled by an increased F.E. for HER that accounts for almost 100% of the total products at the

most negative potentials (not shown). No other gaseous $CO_2$ reduction products, like CO, ethylene or methane, have been indeed detected. These results are possibly another experimental evidence for the crucial formation and participation of hydrides in $CO_2$ reduction. Scheme **2.2** resembles the situation that likely occurs at the electrode surface, where $CeO_{2-x}$ mediates the hydrogenation of $CO_2$ to formate/formic acid.
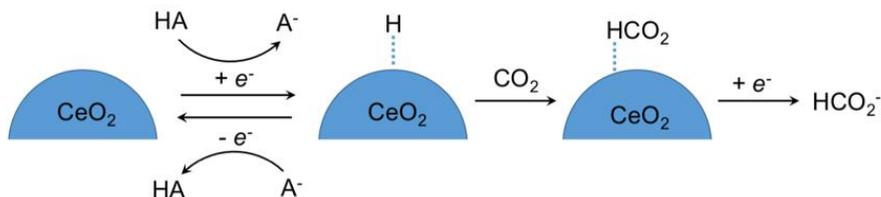


**Scheme 2.2:** schematic representation of $CO_2$ reduction on **MWCNT@CeO_2** where hydrides species formed on the surface of CeO2 mediate the electro-hydrogenation of $CO_2$ to formate/formic acid. This process is fostered in acid solution where the availability of free protons does not hinder the formation of such hydrides, whereas at neutral pH the conversion is more inefficient.

The obvious low availability of free protons (or HA in Scheme **2.2**) at neutral pH hinders the formation of hydrides on $CeO_2$ during cathodic polarization and results in a general low efficiency for formate production. Moreover, it has been found that the presence of carbonates does not improve $CO_2$ conversion. Probably the interaction of $CO_3^{2-}$ with $Ce^{3+}$ competes strongly with the adsorption of $CO_{2(aq)}$ (or its corresponding hydrated form $HCO_3^-$) and this decreases the efficiency for $CO_2$ conversion. This is also reflected by the negligible variation of $C_{dl}$ for **MWCNT@CeO_2** in a $KHCO_3$ electrolyte in either the presence or absence of $CO_2$ (Fig. **2.11c**). A comparison with the double layer capacitance of **CeO_2** confirms the general characteristic of higher $C_{dl}$ values for **MWCNT@CeO_2** (as observed in the other electrolytes), and also reveals no variation of $C_{dl}$ for **CeO_2** after saturation of the $KHCO_3$ buffer with $CO_2$.

## 2.3 MWCNT@Pd/CeO₂: Electrochemical characterization and CO₂ reduction.

In light of the results obtained with **MWCNT@CeO_2** it has been proposed the introduction of Pd nanoparticles within the nanostructure so as to increase the availability of hydrides on the electrode surface in a wide range of pH. Palladium is a very well known sponge for hydrogen, and for each Pd atoms it can accommodate

within its lattice almost one hydrogen atom in the form of hydrides.[40] Moreover, the ex-situ co-preparation of the $Pd/CeO_2$ building block and its incorporation around MWCNTs can be easily obtained with the synthetic protocol used. It is then possible to investigate the role of hydride species in $CO_2$ electroreduction for this class of nanocomposites, trying to uncouple the effects that the formation of hydrides on $CeO_2$ and/or Pd NPs have on $CO_2$RR.

The electrocatalytic performances toward $CO_2$ reduction for **MWCNT@Pd/CeO₂** are then studied and are here reported.

Films of **MWCNT@Pd/CeO₂**, prepared according to the procedures previously described, were studied in the same $HNO_3$ and $KHCO_3$ solutions.

### 2.3.1 Electrochemical characterization in Nitric Acid

The electrochemical characterization in $HNO_3$ is reported in Fig. **2.12**. LSV scans reveal how **MWCNT@Pd/CeO₂** displays high cathodic currents as evidenced by the high current density and the value of the onset potential of the black curve in Fig. **2.12a**. Reduction occurs already at positive overpotentials for formate reduction (i.e., at more positive potentials than the thermodynamic limit E' [$CO_2/HCO_2H$]), meaning that hydrogen evolution (E' at $\eta \sim +0.2$ V ) is the predominant process at such potentials. For comparison, the metal-free **MWCNT@CeO₂** shows comparable currents but shifted more negative by ~600 mV. It is interesting to note how for **MWCNT@Pd/CeO₂**, due to the strong contribution of HER, no processes associated to $CO_2$ conversion and $Ce^{4+}/Ce^{3+}$ reduction could be appreciated in the "low-overpotential region", as in the case of **MWCNT@CeO₂**. This enhanced activity of **MWCNT@Pd/CeO₂** for HER is clearly seen by analysis of the F.E. for formic acid synthesis (Fig. **2.12c** and related potentiostatic 1-hour electrolysis in Fig. **2.12d**). The production of formic acid increases as the potential approaches the thermodynamic limit ($\eta = 0$ V), but with an efficiency that falls well below that of the analogous metal-free **MWCNT@CeO₂**. This behavior is explicable with a greater tendency of the hydrides formed on Pd (Pd-H) to evolve to $H_2$ instead of promoting the electro-hydrogenation of $CO_2$ to formate. This observation contrasts with what reported by Kanan and coworkers,[14] but it is likely that on Pd nanoparticles the acidic media may enhance more strongly the rate of HER than that of $CO_2$ hydrogenation. In acidic solution, Pd-H are then more keen to generate $H_2$ following a Volmer-Heyrovsky or Volmer-Tafel mechanism (120 mV/dec slope, Fig.

**2.12.b**), whereas the formation of hydrides on $CeO_2$ is less efficient and does not led to an efficient production of formic acid.
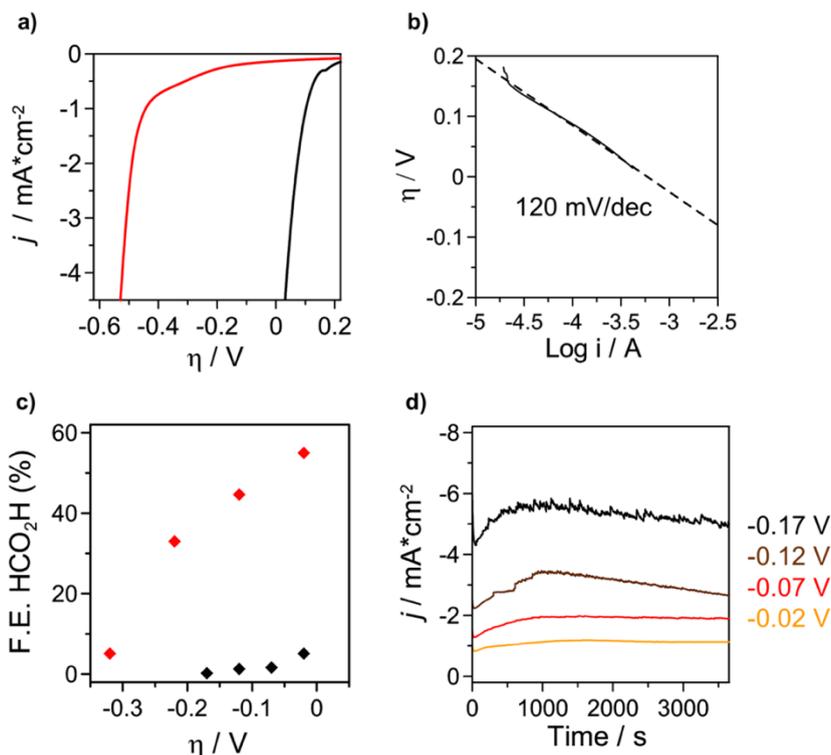


**Figure 2.12:** Electrochemical characterization of **MWCNT@Pd/CeO₂**. **a)** LSV for the nanostructured catalysts **MWCNT@Pd/CeO₂** (black line) and **MWCNT@CeO₂** (red line) in a $CO_2$-saturated solution. Scan rate 2 mV/s. Potential are reported vs. E' [$CO_2$/$HCO_2H$] = -0.2 $V_{RHE}$. Note that the cathodic current of the black curve is positive to 0 V vs. E' [$CO_2$/HCOOH] because of HER current. **b)** Tafel plot for **MWCNT@Pd/CeO₂** derived from LSV experiments. **c)** Comparison between the F.E. of formic acid production for **MWCNT@Pd/CeO₂** (black) and **MWCNT@CeO₂** (red diamonds) in a $CO_2$-saturated $HNO_3$ solution. **d)** Potentiostatic 1-hour electrolysis at overpotentials of -0.02 V, -0.07 V, -0.12 V and -0.17 V vs. E' [$CO_2$/$HCO_2H$] (from bottom to top). Electrolyte: $HNO_3$ 0.1 M solution.

To definitively prove the role of the different hydride species on Pd and $CeO_2$, experiments with **MWCNT@Pd/CeO₂** in neutral bicarbonate buffer were performed.

## 2.3.2 Electrochemical characterization in Bicarbonate buffer

An exhaustive electrochemical characterization of **MWCNT@Pd/CeO₂** and its comparison with **MWCNT@CeO₂** is reported in Fig. **2.13**. It is remarkable how similarly the two nanocomposites behave in near neutral bicarbonate buffer (Fig.

**2.13a**), while in acidic solutions their respective *j*-V curves are displaced by about 600 mV. In KHCO$_3$ 0.5 M, both the nanocomposites struggle to reach high cathodic currents (irrespective if they are related to HER or CO$_2$ reduction) even if large overpotentials are applied. This behavior is translated in a similar trend and comparable F.E. for formic acid production as measured by I.C. (Fig. **2.13b**) and also similar F.E. for H$_2$ evolution (not shown). In bicarbonate buffer and especially at low overpotential, **MWCNT@Pd/CeO$_2$** is more efficient than **MWCNT@CeO$_2$** for formate production. The difference even if not substantial can be ascribed to the extent of hydride species on the two samples. At near neutral pH it is likely that hydrides formation on the Pd NPs of **MWCNT@Pd/CeO$_2$** is more efficient than on CeO$_2$. If hydrides are involved in CO$_2$ electro-hydrogenation, this finding would provide an additional proof of their participation in the mechanism, and would explain the higher, but however low, F.E. for formate production observed in the case of **MWCNT@Pd/CeO$_2$**.
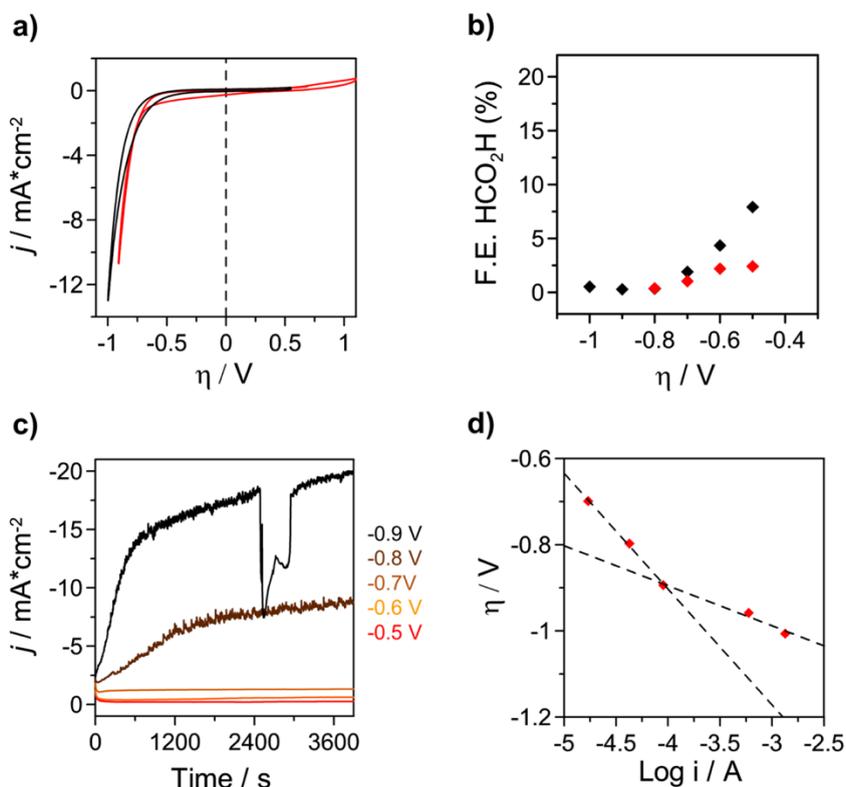


**Figure 2.13**: **a)** CVs at 50 mV/s for **MWCNT@Pd/CeO$_2$** (red) and **MWCNT@CeO$_2$** (black line) in KHCO$_3$ 0.5 M. **b)** Comparison between the F.E. for formic acid production of **MWCNT@Pd/CeO$_2$** (black) and

**MWCNT@CeO$_2$** (red diamonds) in a $CO_2$-saturated KHO$_3$ 0.5 M solution. **c)** Potentiostatic 1-hour electrolysis at various overpotentials vs. E' [$CO_2$/HCOOH] (from bottom to top). The decrease of the current for the more negative potentials around 2400 s is due to the formation of bubbles that stick at the surface and reduce the effective surface area of the electrode. It is worth mentioning that this however does not affect the F.E. calculations since the charge is integrated over the entire length of the electrolysis. **d)** Tafel plot obtained from potentiostatic experiments.

From these results it is then possible to correlate the availability of free protons in solution to the likeliness of hydride formation both on CeO$_2$ and Pd nanoparticles. Since in the case of **MWCNT@Pd/CeO$_2$** the nanocomposite displays identical efficiencies for formate production in acid and in bicarbonate buffer (although, for the latter, shifted to more negative potentials) we may infer that Pd-hydrides play a minor role in promoting CO$_2$ electro-hydrogenation with respect to hydrides formed on CeO$_2$. In the latter case very different efficiencies at acidic or neutral pH were observed. In bicarbonate buffer the F.E. for HER is pretty much the same for **MWCNT@CeO$_2$** and **MWCNT@Pd/CeO$_2$**: the process however occurs for both systems at moderate-high overpotential, Pd-H led to HER similarly to **MWCNT@CeO$_2$**, meaning that possibly at neutral pH also the formation of Pd-H is hindered by the solution pH. The latter observation is somehow in contrast to what reported by Kanan in his work with Pd/C NPs, where in the same experimental conditions (KHCO$_3$ 0.5 M) they reported current densities that are more than twice of those reported here. Also, the authors detected formic acid at very low overpotentials, in a potential region where no faradaic currents are here observed. This difference may arise from the large amount of Pd present in their work (10% wt.) and probably to a better dispersion of their nanoparticles on Pd/C. The Tafel plot of Fig. **2.13d** reveals the existence of two regions of different kinetics, similarly to what observed in acidic solutions, with the differences in Tafel slope are not paralleled by differences in F.E. for formate production (that is rather low in both potential regions).

From the results here reported it seems that at neutral pH the low availability of free protons not only hinders the formation of Pd-H, but also that of hydrides on CeO$_2$. The net effect is a drastic reduction of F.E. for formate and a preferential HER due to the very negative overpotential required. In KHCO$_3$ the slightly higher F.E. for formate of **MWCNT@Pd/CeO$_2$** may arise from a more favorable formation of Pd-H than other types of hydrides on CeO$_2$. By contrast, the high availability of protons in acidic solution makes the formation of hydrides much easier, and these

species on the surface of cerium oxide turn to be very reactive towards $CO_2$ hydrogenation.

## 2.4 Conclusions & Outlooks

The pretty high selectivity for formic acid production is a remarkable result for the nanocomposite **MWCNT@CeO₂**, a noble metal-free electrocatalyst. This peculiar activity arises form the combination of multiple factors and ultimately by the synergic combination of the different building blocks.  MWCNTs are proved to be fundamental to provide an optimal electronic connection within the nanostructure, whereas the oxide shell actively mediates $CO_2$ conversion, thus being much more than a mere –though rather effective- platform for $CO_2$ adsorption. After comparison of the electrochemical activity of **MWCNT@CeO₂** with that of **MWCNT@Pd/CeO₂** at various pHs, the strikingly high efficiency for formate/formic acid production has been ascribed to the formation of very reactive hydrides species on the surface of cerium dioxide. These hydrides on $CeO_2$, as well as those on Pd (Pd-H), would form preferentially in acid, but only in the former material this translates in an efficient formic acid production. In the presence of Pd NPs the preferential HER is observed. In general, the formation of Pd-H does not lead to improved conversion efficiency, but the investigation of such system allowed to better understand the role of different hydrides and decouple them from the overall catalytic activity.
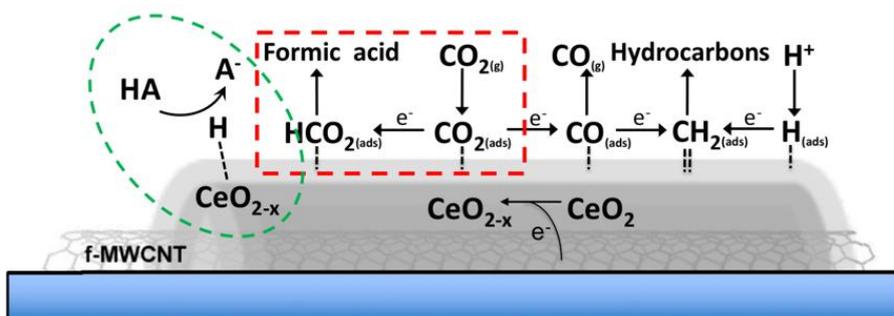


**Figure 2.14:** schematic representation of $CO_2$ reduction on **MWCNT@CeO₂** with highlighted the path to formic acid production favored by partially reduced $CeO_{2-x}$ that enables hydrides formation.

Fig. **2.14** summarizes the possible reaction mechanism derived from the experimental results. $CO_2$ adsorption occurs preferentially after reduction of $CeO_2$

to its sub-stoichiometric form $CeO_{2-x}$. In the reducing environment of cathodic polarization very reactive hydride species are generated on the surface of $CeO_2$ from the reduction of a proton source (HA) in solution. The combination of these two process leads to the preferential formation of formate/formic acid following an electro-hydrogenation mechanism thus bypassing the highly endoergonic direct outer-sphere reduction of $CO_2$. The overall process is particularly selective since adsorbed CO, a precursor for the formation of more reduced hydrocarbons like methane, is not formed.

The possibility to convert $CO_2$ by the co-participation of electrochemically generated hydride species on oxides may provide very interesting implications for the future development of $CO_2$ reduction electrocatalysts. Following this proof of principle, it is envisaged that other oxide materials able to form hydrides can be used. $WO_3$, for example, can be a potential candidate, also suitable for a photo-electrochemical approach. Indeed, the bands of $WO_3$ met the energy requirements needed to reduce $CO_2$ and photo-excited electrons can potentially be transferred from the CB of $WO_3$ to $CO_2$ via the participation of surface hydride species.[40]

Also the very tunable family of perovskites can have a role in this context. Moreover, the combination of oxides with cheap and earth-abundant metals like Cu, Fe, Sn is also foreseen to boost the future of $CO_2$ electrocatalysis and their study will be for sure of great interest. For example, in the specific case of $CeO_2$ it has been recently reported how a Cu-doping of the ceria lattice increases $CO_2$ adsorption on the surface, especially at low dopant contents.[41] These findings and the excellent properties of copper as $CO_2RR$ electrocatalyst, together with the results here reported may suggest intriguing characteristic for a potential MWCNT@Cu/$CeO_2$ electrocatalyst.

# 2.5 Bibliography

1. M. Gattrell, N. Gupta, A. Co, A review of the aqueous electrochemical reduction of $CO_2$ to hydrocarbons at copper. *J. Electroanal. Chem.*, **594**, 1–19 (2006).
2. C. M. Sánchez-Sánchez, V. Montiel, D. A. Tryk, A. Aldaz, A. Fujishima, Electrochemical approaches to alleviation of the problem of carbon dioxide accumulation, *Pure Appl. Chem.,* **73**, 1917–1927 (2001).
3. K. P. Kuhl, E. R. Cave, D. N. Abram, T. F. Jaramillo, New insights into the electrochemical reduction of carbon dioxide on metallic copper surfaces, *Energy Environ. Sci.*, **5**, 7050-7059 (2012).
4. C. Rice, S. Ha, R. I. Masel, P. Waszczuk, A. Wieckowski, T. Barnard, Direct formic acid fuel cells, *J. Power Sources*, **111**, 83-89 (2002).
5. S. N. Bizzari, M. Blagoev (June 2010). "CEH Marketing Research Report: FORMIC ACID". *Chemical Economics Handbook*. SRI consulting.
6. S. Moret, P. J. Dyson, G. Laurenczy, Direct synthesis of formic acid from carbon dioxide by hydrogenation in acidic media, *Nat. Comm.*, **5**, 4017 (2014).
7. M. Aresta, A. Dibenedetto, Utilisation of $CO_2$ as a chemical feedstock: opportunities and challenges, *Dalton Trans.*, 2975–2992 (2007).
8. P. G. Jessop, F. Joo, C. C. Tai, Recent advances in the homogeneous hydrogenation of carbon dioxide, *Coord. Chem. Rev.*, **248**, 2425–2442 (2004).
9. P. G. Jessop, T. Ikariya, R. Noyori, Homogeneous catalytic hydrogenation of supercritical carbon dioxide, *Nature*, **368**, 231–233 (1994).
10. S. Ogo, H. Hayashi, S. Fukuzumi, Aqueous hydrogenation of carbon dioxide catalysed by water-soluble ruthenium aqua complexes under acidic conditions, *Chem. Commun.*, **23**, 2714–2715 (2004).
11. S. Kapusta, N. Hackerman, The Electroreduction of Carbon Dioxide and Formic Acid on Tin and Indium Electrodes, *J. Electrochem. Soc.*, **130**, 607-613 (1983).
12. M. Todoroki, K. Hara, A. Kudo, T. Sakata, Electrochemical reduction of high pressure $CO_2$ at Pb, Hg and In electrodes in an aqueous $KHCO_3$ solution, *J. Electroanal. Chem.* **394**, 199 (1995)
13. M. N. Mahmood, D. Masheder, C. J. Harty. Use of gas-diffusion electrodes for high-rate electrochemical reduction of carbon dioxide. I. Reduction at lead, indium- and tin-impregnated electrodes, *J. Appl. Electrochem*. **17**, 1223 (1987).
14. X. Min, M. W. Kanan, Pd-Catalyzed Electrohydrogenation of Carbon Dioxide to Formate: High Mass Activity at Low Overpotential and Identification of the Deactivation Pathway, *J. Am. Chem. Soc*., **137**, 4701–4708 (2015).
15. M. Azuma, K. Hashimoto, M. Hiramoto, M. Watanabe, T. Sakata, Electrochemical Reduction of Carbon Dioxide on Various Metal Electrodes in Low-Temperature Aqueous $KHCO_3$ Media, *J. Electrochem. Soc.*, **137**, 1772–1778 (1990).

16. H. Noda, S. Ikeda, Y. Oda, K. Imai, M. Maeda, K. Ito, Electrochemical Reduction of Carbon Dioxide at Various Metal Electrodes in Aqueous Potassium Hydrogen Carbonate Solution, *Bull. Chem. Soc. Jpn.*, **63**, 2459–2462 (1990).

17. K. Ohkawa, K. Hashimoto, A. Fujishima, Y. Noguchi, S. Nakayama, Electrochemical reduction of carbon dioxide on hydrogen storing materials: Part 1. The effect of hydrogen absorption on the electrochemical behavior on palladium electrodes, *J. Electroanal. Chem*. **345**, 445–456 (1993).

18. Y. Hori, H. Wakebe, T. Tsukamoto, O. Koga, *Electrochim. Acta*, **39**, 1833–1839 (1994).

19. R. Kortlever, K. H. Tan, Y. Kwon, M. T. M. Koper, Electrochemical carbon dioxide and bicarbonate reduction on copper in weakly alkaline media, *J. Solid State Electrochem.,* **17**, 1843-1849 (2013).

20. K. J. P. Schouten, Y. Kwon, C. J. M. van der Ham, Z. Qin, M. T. M. Koper, A new mechanism for the selectivity to $C_1$ and $C_2$ species in the electrochemical reduction of carbon dioxide on copper electrodes, *Chem. Sci.,* **2**, 1902–1909 (2011).

21. Hori Y (2008) In: Vayenas CG, White RE, Gamboa-Aldeco ME (eds.) Modern Aspects of Electrochemistry. Springer, New York

22. M. Cargnello, M. Grzelczak, B. Rodrı́guez-Gonzaĺez, Z. Syrgiannis, K. Bakhmutsky, V. LaParola, L. M. Liz-Marzań, R. J. Gorte, M. Prato, P. Fornasiero, Multiwalled Carbon Nanotubes Drive the Activity of Metal@oxide Core−Shell Catalysts in Modular Nanocomposites, *J. Am. Chem. Soc.*, **134**, 11760-11766 (2012).

23. Z. Cheng, B. J. Sherman, C. S. Lo, Carbon dioxide activation and dissociation on ceria (110): A density functional theory study, *J. Chem. Phys.*, **138**, 014702 (2013).

24. P. M. Albrecht, D. Jiang, D. R. Mullins, $CO_2$ Adsorption As a Flat-Lying, Tridentate Carbonate on $CeO_2(100)$, *J. Phys. Chem. C*, **118**, 9042–9050 (2014).

25. F. D. Manchester, J. M. Pitre, The Ce-H (Cerium-Hydrogen) System, *J. Phase Equilib.,* **18**, 63-77 (1997).

26. P. Serp, J. L. Figueiredo, *Carbon materials for catalysis* (J. Wiley and sons, Hoboken, 2009)

27. L. Eyring. *The binary lanthanide oxides: synthesis and identification*. 201 (Kluwer, 1991).

28. W. C. Chueh, Electrochemical and thermochemical behavior of $CeO_{2-\delta}$, *PhD thesis*, CalTech (2011).

29. J. J. Delgado, E. d. Río, X. Chen, G. Blanco, J. M. Pintado, S. Bernal, J. J. Calvino, in *Catalysis by Ceria and Related Materials*, Ch. 2 47–138 (Imperial College press, London, 2013)

30. A. Trovarelli, P. Fornasiero (eds.), *Catalysis by Ceria and Related Materials*, (Imperial College press, London, 2013)

31. A. Trovarelli, Catalytic properties of ceria and $CeO_2$-containing materials, *Cat. Rev. - Sci.  Eng.,* **38**, 439-520 (1996).
32. W. C. Chueh, C. Falter, M. Abbott, D. Scipio, P. Furler, S. M. Haile, A. Steinfeld, High-Flux Solar-Driven Thermochemical Dissociation of $CO_2$ and $H_2O$ Using Nonstoichiometric Ceria, *Science,* **330**, 1797-1801 (2010).
33. D. R. Mullins, The surface chemistry of cerium oxide, *Surf. Sci. Rep.,* **70**, 42-85 (2015).
34. C. Y. Cummings, S. J. Stott, M. J. Bonné, K. J. Edler, P. M. King, R. J. Mortimer, F. Marken, Underpotential surface reduction of mesoporous $CeO_2$ nanoparticle films, *J Solid State Electrochem*, **12**, 1541–1548 (2008).
35. R. K. Nagarale, U. Hoss, A. Heller, Mixed-Valence Metal Oxide Nanoparticles as Electrochemical Half-Cells: Substituting the Ag/AgCl of Reference Electrodes by $CeO_{2-x}$ Nanoparticles, *J. Am. Chem. Soc.*, **134**, 20783-20787 (2012).
36. A. J. Bard, L. R. Faulkner, *Electrochemical Methods: Fundamentals and Applications*, (Wiley, New York, ed. 2 ,2001).
37. A. Bassegoda, C. Madden, D. W. Wakerley, E. Reisner, J. Hirst, Reversible Interconversion of $CO_2$ and Formate by a Molybdenum- Containing Formate Dehydrogenase, *J. Am. Chem. Soc.,* **136**, 15473–15476 (2014).
38. A. Kapałka, G. Fòti, C. Comninellis, Determination of the Tafel slope for oxygen evolution on boron-doped diamond electrodes, *Electrochem. Commun.,* **10**, 607-610 (2008).
39. Z. A. Feng, M. L. Machala, W. C. Chueh, Surface electrochemistry of $CO_2$ reduction and CO oxidation on Sm-doped $CeO_{2-x}$: coupling between $Ce^{3+}$ and carbonate adsorbates, *Phys. Chem. Chem. Phys.,* **17**, 12273-12281 (2015).
40. R. Griessen, N. Strohfeldt, H. Giessen, Thermodynamics of the hybrid interaction of hydrogen with palladium nanoparticles, *Nat. Mater.*, 1-7 (2015). refsuPd che adsorbe protoni
41. M. Li, U. Tumuluri, Z. Wu, S. Dai, Effect of Dopants on the Adsorption of Carbon Dioxide on Ceria Surfaces. *ChemSusChem,* **8**, 3651-3660 (2015).

# PHOTO-ELECTROCHEMICAL HYDROGEN EVOLUTION

# CHAPTER 3

# Photo-Electrochemical Hydrogen Evolution

The work presented in this Chapter has been conducted during a six-month research stay in the Electrochemical Energy Laboratory (EEL) at M.I.T. In that period, the original aim of the PhD project of studying electrocatalytic systems for energy conversion, has been expanded and integrated with a photo-electrochemical approach, in which the classical know-how of electrochemistry is combined to that of semiconductor physics and material science.

The project outlined in the following section results from a collaboration between EEL and the Departments of Physics and Mechanical Engineering at the University of Yale, where the studied materials have been synthesized. It is here reported the complete electrochemical characterization performed on the photoelectrode assemblies during my visit, as well as other materials' characterization. For a better understanding of the project and to appreciate the peculiarity of the studied systems, also experiments done by collaborators are also presented (specified in the text).

## 3.0. Photo-electrochemical Hydrogen Evolution (PEC HER)

One of the big challenges for a sustainable society is to develop methods able to capitalize the potentiality of solar energy, the most extensive, cheap and powerful source of energy available on Earth. This milestone can be partially achieved from the conversion of solar energy into chemical fuels, that entangles also the potentiality to decouple the processes of energy capture and reconversion.

Solar fuel production, such as by photo-electrochemical (PEC) water splitting[1-3] or $CO_2$ reduction[4,5] allows the storage of solar energy in the form of chemical bonds, easily reconverted to electricity, heat, chemicals or other forms of energy on demand. Practical materials and devices able to produce chemical fuels when exposed to sunlight have to be designed, keeping in mind that the prominence of the problem emphasize the requirement for low-cost and abundant materials.

Realization of this concept requires the integration in a single device of diverse functional elements that must work together efficiently to transform in the order

*i*) light into charge (photons absorption and charge separation), and *ii*) charge into fuels through electron transfer reactions at the surface. This can be achieved by means of several possible configurations (highlighted in Fig. **I.5**, but many others are also possible), that share a common point, that is the use of semiconducting materials as photoelectrodes. Due to their band structure, semiconductors can efficiently separate photogenerated charge carriers and are excellent candidate to carry out the task of light absorption in practical devices.

More specifically, the most efficient collectors of solar energy are III-V semiconductor solar cells in light of their direct band gap (electrons in the valence and conduction bands share the same crystal momentum).[6] Such high efficiency of light absorption allows to use very thin active layers, with the possibility to make thin-films devices (< 1 μm thick).[7-9] By contrast, indirect band gap semiconductors, like Si, absorb light less efficiently and require much thicker active layers. Despite these drawbacks, Si is the most used material in PV for its huge abundance and low costs.

### 3.0.1 Protection of solar cells

III-V semiconductors (and also Si), however, are not stable under illumination in the relevant operative conditions of PEC water splitting (i.e. aqueous electrolytes).[10,11] They thus need need to be protected from the solution, but in a way that sunlight absorption is still efficient and that photogenerated carriers are able to react at the surface giving the desired products. Transition metal oxides represent a flexible class of materials with the right requirements to be good candidates as protective layers for III-V semiconductors.[12,13] They are stable in aqueous solutions and the possibility to easily tune their properties give rise to their peculiar activity for promoting water splitting kinetics, including HER and OER.[14] Moreover, since they do not perform well as solar energy collectors they are perfectly complementary to III-V semiconductors.

Among the various approaches to PEC water splitting,[15] the strategy to "bury" a solar cell under a protective layer is getting more and more credit in the scientific community as a valuable way to leverage the impact of this technology on the global scale. This strategy is particularly interesting for the possibility to use very well-known and efficient PVs like Si, GaAs and perovskites. Some of these semiconductors have been studied for decades, and the huge background in

material fabrication and development can in principle allow for this technology to see the light of tomorrow in a relative short time. Other PEC approaches, like those reported in Fig. **I.5b**, have actually the limitation of a poor material stability for long-term operation, but several very promising candidates have been proposed and are being under development both as photoanodes (like $BiVO_4$) or photocathodes ($Cu_2O$, $WSe_2$, InP).[16]

Recent advances in efficiency for photo-electrochemical hydrogen[17] and oxygen evolution[18-21] include the incorporation of III-V (like GaAs) or Si solar cells[22,23] with surface protecting oxides[17-24] or sulfides[25-27]. The concept of this approach is to couple the high efficiency for solar conversion of solar cells with the high stability of surface protective layers in the relevant chemistries of PEC water splitting. $TiO_2$ has received wide attention as a coating layer on different solar cells (Si, perovskites) and for both PEC HER and PEC OER. The results of this approach are very remarkable[27,28] and conversion efficiencies up to 12.3% for unbiased overall water splitting have been reported.[29] Key point is to create a stable surface coating that allows electrons to flow by tunneling or by a metal-like ohmic contact as demonstrated in some cases for thicker (~100nm) layers.[24,30]

These protection schemes however often require precious metal catalysts such as Pt[17,24,31,32] to promote reaction kinetics, reducing the kinetic overpotentials for the oxidation or reduction reactions.

An incomplete control of the interfaces between the catalysts, surface protection layers, and the underlying semiconductor has in some cases limited the ability to achieve further advances.[33]

### 3.0.2. A novel concept

With this respect, a key point of the work here presented is the possibility to eliminate the presence of surface catalysts by a proper combination and engineering of the solar cell-metal oxide protective layer. In particular, it is shown how a detailed determination of the band energy diagram (bands position in the absolute energy scale) for the studied photocathode is a powerful guideline to design and predict effective photoelectrodes, without the need for catalysts on the surface. Moreover, the current density usually involved in PEC water splitting are about two order of magnitude smaller than those of commercial electrolyzers. This

fact greatly reduces the requirements for very high catalytic activity and further motivates the possibility to circumvent the use of catalysts.

Of course this strategy cannot be adopted to any solar-fuel production scheme, as there are reactions with slow kinetics that strongly require surface catalysis (e.g. OER), but in some cases this approach can be extremely helpful to simplify the device architecture while keeping high the efficiency of the conversion process. This is the case for example of hydrogen evolution, a relatively simple reaction with fast kinetics.

In this Chapter it is shown how photo-electrochemical HER can proceed on a catalyst-free metal oxide-protected III-V semiconductor (an np-GaAs solar cell) at neutral pH. The np-GaAs has been protected with a nanometric-thick layer of $SrTiO_3$, a wide band gap transition metal oxide with perovskite structure. This oxide is very stable in water and has been epitaxially grown on top of GaAs, so as to reduce as much as possible any losses (charge carrier recombination, slow electron transport, etc.) at the interface with the solar cell.

## 3.1 STO-GaAs photocathode assembly for PEC hydrogen evolution

The concept of protecting III-V solar cells by transition metal oxides is realized in this work burying the np-GaAs junction under a 16 nm thick epitaxial $SrTiO_3$ layer. These photocathode assemblies, labelled as **STO-GaAs** and highlighted in Fig. **3.1**, have been synthesized in the Department of Physics at the University of Yale, where also the solid state characterization of the devices has been performed.

The 16 nm thick protective oxide has been epitaxially grown on np-GaAs by MBE. $SrTiO_3$ faces the solution side, while the protected GaAs is isolated from the electrolyte and back-contacted to the external electrical circuit. The peculiar characteristics of the GaAs solar cell, as well as those of the $SrTiO_3$ protective layer are reported in detailed in the following sections.

The motivation for the choice of $SrTiO_3$ and GaAs is multiple, and mainly deals with consideration based on the energetics of the semiconductors' bands and their relative alignment. In Fig. **3.1a** the various elements of the device, together with the relevant [$H^+/H_2$] redox couple at pH = 7 are shown and aligned with respect to the absolute energy scale. The diagram refers to energetics calculated with the components not in contact one to the other, so it is not representative of a real situation, but clearly evidences the favorable downhill pathway for electron flow

from the top of the conduction band of GaAs down to the solution. When **STO-GaAs** photocathode is realized and placed in solution, the electrical contact of the different elements induces adjustments of the bands' position so that the solution and the electrode experience the same Fermi energy when the system is equilibrated in the dark. However, these adjustments do not involve changes of the band edge positions, that are determined by the chemical properties of the different interfaces, and then are fundamental to describe the properties of the entire photoelectrode. These interfaces are those between electrolyte-SrTiO$_3$ and SrTiO$_3$-GaAs and are highlighted by the black circles of Figure **3.1b**. In this work they have been determined experimentally by means of EIS and XPS to gather a quantitative description of **STO-GaAs** energetics and to have an in-depth analysis of PEC performances. As it will be shown, the possibility to run HER without the addition of any catalyst on the surface relies mainly on the energy offset between the [H$^+$/H$_2$] level and the SrTiO$_3$ conduction band.
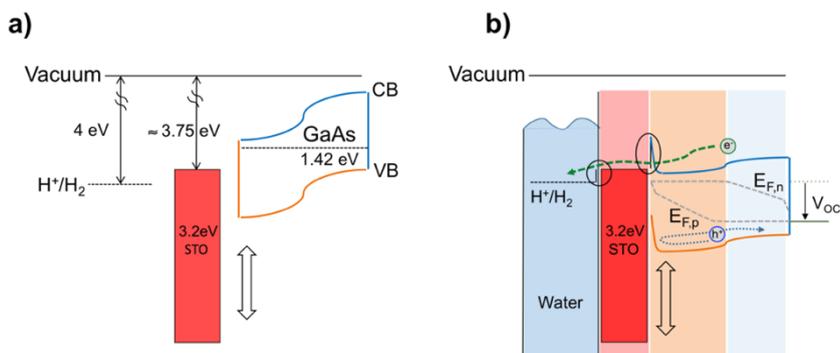


**Figure 3.1: a)** schematic energy diagram of SrTiO$_3$ and GaAs in vacuum and not contacted one to the other. The energies of the bands are drawn in the absolute energy scale, with Electron Affinity and Band-gap (E$_g$) values taken from tabulated values. The black arrow highlights the high energy barrier between SrTiO$_3$ and GaAs that does not allow photogenerated holes to reach the surface. Not in scale.
**b)** Preliminary representation of **STO-GaAs** operation under 1 sun illumination. The SrTiO$_3$ layer (red shaded area) protect the underlying np-GaAs solar cell (orange and blue areas) from photocorrosion in aqueous electrolytes (drawn at left together with the energy of the relevant [H$^+$/H$_2$] redox couple). When sunlight is absorbed by the GaAs solar cell, electrons are excited in the CB and can flow downhill towards the surface where they react and reduce water to hydrogen. Holes are not allowed to reach the surface for the high energy barrier present. The photovoltage generated by the np-junction is described as the difference of the quasi Fermi energy level for electrons (E$_{F,n}$) and holes (E$_{F,p}$), that respectively describe the population of majority and minority carriers. With black circles are also highlighted the fundamental energy gaps at the interfaces electrolyte-SrTiO$_3$ and SrTiO$_3$-GaAs, that have been experimentally evaluated (see text). CB and VB denote the conduction and valence bands, respectively. Lengths are not in scale, while band energies are.

**STO-GaAs** operation under 1 sun illumination is highlighted in Fig. **3.1b**. Absorption of sunlight by the GaAs solar cell generates a photovoltage and the resulting electric field at the np-junctions induces the separation of the photogenerated carriers. Electrons move towards the oxide-water interface where they have enough free energy to evolve hydrogen, while photogenerated holes move in the opposite direction and are collected at the back contact. In addition to the electric field effect, the high energy barrier at the $SrTiO_3$-GaAs interface prevents holes to reach the surface, inducing possible recombination losses.

To understand the electronic structure and the properties of the oxide-electrolyte interface, also Nb-doped $SrTiO_3$ single crystal electrodes (**Nb:STO**) have been studied. The Nb doping (1% at.) is needed to make the electrodes electronically conductive, and since it does not induce considerable changes in the optical gap with respect to un-doped $SrTiO_3$,[34] **Nb:STO** is a good approximation of the epitaxial $SrTiO_3$ protective layer.

Measurements of the model system **Nb:STO** are required to figure out some peculiar features of the oxide protective layer. For example, the valence band energy of $SrTiO_3$ are revealed by Mott-Schottky analysis (section **3.3.4**). As in the case of **MWCNT@PdTiO₂**, measurements of the space charge capacitance as a function of $E_{app}$ have been used to evaluate the valence band position. As mentioned, the offset between the $SrTiO_3$ valence band and the hydrogen couple ($H^+/H_2$) in the actual experimental conditions is a fundamental point to understand the PEC performances of **STO-GaAs** and to rationalize a quantitative band diagram for the photocathode.

### 3.1.1. III-V semiconductor solar cell.

As mentioned earlier in section **3.0**, III-V semiconductors are up to now the most efficient materials for solar cells, with efficiencies as high as 28.8%. However, performances for state-of-the art crystalline silicon are not very different, with a record efficiency of 25.6%.[6] GaAs has a bandgap of 1.42 eV that is an optimal value to exploit at best the incoming sunlight. The visible part of the solar spectrum is effectively absorbed and GaAs solar cells reach conversion efficiency close to the Shockley-Quessier limit of 31%.[35] As it will be explained in section **3.2.3**, a bandgap of 1.42 eV would allow to reach a maximum current density of ~32 mA/cm$^2$, a value

well above the conventional threshold current of 10 mA/cm$^2$ that roughly correspond to a 10% solar-to-hydrogen efficiency.[36]

In this work, GaAs solar cells have been produced on a lab scale by solid source molecular beam epitaxy (MBE) on on-axis 10 cm square (001) p-GaAs wafers ($\sim$10$^{19}$ cm$^{-3}$). By electron diffraction is revealed the growth of a smooth crystalline (001) surface. In order to generate the np-junction, *n*- and *p*-type dopants (Si and Be respectively) have been added. In Fig. **3.2a** is reported a schematic section of the GaAs solar cell with highlighted the dopant densities of each layer. Role of the buffer layers is to prevent current losses for charge recombination in the bulk of the solar cell.

Classical current–voltage (J–V) characteristic of a representative np-GaAs solar cell is shown in Fig. **3.2b** under simulated AM1.5g solar irradiation. The solar cell shows an open circuit voltage ($V_{OC}$) of 0.94 V (that corresponds to the generated photovoltage) and a short circuit current ($J_{SC}$) of 14.3 mA/cm$^2$. These values yield a solar-to-electricity efficiency of 10.2%.

The theoretical voltage required to split water (without applying any external bias) is 1.23 V (at 20°C), but because of kinetic overpotentials this value practically raises in the order of 1.8-2 V. This fact means that any solar cell is not able to generate enough driving force to split water by itself. More than a single cell, in a tandem (2x) or multi-junction (3x, 4x) configuration are then needed to reach the required voltage. The high $V_{OC}$ registered for np-GaAs, underlines the possibility to achieve unassisted water splitting with just a combination of 2x np-GaAs solar cells in a tandem configuration.

a)

| Cap | As$_2$ | | $\sim$60 nm |
|---|---|---|---|
| Emitter | n-GaAs | 1x10$^{18}$ cm$^{-3}$ | 100 nm |
| Base | p-GaAs | 1x10$^{17}$ cm$^{-3}$ | 2 µm |
| Buffer | p-GaAs | 5x10$^{18}$ cm$^{-3}$ | 20 nm |
| Reflector | p-Al$_{0.4}$Ga$_{0.6}$As | 3x10$^{18}$ cm$^{-3}$ | 50 nm |
| Buffer | p-GaAs | 5x10$^{18}$ cm$^{-3}$ | 250 nm |
| Substrate | p-GaAs | 1x10$^{19}$ cm$^{-3}$ | 600 µm |

b)

$J_{SC}$ = 14.3 mA/cm$^2$
$V_{OC}$ = 0.94 V
$\eta$ = 10.2%
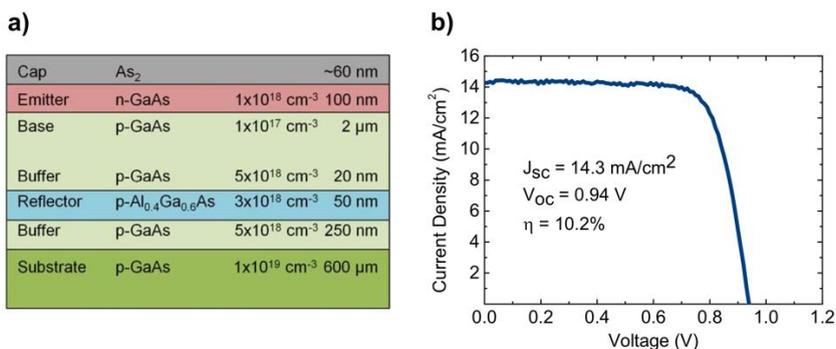
**Figure 3.2: a)** schematic section of the np- GaAs solar cell, with specified the different layers. Not in scale. **b)** Current-voltage (J-V) characteristic of the np-GaAs solar cell under AM1.5g illumination. Courtesy of Dr. Lior Kornblum, University of Yale.

To clarify the role of the np-junction, the operation of the np-GaAs solar cell when used directly as a photocathode is schematized by the band diagrams of Fig. **3.3**.
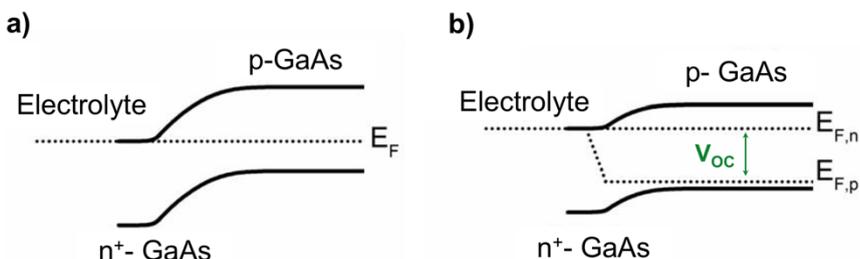


**Figure 3.3:** Band diagrams showing the operation of the np junction solar cell under open-circuit conditions **a)** in the dark and **b)** under illumination. Courtesy of Dr. David Fenning, MIT.

An electrolyte with a redox level matching the electron affinity of GaAs is chosen for simplicity. In the dark (Fig. **3.3a**), the junction is equilibrated and a built-in potential (and an electric field) are formed across the depletion region, caused by the diffusion of carriers from both sides of the junction.[37] Under illumination (Fig. **3.3b**), photogenerated electrons and holes in and near the depletion region are separated by the built-in field and are the source of the photocurrent.[32] The populations of these excess carriers are represented by the quasi-Fermi energy levels for electrons ($E_{F,n}$) and holes ($E_{F,p}$), and their difference correspond to the generated photovoltage, $V_{OC}$.

### 3.1.2. Transition metal oxide protective layer.

Many materials have been studied as protective layer for solar cells, but issues of poor quality of the junctions has often limited their applications. A protective layer having a high-quality interface with the underlying solar cell is therefore necessary to maximize the efficiency of the photoelectrode assembly. $SrTiO_3$ is a wide band gap semiconductor (3.2 eV) with perovskite structure $ABO_3$ and can be grown epitaxially with minimal interfacial reactions.[38-41] Among oxide materials, is one of the few that is possible to epitaxially grow. These characteristic, together with the great stability at different pH[ref??] and at extreme temperatures and pressures, makes it an ideal candidate for the purpose to protect GaAs.

In this work a thin $SrTiO_3$ metal oxide layer is grown epitaxially by MBE[42,43] on the GaAs solar cell structure previously described. The resulting oxide coating is 16 nm-thick and by X-ray diffraction (not shown) it is demonstrated the high crystalline

quality. TEM image of Fig. **3.4** reveals an atomically sharp interface between $SrTiO_3$ and the underlying GaAs solar cell, necessary to achieve good photo-electrochemical properties.
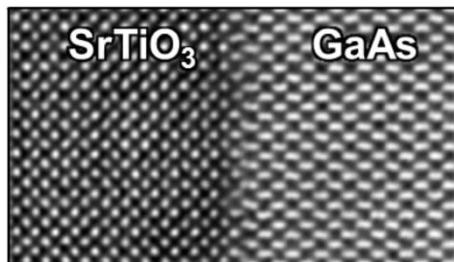


**Figure 3.4:** Atomic structure of the $SrTiO_3$/n-GaAs interface revealed using transmission electron microscopy (2 nm scale bar). White dots in the $SrTiO_3$ side are Sr atoms. Courtesy of Y. Zhou, Brookhaven National Laboratory.

## 3.2. Characterization of PEC devices.

To assess the solar-to-fuel energy conversion process of a PEC device, different performance metrics are used. This has sometimes generated ambiguity in data presentation, and for this reason over the years some formalizations have been proposed.[44] It is then convenient to briefly introduce some of the figure of merit usually considered in evaluating PEC devices and several standardized procedures adopted for materials' testing and characterization.

### 3.2.1. AM 1.5g solar spectrum

Standardization measurements in the field of PEC stems from that of photovoltaics, and both share several methodologies and test facilities. The first aspect to consider is the light source. In a collaborative effort, the PV industry, government laboratories and the American Society for Testing and Materials (ASTM) years ago defined the standard terrestrial solar spectrum, the Air Mass 1.5 Global, also known as AM1.5g.[45]

By then solar cells have been characterized with this simulated sunlight, whose light intensity is commonly defined as "1 sun" and correspond to 100 mW/cm². In this work 1 sun illumination is realized using a 300 W Xe arc lamp as the light source, and a Schott glass AM1.5g filter to reproduce the simulated sola spectrum. The intensity of the light in front of the working electrode is calibrated before each measurement with a standard c-Si PV reference cell.

### 3.2.2. Photocurrent – potential

The most common, easy and powerful tool to analyze the behavior of a photoelectrode is to record the generated photocurrent as a function of the applied potential in a three-electrode electrochemical cell. Once each photoelectrode is optimized, two-electrode measurements are necessary to characterize the whole water splitting device.

### 3.2.3 External Quantum Efficiency (EQE)

The External Quantum Efficiency (EQE), also known as Incident Photon-to-Current Efficiency (IPCE) is the most important diagnostic efficiency for a PEC device and refers to the fraction of incident photons, of a given energy, that generate a photocurrent. Ideally each photon that hits a photoelectrode generates an electron, thus giving 100% EQE. EQE spectra are very useful to determine which photon energies are responsible of the observed photocurrent and are usually recorded varying the wavelength of the incident light source.

EQE accounts for the efficiencies of three fundamental processes involved in a semiconductor-based device, whether a solar cell or a PEC water splitting device (Eq. **3.1**). These are photon absorption (the fraction of electron-hole pairs generated for each incident photon, $\eta_{abs}$), charge transport to the solid-liquid interface ($\eta_{transp}$), and the efficiency of the interfacial charge transfer ($\eta_{ct}$).

$$EQE = \eta_{abs} \times \eta_{transp} \times \eta_{ct}$$    Eq. **3.1**

EQE is a common diagnostic figure of merit also for solar cells and in this work EQE in "wet" and "dry" configurations are reported. "Dry", or PV EQE, refers to EQE collected for **STO-GaAs** outside the solution in a classical two-contact photovoltaic measurement, where current is collected by evaporated metal contacts (Au/Ni/AuGe for the top electrode and Au/Cr for the back contact). On the other hand, "Wet", or PEC EQE, relates to EQE measurements with the photoelectrode in solution, and current collection occurs via HER instead than on metal contacts. Fig. **3.5a** and **3.5b** show schematics of the two different configurations.
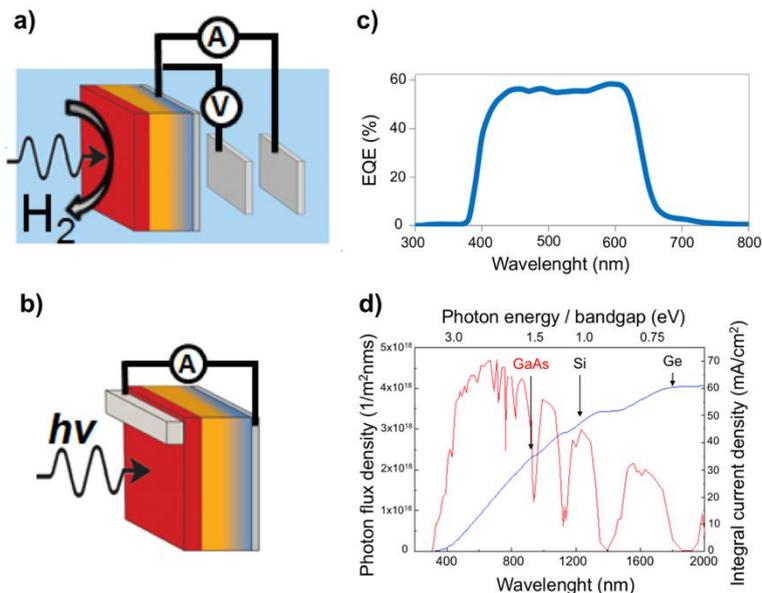
**Figure 3.5:** schematic of different measurement configurations. **a)** Three-electrode PEC configuration, where the working electrode is back-contacted to a titanium wire and the current of $H_2$ evolution is measured against a counter electrode with a potentiostat. **b)** Two-electrode PV configuration used for EQE and J-V measurements. The top electrode and the back contact are respectively made of Au/Ni/AuGe and Au/Cr. Electric current is recorded between these two electrodes. **c)** Typical spectra where EQE is evaluated at different wavelengths. **d)** Prediction of maximum expected current density under 1 sun illumination as a function of semiconductors' bandgap. The current densities reported on the right axis refer to 100% EQE and are obtained by integration over the AM1.5g solar spectrum, whose photon flux is reported in red.

PEC EQE are generally measured at a fixed $E_{app}$ varying the wavelenght of the incident illumination (Fig. **3.5c**). They are particularly useful to understand which photons contribute to the solar photocurrent, also highlighting the causes of possible losses in the semiconductors (recombination of carriers, scattering effects). Because of the need for monochromatic light, EQE spectra are recorded with illumination intensities that are much lower than the standard AM1.5g (100 mW/cm$^2$). This is practically connected to the generation of low photocurrents and, for this and other technical reasons, the use of a lock-in amplifier (coupled with a potentiostat) is required. Other possible diagnostic criteria that EQE spectra can reveal will be highlighted later in the chapter during the discussion of the experimental results.

EQE is also a good tool to predict the performance of a PEC water splitting device. Multiplying the photon energy of the incoming sunlight (relative to the AM1.5g

solar spectrum, left axis of Fig. **3.5d**) by the fraction of incident photons that are converted to electric current is possible for a given semiconductor to estimate the expected current at 1 sun illumination. The EQE to consider in the calculation is that obtained at 0 $V_{RHE}$. Fig. **3.5d** highlights the cases of GaAs, Si and Ge (vertical arrows) with the maximum expected currents in the case of 100% EQE reported on the y-axis at right. It is possible to notice that the lower the bandgap, the higher the maximum achievable current density. This trend has however to be paralleled also with the fact that very low bandgap semiconductors, e.g. Ge, are not able to generate a large photovoltage. Multiple junction devices (more than three) would be necessary to have enough driving force for water splitting, then increasing the complexity of the device.

### 3.2.4 Photoelectrode efficiency and Solar-to-Hydrogen Efficiency (STH)

In order to optimize independently each photoelectrode it is useful to calculate the solar conversion efficiency for the photocathode and the photoanode separately one from the other. It is however important to keep in mind that the power produced by each photoelectrode represents just a portion of the total free energy needed to split water. The efficiency of a single photoelectrode ($\eta_{PE}$) can be calculated with Eq. **3.2** from plots of the photocurrent density as a function of the applied potential (J-V data):

$$\eta_{PE} = \frac{J_{mp} * V_{mp}}{P_{in}} \qquad\qquad \text{Eq. } \textbf{3.2}$$

where $J_{mp}$ is the current density at the maximum power point, $V_{mp}$ is the voltage at the maximum power point and $P_{in}$ (in W/cm$^2$) is the power of the incident illumination (0.1 W/cm$^2$ in the case of AM1.5g solar simulators). This efficiency is however different from the solar-to-hydrogen (STH) efficiency, the most important measurement that characterize a PEC device. STH ultimately refers to the chemical energy produced by the solar energy input and should be evaluated only in a two-electrode, unbiased, device where simultaneously $H_2$ and $O_2$ evolution occur. Since in this work only the photocathode assembly is analyzed, STH is not reported.

### 3.3. STO-GaAs: (Photo)-Electrochemical characterization

All the electrochemical characterization herein described has been done in a three-electrode cell, using a Ag/AgCl R.E. and a Pt mesh C.E. The glass cell (V = 250 ml) has flat optical quartz faces to provide minimal absorption of light and an optimal irradiation of the W.E. The working electrode assemblies were back contacted with titanium wires using an InGa eutectic and a silver paint. After drying, the back, sides, and wires were covered with a nonconductive epoxy so that only the $SrTiO_3$ protective layer was exposed to the electrolyte. The so-prepared working electrodes were immersed in solution from the top of the cell. For all the measurements a freshly-prepared neutral (pH 7) potassium PB in 18.2 MΩ deionized water was used as the electrolyte. For CV and CA measurements a 2 cm stirring bar was rotated at 500 rpm to agitate the solution and reduce bubbles accumulation on the electrode surface.

Prior to PEC measurements, the electrochemical cell was purged with Ar for at least 30 minutes to remove dissolved oxygen. Argon was flowed through the cell at 10 mL/min with the exhaust stream from the cell plumbed directly into the sampling loop of a G.C. for the on-line detection of gaseous products. Quantification by G.C. of the hydrogen generated during prolonged electrolysis (up to 24 hours) enabled a real time determination of the Faradaic Efficiency for PEC HER. Analysis of the gas phase occurred by automatic injection every 12 minutes of a 1 mL volume of gas.

### 3.3.1. Results & Discussion.

Electrochemical and PEC measurements of **STO-GaAs** have been performed on 8x8 $mm^2$ electrodes, which were contacted on the backside with a titanium wire and insulated with epoxy resin from the sides to form the photocathode. The PB electrolyte (pH 7) in which **STO-GaAs** was studied, has been selected for its non-corrosive and non-toxic nature. Despite the good stability of the $SrTiO_3$ layer at various pH, the choice of a neutral pH is advantageous for the long-term operation of the device. Accordingly to recent techno-economical analysis, to make viable a PEC approach for hydrogen production, water splitting devices should last for years to reduce the actual cost of hydrogen.[46] A neutral pH is therefore more favorable to reach the goal of years-standing photoelectrodes, membranes, etc. that even if

stable in some cases at extreme pH values are however more comfortable in mild solutions.

In Figure **3.6a** the PEC activity of **STO-GaAs** under AM1.5g standard illumination (1 sun) is reported and compared to that of **Nb:STO** and a Pt wire. The photovoltage generated by the GaAs solar cell can be considered like an additional potential that helps to drive HER, and results for **STO-GaAs** in cathodic HER currents that are positive of the thermodynamic limit (0 $V_{RHE}$). Under 1 sun, the catalyst-free **STO-GaAs** provides a $\sim 0.55$ V voltage gain with respect to the Pt wire at the threshold value of 1 mA/cm$^2$ (see the comparison of the purple and blue lines in Fig. **3.6a**). CVs of Fig. **3.6a** reveals for **STO-GaAs** an HER onset potential of $\sim 0.3$ $V_{RHE}$, and a large reduction current of 7 mA/cm$^2$ at 0 $V_{RHE}$ (blue line of Fig. **3.6a**). The noise in the current measurement below 0.1 $V_{RHE}$ arises from bubble formation and mass transport limitations. Comparing CVs of **Nb:STO** (green line) and **STO-GaAs** (blue line) it is possible to notice a positive shift of the latter by $\sim 1$ V. This value matches well with the gain in photovoltage ($V_{OC} = 0.95$ V) given by the GaAs solar cell (see Fig. **3.2b**). The fact that the CVs for **Nb:STO** and **STO-GaAs** are simply shifted by the additional $V_{OC}$ means that is likely that HER occurs on both SrTiO$_3$ surfaces in the same way. Then, the device maximizes the integration of the two components transforming the produced photovoltage into $E_{app}$, which is positively shifted of the same entity. From this first qualitative assessment, it is likely that the growth of a nanometric thick SrTiO$_3$ protective layer on GaAs does not lead to energetic losses or carriers' recombination within the solar cell (see also EQE experiments later on).

**b)**
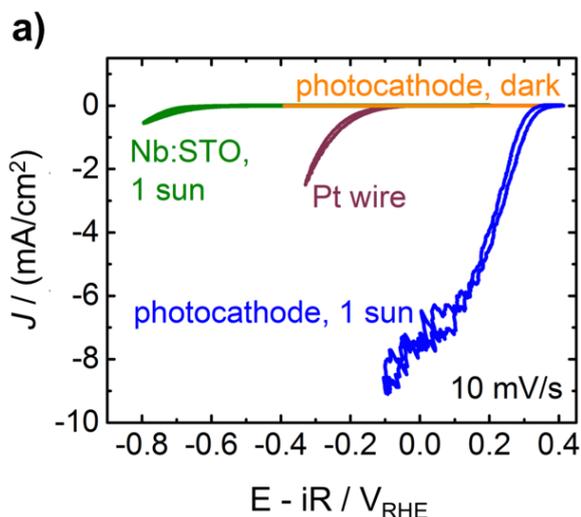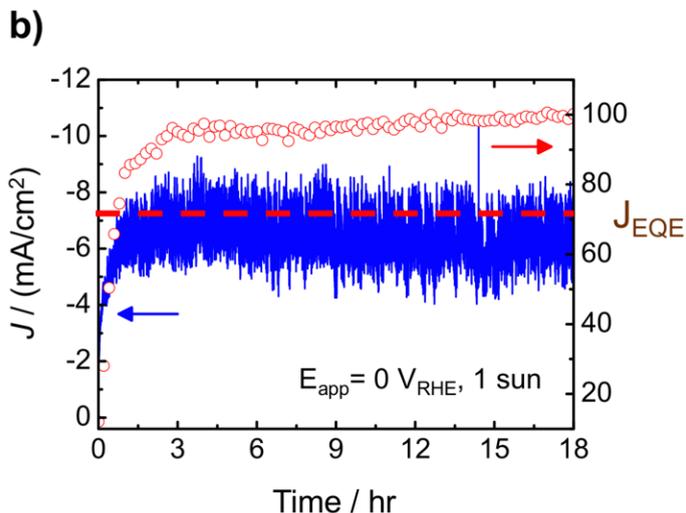


**Figure 3.6:** Photo-electrochemical performance and stability test of the **STO-GaAs** photocathode. The electrochemical measurements are performed in a 0.1 M potassium PB electrolyte solution (pH=7) with bubbling Ar and stirring the solution at 500 rpm to reduce mass transport limitations and $H_2$ bubbles accumulation on the electrode surface. **a)** CV at 10 mV/s ($5^{th}$ cycle shown) of hydrogen evolution currents for **STO-GaAs** photocathode in the dark (orange line) and under 1 simulated sun (AM1.5g, 100 mW/cm², blue line). For comparison, also CVs for **Nb:STO** (green line) and an HCl-cleaned Pt wire are shown. CVs of panel **a)** have been recorded after 24-hr solar hydrogen production of the respective samples at $E_{app}$ = 0 $V_{RHE}$ (for **STO-GaAs** samples) or $E_{app}$ = -0.4 $V_{RHE}$ (for **Nb:STO** and the Pt wire). The photovoltage generated by the np-GaAs solar cell ($V_{OC}$= 0.94 V) shifts the onset potential for HER positive of 0 $V_{RHE}$ for the **STO-GaAs** photocathode. **b)** Stability test during an 18-hr CA measurement for the **STO-GaAs** photocathode, overlaid with the Faradaic Efficiency calculated by on-line gas chromatography (red empty dots). The predicted current for **STO-GaAs** at $E_{app}$= 0 $V_{RHE}$ obtained from integration of the EQE spectra at the same applied potential is also reported (red dashed line).

The behavior over time of **STO-GaAs** toward solar-to-hydrogen production has been assessed by extended electrolysis at 0 $V_{RHE}$ and representative results are reported in Fig. **3.6b**. As can be seen, the **STO-GaAs** photocathode is able to sustain HER at the constant rate of $\sim$ 7 mA/cm² for about 18 hours (blue line, left axis), while maintaining a constant Faradaic Efficiency for the process of $\sim$ 100% (red dots, right axis). The stability of the photocathode has been also evaluated for up to 24 hours, a common benchmark test, with analogous results. It is to recall that the value of 7 mA/cm² agrees well with the prediction of the current density given by integration of the EQE spectra over the solar AM1.5g spectrum (see also section **3.3.6**) and is highlighted by the red dashed line of Fig. **3.6b**. A closer look to the J-t curve reveals how the HER current increases over the first 1.5 hours of electrolysis and then attains a constant value for the rest of the measurement. This effect is

consistent for all the samples studied and to exclude the contribution of possible contaminants in solution, the same CA measurements have been performed on a PB electrolyte that underwent a pre-electrolysis treatment. The procedure consisted of doing a galvanostatic electrolysis with sacrificial electrodes in the same electrolyte then used for the PEC characterization. Pre-electrolysis was performed at -0.15 mA/cm$^2$ for 12-14 hours in a two-electrode configuration, with carbon paper working and counter electrodes that were removed from the solution under potential control. This procedure allowed to purify the PB solution inducing the deposition of potential contaminants, especially metal cations $M^{n+}$, on the sacrificial working electrode. Doing this, are excluded the possible effects of metal impurities that may deposit on **STO-GaAs** for the application of a constant reductive potential over a long period of time and in a limited volume of solution. Nevertheless, after pre-electrolysis of the buffer (not shown) the same increase of current during the first hours of CA was observed and the beneficial behavior was ascribed to a peculiar activity of the photocathode assembly. For the sake of comparison all CV curves of Fig. **3.6a** have been recorded after 18/24-hours electrolysis.

### 3.3.2. Gas Detection and Faradaic Efficiency

The persistent noise in the J-t curve is due to extended hydrogen bubbles that occur during 1 sun illumination. Their nucleation and detachment from the electrode surface is reduced, but not completely eliminated, by stirring the solution. The hydrogen evolved form the **STO-GaAs** photocathode during CA has been measured using gas chromatography (SRI GC 8610C in Multi-Gas #3 configuration, equipped with a thermal conductivity detector, TCD). Gases were separated in a 6' Molecular Sieve 13X Packed Column and argon was used as the carrier gas. $H_2$ quantification is necessary to evaluate the F.E. of the process, highlighting possible efficiency losses due to **STO-GaAs** degradation or other parasitic reactions. Every 12 minutes a sample from the headspace of the cell, continuously flowed at 10 mL/min, was injected from the 1 mL sampling loop onto the column and detected by the TCD. In order to calibrate the $H_2$ signal from the TCD a two-point calibration was performed. For this purpose, a 5% $H_2/N_2$ gas mixture and a standard gas containing 100 ppm of $H_2$ were used as references.

Determination of the F.E. has been done using Eq. **3.3**:

$$F.E. = \frac{J_{HER}}{J_{TOT}} = \frac{A \times K \times F \times n \times P^0 \times flow}{RT} \qquad \text{Eq. } \textbf{3.3}$$

where $K$ is the conversion factor from TCD counts ($A$) to moles, $F$ is the Faraday constant, $n$ the electrons exchanged, $P^0$ the overpressure of the G.C. line (measured right before the sampling loop) and *flow* is referred to the purging gas flow (in $m^3$/s). It is important to note that the $H_2$ signal, and then apparently also the F.E., varies if the flow of the gas from the electrochemical cell is not constant (and the pressure too). To this end, the flow (10 mL/min) and the overpressure (~0.14 bar). were continuously controlled and monitored during measurements with a metering valve and a manometer.

As highlighted in Fig. **3.6b** (right axis), the F.E. for hydrogen production can be considered quantitative. F.E. in the order of 98±3% are found except for the first three hours of electrolysis when is seen an increase from 10% up to the final value. The initial lower F.E. is a characteristic of the experimental setup used and is due to the big dead volume of the cell. The evolved $H_2$ requires time to saturate the empty volume above the solution, hence the injections during the first three hours are not representative of a stationary situation and should be discarded for data analysis. This increase of F.E. is also disconnected from the increase of HER current. The time scale of the two events is different and, also in this case, is consistent throughout all the samples studied.

The remarkable stability of **STO-GaAs** revealed by CA is also confirmed by optical inspection of the photoelectrodes before and after PEC testing. Representative SEM images of **STO-GaAs** surfaces are shown in Fig. **3.7**. As it can be seen, **STO-GaAs** electrodes looks identical before (Fig. **3.7a**) and after (Fig. **3.7b**) extensive electrochemical testing, with no evidence of corrosion even after 24 hours of PEC hydrogen evolution. In contrast, in the absence of any $SrTiO_3$ protective layer, the corrosion of the bare GaAs solar cell upon photoelectrolysis is severe and occurs in less than an hour (Fig. **3.7c**). The only tangible difference is the presence of particles observed after testing (see Fig. **3.7b**). However, they are attributed to traces of residual electrolyte salts and not to sample degradation. Even EDX spectroscopy (not shown) before and after testing looks identical except for the elements present in the electrolyte salts.
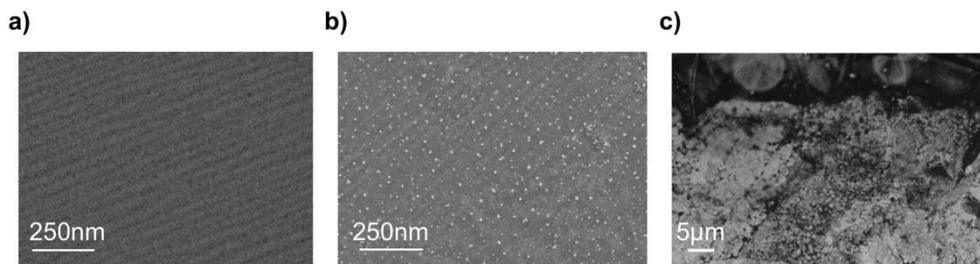
**Figure 3.7:** Scanning Electron Microscope (SEM) images of the **STO-GaAs** surface before **a)** and **b)** after testing in phosphate buffer. Image **b)** has been taken after all the (photo-)electrochemical characterization, including 24 hours CA under 1 sun illumination. The particles observed in **b)** are attributed to trace residual electrolyte salts that after rinsing with deionized water still remain on the surface of **STO-GaAs**.

The stability of the oxide layer during PEC operation is of crucial importance for the feasibility of this approach as a sustainable energy source. To evaluate the endurance and integrity of the $SrTiO_3$ layer after PEC testing, also XPS measurements were performed on the surface of the **STO-GaAs** photocathode before and after PEC characterization.

The Ti 2p peaks and Sr 3d XPS spectra are shown in Figure **3.8** after background subtraction. The Ti 2p peaks (Fig. **3.8a**) are identical before and after PEC operation. This peak is sensitive to the oxidation state of Ti, and displays a 4+ valence as expected for $SrTiO_3$[47] with no other oxidation states observable within the experimental resolution of XPS. In contrast to the Ti data, the Sr 3d spectra (Fig. **3.8b** and **3.8c**) show a reduction in the height and width of the peaks after PEC operation. This observation can be further investigated by fitting of the Sr 3d peaks to gain insights in the nature of the Sr oxidation states which cause the observed differences. The inset of Fig. **3.8c** shows how after PEC operation the Sr 3d peaks is originated by a single chemical state of Sr in $SrTiO_3$. In contrast, before PEC operation the additional features are attributed to a small amount of SrO on the surface of $SrTiO_3$.[48] It is not to exclude the possible participation of SrO in the initial activation process observed during photo-electrolysis but it is yet to be demonstrated.
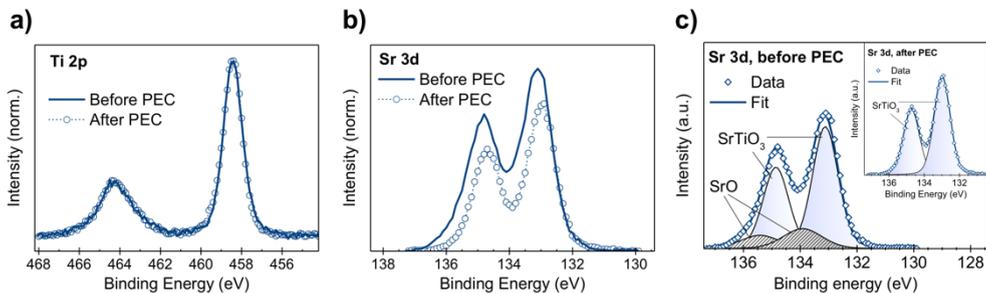
**Figure 3.8:** XPS analysis of the **STO-GaAs** surface before and after prolonged 24hours electrolysis at 0 $V_{RHE}$ under 1 sun illumination. Comparison between **a)** Ti 2p and **b)** Sr 3d orbitals. **c)** XPS spectra before PEC hydrogen evolution reveal a contribution of SrO species (dark grey) to the Sr 3d peak. After electrolysis, those contributions are not present and only $SrTiO_3$ species (light blue areas) are responsible of the Sr 3d peak.

### 3.3.3. Electronic band structure at the SrTiO₃-GaAs interface: XPS analysis.

The large solar-to-hydrogen currents reported in Fig. **3.6** and **3.7** are likely obtained for the optimal band alignment present in the **STO-GaAs** photoelectrode. To derive a quantitative description of the relative band positions XPS analysis has been used to highlight the electronic band structure at the $SrTiO_3$-GaAs interface. In Fig. **3.9** are reported the XPS spectra of a "Bare GaAs" solar cell in the absence of any $SrTiO_3$ layer (orange line), of a **STO-GaAs** photoelectrode ("Thick STO", red line) and a thin **STO-GaAs** photoelectrode (4nm, "Thin STO", green line). The valence band energy can be determined from these plots by the point at which the photoelectron intensity goes to zero (highlighted by the blue circles). This binding energies by themselves are however not absolute values (they depend on multiple factors)[49] and to draw conclusions regarding the band alignment at the $SrTiO_3$-GaAs interface relative comparisons are necessary. To this end a common strategy to derive the band energy offset between thin films grown on semiconductors is to acquire XPS spectra for the case of very thin films (the "Thin STO" spectrum of Fig. **3.9**), that allow to reveal the contribution of both the surface layer ($SrTiO_3$) and the underlying semiconductor (GaAs).[50,51] Indeed, the XPS spectrum of a thin **STO-GaAs** (green line) enables to collect photoelectrons from both the $SrTiO_3$ and the GaAs. Comparison with "thick" **STO-GaAs** and GaAs, where the oxide and GaAs signals dominate, allows to align the spectra by the position of the common peaks (As 3d and Ti 3p). With this procedure it is possible to determine the real energy

offset at the oxide-semiconductor interface, that is represented by the purple arrow of Fig. **3.9** and for **STO-GaAs** is in the order of 2.6 eV.
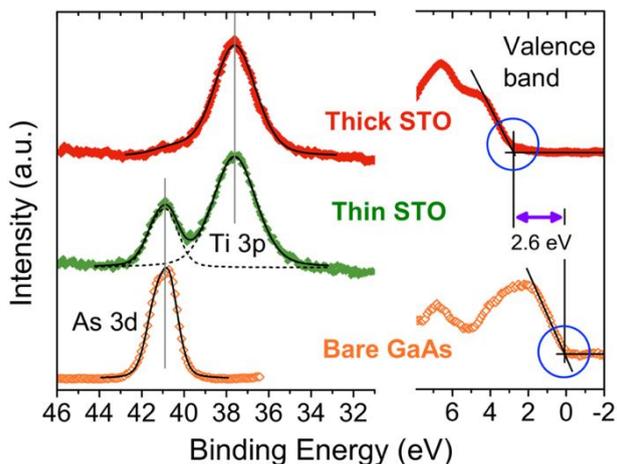


**Figure 3.9:** Band structure analysis of the oxide-semiconductor interface. XPS spectra of the As 3d, Ti 3p and the valence band of thick (16 nm, red line) and thin (4nm, orange line) **STO-GaAs** surface, as well as those of clean GaAs interface. The valence band offset between SrTiO$_3$ and GaAs is highlighted by the purple horizontal arrow. The indicated value of 2.6eV is identical to that reported in the band diagram of Fig. **3.1**. Courtesy of Dr. Lior Kornblum, University of Yale.

This high energy barrier is the same to which the caption of Fig. **3.1** and the text of section **3.1** refers to, and is beneficial because prevents holes recombination at the surface. Knowing the E$_g$ for SrTiO$_3$ and GaAs, from the obtained value of the valence band offset it can be calculated the conduction band offset, that is 0.7 eV.

### 3.3.4. Electronic structure at the SrTiO$_3$-electrolyte interface: Mott-Schottky analysis.

The energy offset still unknown in the schematic band diagram of Fig. **3.1b** is that at the oxide-electrolyte interface. The energy position of the SrTiO$_3$ conduction band edge can be experimentally determined by Mott-Schottky analysis. In this specific case it is convenient to perform EIS measurements with the **Nb:STO** model system previously described. In this case of major interest is the possibility to determine the flatband potential, E$_{FB}$. As mentioned in Chapter 1, by the application of an appropriate potential it is possible to reduce the band bending up to a point where the bands are completely flat.[52] Analyzing the behavior of the space charge capacitance C$_{SC}$ as a function of E$_{app}$ the conduction band energy can thus be

evaluated. This analysis assumes that the energetic offset of **Nb:STO** with the PB electrolyte approximates the offset at the surface of the epitaxial **STO-GaAs** photoelectrode, but due to the similarity between **Nb:STO** and SrTiO₃,[34] it is a reasonable speculation.
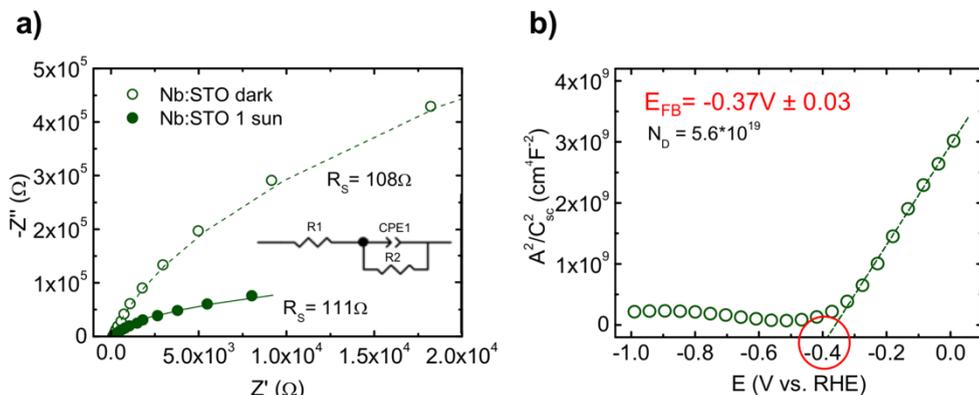


**Figure 3.10:** EIS characterization of **Nb:STO** in 0.1 M PB (pH=7). **a)** Nyquist plot of **Nb:STO** at open circuit voltage in the dark (empty dots) and under 1 sun illumination (filled dots). The inset displays the equivalent circuit used for data fitting, from which the values of $R_S$ in the various cases have been determined. **b)** Mott-Schottky plot of **Nb:STO** extracted from impedance data at the fixed frequency of 1.8 kHz (previously determined by analysis of the EIS spectra in the same electrolyte). Fitting the linear portion of the curve yields a $E_{FB}$ = 0.37 ± 0.3 $V_{RHE}$. The estimated donor density is $5.6\times10^{19}$ cm$^{-3}$

EIS data of **Nb:STO** are reported in Fig. **3.10a**. The inset shows the equivalent circuit used to fit the experimental data, where the constant phase element (CPE1) combines the capacitance of the Helmholtz double-layer and of the depletion layer within the semiconductor. Following EIS spectra, Mott-Schottky plots were then acquired from 0 V to -1 $V_{RHE}$ at a fixed frequency of 1.8 kHz. A representative M-S plot is reported in Fig. **3.10b**. To estimate the donor density ($N_D$), a dielectric constant ($\varepsilon$) of 310[53] and a surface area of 0.094 cm$^2$ have been used, yielding $N_D$ of 6×10$^{19}$ cm$^{-3}$ in good agreement with reported values.[54] Fitting of the potential-dependent linear region between 0 V and -0.4 $V_{RHE}$ allow to extract a $E_{FB}$ of -0.37 $V_{RHE}$ in the phosphate buffer of use. This value is slightly less negative than values measured in alkaline 0.1 M KOH and thus more favorable for allowing photogenerated electrons to perform efficient hydrogen evolution.[55]

From the $E_{FB}$ of -0.37 $V_{RHE}$ the band alignment at the oxide-electrolyte interface is finally approximated. It is to note the large overpotential of 370 mV present at the surface of **STO-GaAs**. This large electronic driving force has been shown to be

sufficient to promote hydrogen evolution kinetics even in the absence of HER catalysts.

### 3.3.5. Band diagram calculation.

The energy diagrams schematized in Fig. **3.1** are idealized representations of the **STO-GaAs** photocathodes, just to highlight the operating principles. Indications of the energy offsets at the various interfaces, bands bending and carriers' levels are not accurately described and the lengths are not in scale. Following XPS and Mott-Schottky analysis, all the required energetic characteristics of the system are available and it is possible to derive quantitative band diagrams for **STO-GaAs** both in the dark and under illumination. The band diagrams have been calculated using ADEPT 2.1,[56] a Poisson equation solver, and the results are reported in Fig. **3.11**. The situation when **STO-GaAs** is equilibrated in the dark (i.e. the Fermi energy within the device is the same) is shown in Fig. **3.11a**, while in Fig. **3.11b** is simulated the illumination of **STO-GaAs** at 1 sun intensity.
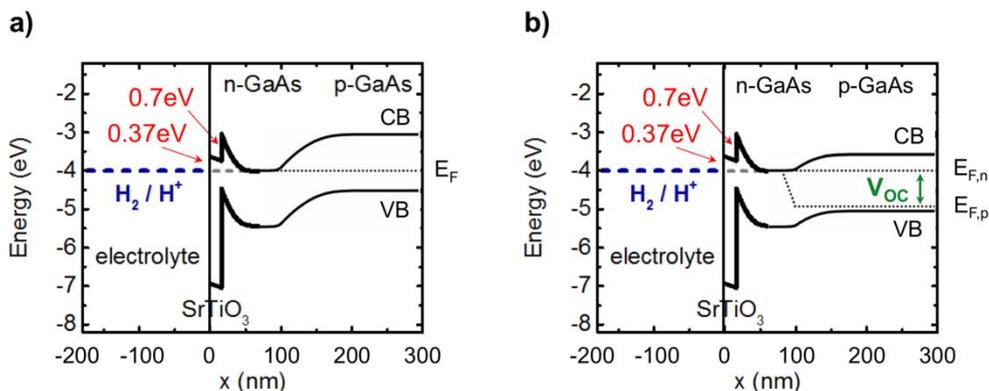


**Figure 3.11: a)** Band energies at the electrolyte/SrTiO$_3$ and SrTiO$_3$/GaAs interfaces after equilibration with the H$^+$/H$_2$ couple in the dark. The offset between the conduction bands of GaAs and SrTiO$_3$ (0.7 eV, as determined by XPS), and the energy offset at the semiconductor-electrolyte interface (0.37 eV, as determined by Mott-Schottky analysis) are highlighted in red. **b)** Band energies for **STO-GaAs** under 1 sun illumination and at open circuit. It is to note the mismatch between the CB of n-GaAs and the CB of SrTiO$_3$. All the diagrams are in scale and have been simulated using ADEPT 2.1.

The front contact is represented by the [H$^+$/H$_2$] couple and is placed at an energy 0.37 eV below that of the electron affinity of the SrTiO$_3$ protective layer. The doping concentrations in the various layers of the GaAs solar cell are those reported in Fig. **3.2a**. Additional material properties like dielectric constants, holes/electrons

mobility and lifetimes, absorption and recombination coefficients are taken from reported data.[57-61]

When the electron energy equilibrates, the bands of GaAs at the interface with SrTiO$_3$ bend upwards, forming a barrier for electron transport to the SrTiO$_3$ conduction band. The height of this barrier is more pronounced to what initially estimated (note the little mismatch between the CB of SrTiO$_3$ and n-GaAs that hinders the spontaneous flow of electrons when **STO-GaAs** is illuminated). When the solar cell is illuminated, a portion of the generated V$_{OC}$ (Fig. **3.11b**) is needed to reduce the magnitude of the barrier at the SrTiO$_3$-GaAs interface and to produce HER current. Also the depth of the depletion layer that forms in the n-doped region of GaAs is considerable, in the order of 35 nm. As it will be shown in section **3.3.7**, both factors limit the reach of a high conversion efficiency.

### 3.3.6. External Quantum Efficiency measurements.

EQE measurements are a great diagnostic tool to evaluate several features of solar cells. From the wavelength-dependence of EQE is indeed possible to unravel losses related to the dynamics of photogenerated carriers (e.g. recombination losses) or to a non optimal absorption (reflection of incident light). Also physical properties of the semiconductor, like the bandgap energy, can be derived.

In Fig. **3.12a** are reported PEC EQE spectra for **STO-GaAs** (see section **3.2.3.**) at different E$_{app}$. It is possible to note a big increment of EQE in the visible part of the spectra on passing from +0.125 V$_{RHE}$ to 0 V$_{RHE}$. However, the application of more negative potentials has a minor effect in a further increase of EQE, which levels off at a limiting value of ~62%. This behavior is consistent to the situation highlighted in the band diagrams of Fig. **3.11**. Under 1 sun at OCP (~0.7 V$_{RHE}$) the electrons flow towards the solution is not very efficient for the high energy barrier at SrTiO$_3$-GaAs interface. As E$_{app}$ is made more negative, the E$_F$ of GaAs is raised and the bands shift accordingly to higher energies. Doing this has initially a great influence in reducing the barrier height at the SrTiO$_3$-GaAs interface (up to E$_{app}$= 0 V$_{RHE}$), but a further increase of E$_F$ does not eliminate completely the band bending of the depletion region in n-GaAs and explains the flattening of EQE at the most negative E$_{app}$. The inset of Fig. **3.12a** displays the EQE spectrum taken at E$_{app}$ = 0 V$_{RHE}$, whose integration over the standard AM1.5g solar spectrum gives a prediction of the current density obtained during CA at the same E$_{app}$. From the integration, a current

density of 7.2 mA/cm$^2$ was expected (red dashed line of Fig. **3.6b**), in very good agreement with the experimental value of 7 mA/cm$^2$ from CA.

**a)**                                                              **b)**
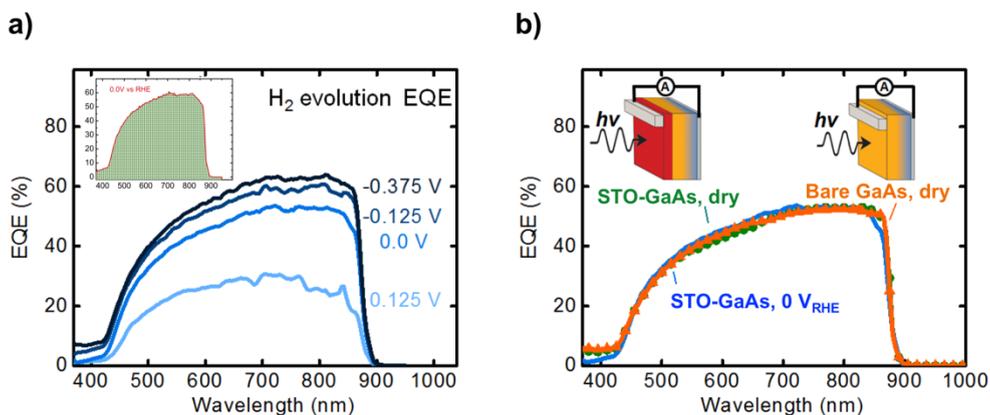


**Figure 3.12:** EQE spectra for **STO-GaAs** photocathodes. **a)** PEC EQE at different applied potentials in 0.1 M phosphate buffer (pH=7). The inset shows integration of EQE at 0 V$_{RHE}$, from which the expected current at 0 V$_{RHE}$ during CA under 1 sun illumination can be estimated (red dashed line of Fig. **3.6b**). Potentials are reported vs. RHE. **b)** Summary of EQE measurements for **STO-GaAs**. PV two-contact photovoltaic measurements with (green curve) and without the protective SrTiO$_3$ layer (orange curve), compared to the PEC EQE at 0 V$_{RHE}$ (blue curve, the same of panel **a**). PV EQE spectra are courtesy of Dr. Lior Kornblum, University of Yale.

In Fig. **3.12b** PEC and PV EQE spectra are compared. The PV EQE spectra of **STO-GaAs** and **GaAs** point out the possible effects that the SrTiO$_3$ layer has on light absorption and carrier dynamics. On the other hand, a comparison with the PEC spectrum of **STO-GaAs** biased at $E_{app} = 0$ V$_{RHE}$ allows to evaluate the effects of having the [H$^+$/H$_2$] redox couple as the front current collector.

The general absence of any EQE decay at increasing wavelengths is an indication of a good solar cell engineering. As the wavelength increases, light is absorbed more deep in the semiconductor and the photogenerated carriers have to make a longer distance to be collected, increasing the probability of recombination. The absence of such recombination losses in the bulk is a sign of a good, but not excellent, engineering of the np-GaAs solar cell. Indeed, PV EQE in the order of 85% are not unreal[62] and there is a substantial opportunity for further improvements in the solar cell design, possibly by reducing reflective losses.

Comparing the spectra of Fig. **3.12b**, it is evident that all PEC and PV EQE are identical. EQE is not affected by the addition of the epitaxial SrTiO$_3$ oxide and, more importantly, by the collection of current via HER. The latter is significant because since EQE depends on $\eta_{ct,}$ (see section **3.2.3**) this means that HER is not limited at

all by kinetics, likely for the big driving force at the surface (0.37 eV). Also $\eta_{transp}$ appear to be the same in PEC and PV EQE, so even electron transport to the surface at 0 $V_{RHE}$ (and at more negative $E_{app}$) is not limiting the generation of PEC current.

### 3.3.7. STO-GaAs conversion efficiency

The big energy gap at the $SrTiO_3$-electrolyte interface if from one side allows high HER currents to flow (for the high $\eta_{ct,}$), however limits the energy efficiency of **STO-GaAs**. The efficiency of the photoelectrode for PEC HER can be calculated from Eq. **3.2** using the CV data of **STO-GaAs** in Fig. **3.6a**. The conversion efficiency at the maximum power point is only 0.55%, a scarce value if compared to the maximum available from the np-GaAs solar cell that is ~10% (see inset of Fig. **3.2b**). In order to improve the efficiency of the device, a trade off between enough driving force (to circumvent the need of catalysts) and energy losses has to be realized. A possible strategy can be envisaged by tailoring the oxide's band structure[41] to increase the electron affinity just enough so that the remaining offset at the water-oxide interface is sufficient to drive HER without the aid of a catalyst.

Nevertheless, probably the weakest point of **STO-GaAs** resides at the interface between $SrTiO_3$ and GaAs. The energy offset of 0.7 eV is a rather big energy barrier that is likely the be the major cause of efficiency losses. If there were no CB offset at the $SrTiO_3$/n-GaAs interface, the 0.94 V $V_{OC}$ of the solar cell could shift the onset potential of HER from -0.37 $V_{RHE}$ (the $E_{FB}$ of $SrTiO_3$ in the dark) to ~0.55 $V_{RHE}$ under illumination. Due to the loss of electron energy at the CB offset, actually STO-GaAs has an onset at ~0.30 $V_{RHE}$ (Fig. **3.6a**). Thus, ~0.25 V could be gained tuning the interface chemistry[63] so as to reduce the energy gap between the CB of $SrTiO_3$ and n-GaAs.

Another aspect that prevents to reach a higher conversion efficiency and limits the performances of **STO-GaAs** is the process of electron transport toward the surface ($\eta_{transp}$). As mentioned in section **3.3.5.**, the depletion width of the n-GaAs layer is in the order of 35 nm, a length scale that is not very favorable for electrons' tunneling. A possible and simple strategy to solve the problem is to create a thin heavily-doped layer of n-GaAs. Increasing the doping density would lead to a narrower depletion width (the barrier height remains the same), then to an increased rate of electron transport.

The effects of such a low efficiency can be visualized in Fig. **3.13**, where J-V data of **STO-GaAs** are paralleled to those of other PEC photocathodes reported in literature.
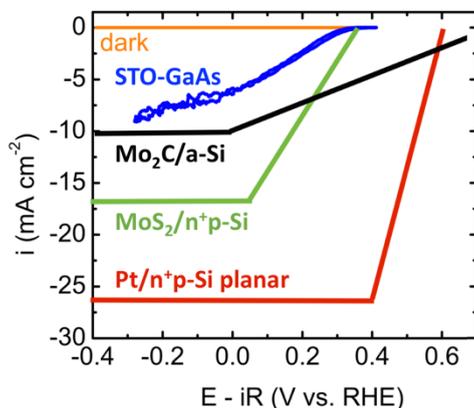


**Figure 3.13:** comparison of PEC HER data for several photocathodes (ref [27] for the green line, ref [28] for the black line and ref [32] for the red line). J-V data for the examples taken from literature reports were collected in 0.5 M $H_2SO_4$, while for **STO-GaAs** in PB at pH=7.

The low slope of the J-V curve observed for **STO-GaAs** results from the above-mentioned losses within the device. It is very likely that a positive shift of the J-V curve (for the better exploitation of the $V_{OC}$) and a faster electron transport to the surface (improving band offset at the $SrTiO_3$-GaAs interface) would result in steeper curves and higher limiting currents, thus increasing the efficiency.

It is worth mentioning that the higher stationary currents for the examples of Fig. **3.13** are related to the higher current densities obtainable by the Si-based solar cells that they enclose (see also Fig. **3.5d**). Moreover, the acidic electrolyte used in the examples reported may help PEC HER. The rate of PEC HER is not affected by concentration overpotentials as much like in "dark" electrochemistry, however having a greater availability of protons could be beneficial for **STO-GaAs** activity.

Summarizing, several aspects of **STO-GaAs** can be improved to magnify the efficiency and the overall performances of the photocathode. However, the concept that is highlighted is the fact that by a proper design of PEC water splitting devices, not always surface catalysis is necessary and catalyst-free devices are a reasonable strategy. This is confirmed for example in the present case. Addition of a Pt layer (deposited by ALD) on the surface of **STO-GaAs**, giving **Pt/STO-GaAs**, is not translated with higher activities. The results, not shown, evidence how the

addition of Pt does not affect PEC HER efficiency. The current density for **Pt/STO-GaAs** during electrolysis at 0 $V_{RHE}$ under 1 sun illumination are only slightly higher than **STO-GaAs** (7.6 mA/cm$^2$ vs. 7.4 mA/cm$^2$) and the efficiency at the maximum power density is only 0.61% (vs. 0.55%). Also PEC EQE spectra for **Pt/STO-GaAs** are identical to those of **STO-GaAs**.

## 3.4. Conclusions & Outlooks

Despite the evident improvements that can be realized, this study has however demonstrated in the context of solar fuels production the robustness and feasibility of integrating the III-V photovoltaic technology with the growth of high-quality, single-crystal epitaxial oxides. Their combination has proved to be a valid strategy for the further development of photoelectrode assemblies.

Using a catalyst-free nanometric SrTiO$_3$ protective layer on top of a np-GaAs solar cell, a stable hydrogen evolution current is produced under 1 sun illumination with the resulting **STO-GaAs** photocathode. PEC EQE (an "electrons-out" per "photons-in" efficiency) for hydrogen production reaches 50% at 0 $V_{RHE}$ and exceeds 60% at more negative $E_{app}$. The high-quality of the SrTiO$_3$/GaAs interface prevents losses related to electron extraction and surprisingly PEC EQE match its PV analogous, with no leaks of efficiency on passing from a "dry" to a "wet" configuration. Moreover, results not shown, any advances in the solar cell engineering have been reflected in the performances of the final PEC device. Starting from a first, very simple, np-GaAs design with EQE of ~10%, and ending up with the presented solar cell, PEC and PV EQE have always been of the same entity. Also the PEC properties of **STO-GaAs**, and the efficiency accordingly, increased as the solar cell was improved.

Band diagram calculations have been an important part of the work to identify the reasons for the low conversion efficiency of **STO-GaAs**. Calculation of band energies with a combined experimental and theoretical work, allowed to highlight the weak points and to envisage strategies for the optimization of the device. Band diagram calculations have also the potentiality to be used not merely as a diagnostic tool, but also to predict the potentiality of a certain material. For the possibility to evaluate *a-priori* some fundamental material's characteristics band diagram calculations are then a very advisable tool for the rapid development of PEC water splitting devices and their role in the actual PEC research should be emphasized.

Extending the approach presented in this work to high-efficiency tandem solar cells, offers the potential to generate sufficient photovoltage for stable and unassisted water splitting. For example, a III-V PV on a Si dual-junction cell operating as a photocathode could achieve photovoltages well in excess of the 1.23 V thermodynamic minimum required for water splitting.[42,43]

In addition, the concept here demonstrated of a catalyst-free platform for solar hydrogen production can also be adopted in the design of other solar cells-semiconductors combinations, or for other relevant energy-related applications, like oxygen evolution or $CO_2$ reduction. Especially the latter may benefit from the specific features of **STO-GaAs**, where the driving force present at the electrolyte interface can be exploited for $CO_2RR$, that usually requires high overpotential to occur.

Another possible and very intriguing strategy is the protection of a np-solar cell with $CeO_2$. Ceria is a very stable oxide with demonstrated applications as anti-corrosive coating.[64] Coupling its stability with the interesting electrochemical properties towards $CO_2RR$ demonstrated in Chapter 2 is for sure of great interest and could give surprising results. Moreover, $CeO_2$ thin films can be produced accordingly to several procedures,[65,66] and there are also examples of nanometric ceria coating on Si,[67] making rather straightforward further steps in this context.

Always concerning $CO_2RR$ another possibility arises from the study of the state-of-the-art oxide-derived-copper catalyst[68,69] in combination with Si. The coating of p-Si with electrodeposited oxide-derived copper would prevent p-Si from corrosion and at the same time provides an optimal surface chemistry to convert $CO_2$ to fuels. To conclude, combining the tunability of complex oxides and the sophisticated engineering of solar cells, whether III-V or the more abundant Si, could allow to get large gains towards efficient solar fuels production and a pervasive diffusion of PEC technology.

# 3.5. Bibliography

1. A. Fujishima, K. Honda, Electrochemical Photolysis of Water at a Semiconductor Electrode. *Nature*, **238**, 37–38 (1972).
2. S. Hu, M. R. Shaner, J. A. Beardslee, M. Lichterman, B. S. Brunschwig, N. S. Lewis, Amorphous $TiO_2$ coatings stabilize Si, GaAs, and GaP photoanodes for efficient water oxidation. *Science,* **344**, 1005–1009 (2014).
3. S. C. Warren, K. Voïtchovsky, H. Dotan, C. M. Leroy, M. Cornuz, F. Stellacci, C. Hébert, A. Rothschild, M. Grätzel, Identifying champion nanostructures for solar water-splitting. *Nat Mater*, **12**, 842–849 (2013).
4. M. Schreier, L. Curvat, F. Giordano, L. Steier, A. Abate, S. M. Zakeeruddin, J. Luo, M. T. Mayer, M. Gratzel, Efficient photosynthesis of carbon monoxide from $CO_2$ using perovskite photovoltaics. *Nat Commun*, **6**, 7326 (2015).
5. F. Studt, I. Sharafutdinov, F. Abild-Pedersen, C. F. Elkjær, J. S. Hummelshøj, S. Dahl, I. Chorkendorff, J. K. Nørskov, Discovery of a Ni-Ga catalyst for carbon dioxide reduction to methanol. *Nat. Chem.*, **6**, 320–324 (2014).
6. M. A. Green, K. Emery, Y. Hishikawa, W. Warta, E. D. Dunlop, Solar cell efficiency tables (Version 45). *Prog. Photovoltaics Res. Appl.*, **23**, 1–9 (2015).
7. A. Shah, P. Torres, R. Tscharner, N. Wyrsch, H. Keppner, Photovoltaic Technology: The Case for Thin-Film Solar Cells. *Science*, **285**, 692-698 (1999).
8. M. A. Green, Thin-film solar cells: review of materials, technologies and commercial status, *J. Mater. Sci: Mater. Electron.*, **18**, S15–S19 (2007)
9. A. G. Aberle, Thin-film solar cells, *Thin Solid Films*, **517** 4706–4710 (2009)
10. H. Gerischer, On the stability of semiconductor electrodes against photodecomposition. *J. Electroanal. Chem. Interfacial Electrochem.*, **82**, 133–143 (1977).
11. O. Khaselev, J. A. Turner, A Monolithic Photovoltaic-Photoelectrochemical Device for Hydrogen Production via Water Splitting. *Science*, **280**, 425–427 (1998).
12. R. B. Comes, S. Y. Smolin, T. C. Kaspar, R. Gao, B. A. Apgar, L. W. Martin, M. E. Bowden, J. B. Baxter, S. A. Chambers, Visible light carrier generation in co-doped epitaxial titanate films. *Appl. Phys. Lett.*, **106**, 092901 (2015).
13. C.-B. Eom J. L. MacManus-Driscoll, Preface for Special Topic: Frontiers in Oxides: Properties and Electronic Applications. *APL Mater.*, **3**, 062201 (2015).
14. W. Hong, M. Risch, K. A. Stoerzinger, A. J. L. Grimaud, J. Suntivich, Y. Shao-Horn, Toward the rational design of non-precious transition metal oxides for oxygen electrocatalysis. *Energy Environ. Sci.*, **8**, 1404–1427 (2015).
15. M. G. Walter, E. L. Warren, J. R. McKone, S. W. Boettcher, Q. Mi, E. A. Santori, N. S. Lewis, Solar water splitting cells, *Chem. Rev.,* **110**, 6446–6473 (2010)
16. K. Sivula, R. van de Krol. Semiconducting materials for photoelectrochemical energy conversion, *Nat. Rev. Mats.,* **1**, 1-16 (2016).

17. L. Ji, M. D. McDaniel, S. Wang, A. B. Posadas, X. Li, H. Huang, J. C. Lee, A. A. Demkov, A. J. Bard, J. G. Ekerdt, E. T. Yu, A silicon-based photocathode for water reduction with an epitaxial $SrTiO_3$ protection layer and a nanostructured catalyst. *Nat. Nano*, **10**, 84–90 (2015).
18. C. R. Cox, J. Z. Lee, D. G. Nocera, T. Buonassisi, Ten-percent solar-to-fuel conversion with nonprecious materials. *Proc. Natl. Acad. Sci.,* **111,** 14057–14061 (2014).
19. M. J. Kenney, M. Gong, Y. Li, J. Z. Wu, J. Feng, M. Lanza, H. Dai, High-Performance Silicon Photoanodes. *Science,* **342**, 836–840 (2013).
20. J. J. H. Pijpers, M. T. Winkler, Y. Surendranath, T. Buonassisi, D. G. Nocera, Light-induced water oxidation at silicon electrodes functionalized with a cobalt oxygen-evolving catalyst. *Proc. Natl. Acad. Sci.*, **108**, 10056–10061 (2011).
21. Y. W. Chen, J. D. Prange, S. Dühnen, Y. Park, M. Gunji, C. E. D. Chidsey, P. C. McIntyre, Atomic layer-deposited tunnel oxide stabilizes silicon photoanodes for water oxidation. *Nat. Mater.*, **10**, 539–544 (2011).
22. E. Verlage, S. Hu, R. Liu, R. J. R. Jones, K. Sun, C. Xiang, N. S. Lewis, H. A. Atwater, A monolithically integrated, intrinsically safe, 10% efficient, solar-driven water-splitting system based on active, stable earth-abundant electrocatalysts in conjunction with tandem III–V light absorbers protected by amorphous $TiO_2$ films. *Energy Environ. Sci.* **8**, 3166-3172 (2015).
23. M. Malizia, B. Seger, I. Chorkendorff, P. C. K. Vesborg, Formation of a p–n heterojunction on GaP photocathodes for $H_2$ production providing an open-circuit voltage of 710 mV. *J. Mater. Chem. A*, **2**, 6847 (2014).
24. B. Seger, T. Pedersen, A. Laursen, P. Vesborg, O. Hansen, I. Chorkendorff, Using $TiO_2$ as a Conductive Protective Layer for Photocathodic $H_2$ Evolution. *J. Am. Chem. Soc.*, **135**, 1057–1064 (2013).
25. A. B. Laursen, T. Pedersen, P. Malacrida, B. Seger, O. Hansen, P. C. K. Vesborg, I. Chorkendorff, $MoS_2$-an integrated protective and active layer on $n^+$p-Si for solar $H_2$ evolution. *Phys. Chem. Chem. Phys.*, **15**, 20000–20004 (2013).
26. A. B. Laursen, S. Kegnæs, S. Dahl, I. Chorkendorff, Molybdenum sulfides—efficient and viable materials for electro - and photoelectrocatalytic hydrogen evolution. *Energy Environ. Sci.*, **5**, 5577-5591 (2012).
27. J. D. Benck, S. C. Lee, K. D. Fong, J. Kibsgaard, R. Sinclair, T. F. Jaramillo, Designing Active and Stable Silicon Photocathodes for Solar Hydrogen Production Using Molybdenum Sulfide Nanomaterials. *Adv. Energy Mater.*, **4**, 1400739 (2014).
28. C. G. Morales-Guio, K. Thorwarth, B. Niesen, L. Liardet, J. Patscheider, C. Ballif, X. Hu, Solar Hydrogen Production by Amorphous Silicon Photocathodes Coated with a Magnetron Sputter Deposited $Mo_2C$ Catalyst, *J. Am. Chem. Soc.*, **137**, 7035–7038 (2015).
29. J. Luo, J-H. Im, M. T. Mayer, M. Schreier, M. K. Nazeeruddin, N-G. Park, S. D.

Tilley, H. J. Fan, M. Grätzel, Water photolysis at 12.3% efficiency via perovskite photovoltaics and Earth-abundant catalysts, *Science,* **345**, 1593-1596 (2014).

30. B. Seger, S. D. Tilley, T. Pedersen, P. C. K. Vesborg, O. Hansen, M. Gratzel, I. Chorkendorff, Silicon protected with atomic layer deposited TiO2: conducting versus tunnelling through TiO2, *J. Mater. Chem. A*, **1**, 15089-15094 (2013).

31. H.-P. Wang, K. Sun, S. Y. Noh, A. Kargar, M.-L. Tsai, M.-Y. Huang, D. Wang, J.-H. He, High-performance a-Si/c-Si heterojunction photoelectrodes for photoelectrochemical oxygen and hydrogen evolution. *Nano Lett.*, **15**, 2817–2824 (2015).

32. S. W. Boettcher, E. L. Warren, M. C. Putnam, E. a Santori, D. Turner-Evans, M. D. Kelzenberg, M. G. Walter, J. R. McKone, B. S. Brunschwig, H. a Atwater, N. S. Lewis, Photoelectrochemical hydrogen evolution using Si microwire arrays. *J. Am. Chem. Soc.*, **133**, 1216–1219 (2011).

33. C. R. Cox, M. T. Winkler, J. J. H. Pijpers, T. Buonassisi, D. G. Nocera, Interfaces between water splitting catalysts and buried silicon junctions. *Energy Environ. Sci.*, **6**, 532–538 (2013).

34. K. J. May, D. P. Fenning, T. Ming, W. T. Hong, D. Lee, K. A. Stoerzinger, M. D. Biegalski, A. M. Kolpak, Y. Shao-Horn, Thickness-Dependent Photoelectrochemical Water Splitting on Ultrathin LaFeO$_3$ Films Grown on Nb:SrTiO$_3$. *J. Phys. Chem. Lett.*, **6**, 977–985 (2015).

35. W. Shockley, H. J. Queisser, Detailed balance limit of efficiency of *p–n* junction solar cells, *J. Appl. Phys.* **32**, 510–519 (1961).

36. K. P. Kuhl, E. R. Cave, D. N. Abram, T. F. Jaramillo, New insights into the electrochemical reduction of carbon dioxide on metallic copper surfaces, *Energy Environ. Sci.*, **5**, 7050-7059 (2012).

37. S. M. Sze, K. K. Ng, *The Physics of Semiconductor Devices*, (Wiley, New York, ed. 3, 2007).

38. R. A. McKee, F. J. Walker, M. F. Chisholm, Crystalline oxides on silicon: the first five monolayers. *Phys. Rev. Lett.* **81**, 3014–3017 (1998).

39. Z. Yu, Y. Liang, C. Overgaard, X. Hu, J. Curless, H. Li, Y. Wei, B. Craigo, D. Jordan, R. Droopad, J. Finder, K. Eisenbeiser, D. Marshall, K. Moore, J. Kulik, P. Fejes. Advances in heteroepitaxy of oxides on silicon. *Thin Solid Films,* **462–463**, 51–56 (2004).

40. M. P. Warusawithana, Cheng Cen, C. R. Sleasman, J. C. Woicik, J. Li, L. Fitting Kourkoutis, J. A. Klug, H. Li, P. Ryan, L-P. Wang, M. Bedzyk, D. A. Muller, L-Q. Chen, J. Levy, D. G. Schlom, A ferroelectric oxide made directly on silicon. *Science,* **324**, 367–370 (2009).

41. A. A. Demkov, A. B. Posadas, H. Seo, M. Choi, K. J. Kormondy, P. Ponath, R. C. Hatch, M. D. McDaniel, T. Q. Ngo, J. G. Ekerdt, Monolithic integration of oxides on semiconductors. *ECS Transactions,* **54**, 255–269 (2013).

42. R. Contreras-Guerrero, M. Edirisooriya, O. C. Noriega, R. Droopad, Interface

properties of MBE grown epitaxial oxides on GaAs. *J. Cryst. Growth*, **378**, 238–242 (2013).

43. A.-B. Posadas, M. Lippmaa, F. J. Walker, M. Dawber, C. H. Ahn, J.-M. Triscone, *Physics of Ferroelectrics*, *Chap. 6: Growth and Novel Applications of Epitaxial Oxide Thin Films.* (Springer Berlin Heidelberg, 2007) pp. 219–304.

44. Z. Chen, T. F. Jaramillo, T. G. Deutsch, A. Kleiman-Shwarsctein, A. J. Forman, N. Gaillard, R. Garland, K. Takanabe, C. Heske, M. Sunkara, E. W. McFarland, K. Domen, E. L. Miller, J. A. Turner, H. N. Dinh, Accelerating materials development for photoelectrochemical hydrogen production: Standards for methods, definitions, and reporting protocols, *J. Mater. Res.*, **25**, 3-16, (2010).

45. http://rredc.nrel.gov/solar/spectra/am1.5/

46. B. A. Pinaud, J. D. Benck, L. C. Seitz, A. J. Forman, Z. Chen, T. G. Deutsch, B. D. James, K. N. Baum, G. N. Baum, S. Ardo, H. Wang, E. Miller, T. F. Jaramillo, Technical and economic feasibility of centralized facilities for solar hydrogen production via photocatalysis and photoelectrochemistry. *Energy Environ. Sci.* **6**, 1983–2002 (2013).

47. M. S. J. Marshall, D. T. Newell, D. J. Payne, R. G. Egdell, M. R. Castell, Atomic and electronic surface structures of dopants in oxides: STM and XPS of Nb- and La-doped $SrTiO_3$ (001). *Phys. Rev. B*, **83**, 35410 (2011).

48. K. Szot, W. Speier, U. Breuer, R. Meyer, J. Szade, R. Waser, Formation of micro-crystals on the (100) surface of $SrTiO_3$ at elevated temperatures, *Surf. Sci.*, **460**, 112 (2000).

49. P. van der Heide, *X-Ray Photoelectron Spectroscopy: an introduction to principles and practices,* (1st edition, Wiley, 2011).

50. S. A. Chambers, Y. Liang, Z. Yu, R. Droopad, J. Ramdani, K. Eisenbeiser, Band discontinuities at epitaxial $SrTiO_3$/Si(001) heterojunctions. *Appl. Phys. Lett.*, **77**, 1662 (2000).

51. L. Kornblum, M. D. Morales-Acosta, E. N. Jin, C. H. Ahn, F. J. Walker, Transport at the Epitaxial Interface between Germanium and Functional Oxides. *Adv. Mater. Interfaces*, **2**, 1500193-1500197 (2015).

52. S. R. Morrison, *Electrochemistry at Semiconductor and Oxidized Metal Electrodes* (Plenum Press, New York, 1980).

53. G. Rupprecht, R. O. Bell, Dielectric Constant in Paraelectric Perovskites. *Phys. Rev.*, **135**, A748–A752 (1964).

54. T. Watanabe, A. Fujishima, K. Honda, Photoelectrochemical Reactions at $SrTiO_3$ Single Crystal Electrode. *Bull. Chem. Soc. Jpn.*, **49**, 355–358 (1976).

55. T. Ming, J. Suntivich, K. J. May, K. A. Stoerzinger, D. H. Kim, Y. Shao-Horn, Visible Light Photo-oxidation in Au Nanoparticle Sensitized $SrTiO_3$:Nb Photoanode. *J. Phys. Chem. C*, **117**, 15532–15539 (2013).

56. J. Gray, X. Wang, R. Vamsi, K. Chavali, X. Sun, A. Kanti J. R. Wilcox, "ADEPT 2.1" https://nanohub.org/resources/adeptnpt. (2015) DOI: 10.4231/D39S1KM3S

57. J. D. Wiley, *Semiconductor and Semimetals*, in R. K. Willardson and A. C. Beer, eds. (Academic Press, N.Y., vol. 10, 1975)

58. V. P. Varshni, Band-to-Band Radiative Recombination in Groups IV, VI, and III-V Semiconductors, *Phys. Status Solidi*, **19**, 459-514 (1967). 20, 1 (1967) 9-36.

59. http://www.ioffe.ru/SVA/NSM/Semicond/GaAs

60. D.C. Look, D.K. Lorance, J.R. Sizelove, C.E. Stutz, K.R. Evans, D.W. Whitson, Alloy scattering in *p*-type $Al_xGa_{1-x}As$, *J. Appl. Phys.*, 71, 1992, 260-266.

61. E. D. Palik, *Handbook of Optical Constants of Solids* (Academic Press, N.Y., 1988)

62. A. McEvoy, T. Markvart, L. Castaner, *Solar Cells: materials, manufacture and operation* (2nd Edition, Academic Press, 2013)

63. S. Yang, D. Prendergast, J. B. Neaton, Tuning Semiconductor Band Edge Energies for Solar Photocatalysis via Surface Ligand Passivation. *Nano Lett.*, **12**, 383–388 (2012).

64. M. Sheffer, A. Groysman, D. Mandler, Electrodeposition of sol-gel films on Al for corrosion protection, *Corrosion Science,* **45**, 2893-2904 (2003).

65. Y. Zhao, J-C. Grivel, Controlled growth of epitaxial $CeO_2$ thin films with self-organized nanostructure by chemical solution method, *CrystEngComm*, **15**, 3816-3823 (2013).

66. S. Khan, G. Anzimi, B. Yildiz, K. K. Varanasi, Role of surface oxygen-to-metal ratio on the wettability of rare-earth oxides*, Appl. Phys. Lett.,* **106**, 061601 (2015).

67. V. Fernandes, J. J. Klein, W. H. Schreiner, N. Mattoso, D. H. Mosca, Electrodeposition of Nanocrystalline $CeO_2$ on Si(001), *J. Electrochem. Soc.,* **156**, E199-E204 (2009).

68. C. W. Li, M. W. Kanan, $CO_2$ reduction at low overpotential on Cu electrodes resulting from the reduction of thick $Cu_2O$ films. *J. Am. Chem. Soc.*, **134**, 7231–7234 (2012).

69. C. W. Li, J. Ciston, M. W. Kanan, Electroreduction of carbon monoxide to liquid fuel on oxide-derived nanocrystalline copper. *Nature*, **508**, 504–507 (2014).

# APPENDIX

# APPENDIX

## A.1. Tafel analysis for HER.

As thoroughly mentioned in the Introduction and in Chapter 1, HER is a multistep reaction that involves three possible reaction steps. After the first Volmer step (Eq. **A.1a**), also known as electrochemical discharge, either the Heyrovsky (Eq. **A.1b**) or Tafel (Eq. **A.1c**) steps may occur, leading to $H_2$ evolution.

$$H_2O + e^- \rightarrow H_{ads} + OH^- \qquad \text{Eq. A.1a}$$
$$H_{ads} + e^- + H_2O \rightarrow H_2 + OH^- \qquad \text{Eq. A.1b}$$
$$2H_{ads} \rightarrow H_2 \qquad \text{Eq. A.1c}$$
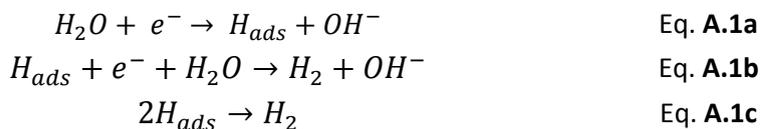
Analysis of the experimental Tafel plots (Log i vs. $\eta$ , see sections **I.3** and **1.3**) allows to investigate the reaction mechanism, highlighting which one of the V-H or the V-T routes would finally give $H_2$.

A general theory of current–potential relations for multistep reactions would need to take into account all potential dependences and surface concentrations of the intermediates involved, as well as the bulk concentrations of educts and products. Fortunately, for HER and in most experimental situations the problem can be significantly simplified for the presence of a single *rds* that limits the overall rate. The current is thus determined by the rate of the *rds* and all other steps can be considered at equilibrium. In the specific case of HER, Tafel analysis is based on the assumption that one between the V, H and T steps is much more sluggish, thus limiting the overall rate.[1,2]

In the following is specified how and why from Tafel analysis it is possible to obtain mechanistic information of HER.

Let consider a general multistep reduction reaction $O + ne \rightleftharpoons R$ which may include a series of chemical and electrochemical reactions. The *rds* can be described with the following general notation:

$$O' + re \rightleftharpoons R' \qquad \text{Eq. A.2}$$
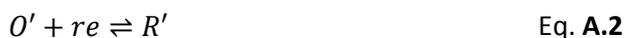
where $r = 0$ in the case the *rds* is a chemical step, and $r = 1$ if it is an electrochemical step. In the case of an electrochemical *rds*, its current is given by:

$$i_{rds} = k_{rds}^f \times C_{O'}^S \times e^{-\alpha F\eta/RT} - k_{rds}^b \times C_{R'}^S \times e^{(1-\alpha)F\eta/RT} \qquad \text{Eq. A.3}$$

$C_{O'}^S$ and $C_{R'}^S$ are the surface concentrations of the intermediates $O'$ and $R'$, $k_{rds}^f$ and $k_{rds}^b$ the rate constants of the forward and back reactions.

For HER, the second term of the previous equation can be neglected, especially in the case are applied moderate $\eta$ (> 50 mV). Eq. **A.3** then simplifies to:

$$i_{rds} = k_{rds}^f \times C_{O'}^S \times e^{-\alpha F\eta/RT} \qquad \text{Eq. A.4}$$

The current is clearly dependent on $C_{O'}^S$, that can be expressed in terms of its bulk concentration $C_{O'}^B$ considering the fact that the steps which precede the *rds* are at equilibrium. By appropriate substitutions, Eq. **A.4** can be written in the Butler-Volmer type current-potential relation, Eq. **A.5**.

$$i = i_0 e^{-\vec{\gamma}_i F\eta/RT} \qquad \text{Eq. A.5}$$

where $i_0$ is the exchange current density. $\vec{\gamma}_i$ is the so called observable charge transfer coefficient (also present in Eq. **I.8.**) and is dependent on the specific reaction mechanism. It is now clear why Tafel plots are very useful tools for the validation of postulated reaction mechanism of multistep reactions, like the case of HER. Indeed, the measured slopes $b$ in Tafel plots ($Log\ I = a + b \times \eta$) reflect the nature of the *rds* since $b$ embodies the term $\vec{\gamma}$, which is characteristic of a particular reaction pathway.

$$b = \frac{2.3 \times RT}{\vec{\gamma}_i \times F} \qquad \text{Eq. A.6}$$

and

$$\vec{\gamma}_i = \frac{n'}{v} + r\alpha \qquad \text{Eq. A.7}$$

where n' are the number of electrons that are transferred in the steps preceding the *rds,* and $v$ is the stoichiometric number of the *rds* (how many times it has to occur for the overall reaction to take place once).

In the case of HER any of the three steps (Eq. **A.1a-c**) can be the *rds,* with $\vec{\gamma}_i$ that would have the following values (considering $\alpha$ = 0.5):

Volmer *rds* (n' = 0, $v$ = 2, r = 1, $\alpha$ = 0.5), then $\vec{\gamma}_V = 1/2$

Heyrovsky *rds* (n' = 1, $v$ = 1, r = 1, $\alpha$ = 0.5), then $\vec{\gamma}_T = 3/2$

Tafel *rds* (n' = 2, $v$ = 1, r = 0, $\alpha$ = 0.5), then $\vec{\gamma}_H = 2$

Substitution of these $\vec{\gamma}_i$ values in Eq. **A.6**. finally results in the characteristic slope values for a Volmer ($b_V$ = 120 mV/dec), Heyrovsky ($b_H$ = 40 mV/dec) or Tafel ($b_T$ = 30 mV/dec) rate determining step. Different $i_0$ would not affect the value of the slope $b$, but are however related to differences in the reaction mechanism since they embody the contributions of intermediates' concentration at the surface and the rate constants of the chemical/electrochemical steps that precede the *rds.*

As demonstrated in Chapter 1, HER on **MWCNT@Pd/TiO₂** is limited by the Volmer step. The rate of HER is then the rate of the Volmer step. The kinetic equation for the case of a Vomler *rds* at neutral pH is expressed in Eq. **A.8b** , that is basically an extended version of Eq. **A.5** in which the various contributions to $i_0$ are specified.

$$r_{HER} = r_{rds} = r_V = k_V(1-\theta)a_{H_2O}^S \qquad \text{Eq. } \textbf{A.8a}$$

Since H$_{ad}$ formation is the *rds,* the surface coverage of H$_{ad}$ can be considered negligible. For $\theta \to 0$ , $i = nFAr$ and $k_V = k_V^0 e^{(-\alpha_V F\eta)}$ , Eq. **A.8a** becomes

$$i_{HER} = i_V = nFAk_V^0 a_{H_2O}^S e^{(-\alpha_V F\eta)} \qquad \text{Eq. } \textbf{A.8b}$$

which is identical to Eq. **A.5**.


## A.2. Electrochemical Cell for the study of CO₂RR

A demanding requirement for quantitative measurements of CO₂RR is the absolute tightness of the electrochemical cell used during bulk electrolysis. An accurate quantification of the reaction products emphasizes the need for a complete suppression of any gas leak, that would otherwise lead to an underestimation of the F.E. To this end, the best way to perform CO₂RR electrolysis is to use a gas-tight cell directly coupled to a Gas Chromatograph, for the online detection of the gaseous products evolved during CA experiments. For a complete description of CO₂RR, also the liquid phase should be collected and analyzed by appropriate characterization techniques (I.C., L.C. or NMR) at the end of each measurement.

The electrochemical characterization of the nanocomposites **MWCNT@CeO₂** and **MWCNT@Pd/CeO₂** presented in Chapter 2, has been entirely performed in a custom-made three electrodes electrochemical cell that possess the above-mentioned requirement of gas-tightness. The cell has been specifically designed during the PhD work and it has been realized in the facilities of the "Centre de Recherche Paul Pascal" (CRPP) in Pessac (France) thanks to a long-standing

collaboration between the EMFM group in Bologna and the research group of Dr. Alain Penicaud in that institution. Special thanks go to Mr. Philippe Barboteaux, who realized the cell.

As can be seen in Fig. **A.1**, the cell presents two threaded cavities near the bottom of the main body, where the R.E. and the C.E. can be accommodated. In this work, a Ag/AgCl R.E. and a Pt spiral C.E. have been used, but others are also possible if they fit within the cavity (4 mm < Ø < 6 mm). Both electrodes are placed into glass tubes and isolated from the electrolytic solution with medium size porous frits. To ensure the gas-tightness at the electrode-cell body junction, Teflon or Viton O-rings are placed around the glass tubes and fitted into PEEK nut connectors (Upchurch Scientific Ltd.) which are screwed directly into the body of the cell.

A peculiar characteristic of the cell is also the bottom part, that consists of circular interchangeable adapters into which different W.E. can be placed. These adapters are tightened with 6 screws to the main body and allow to use different W.E. with different geometries. In this work only rod-like Glassy Carbon electrodes have been used, but commercial SPEs and in general plane electrodes, can be used as well.
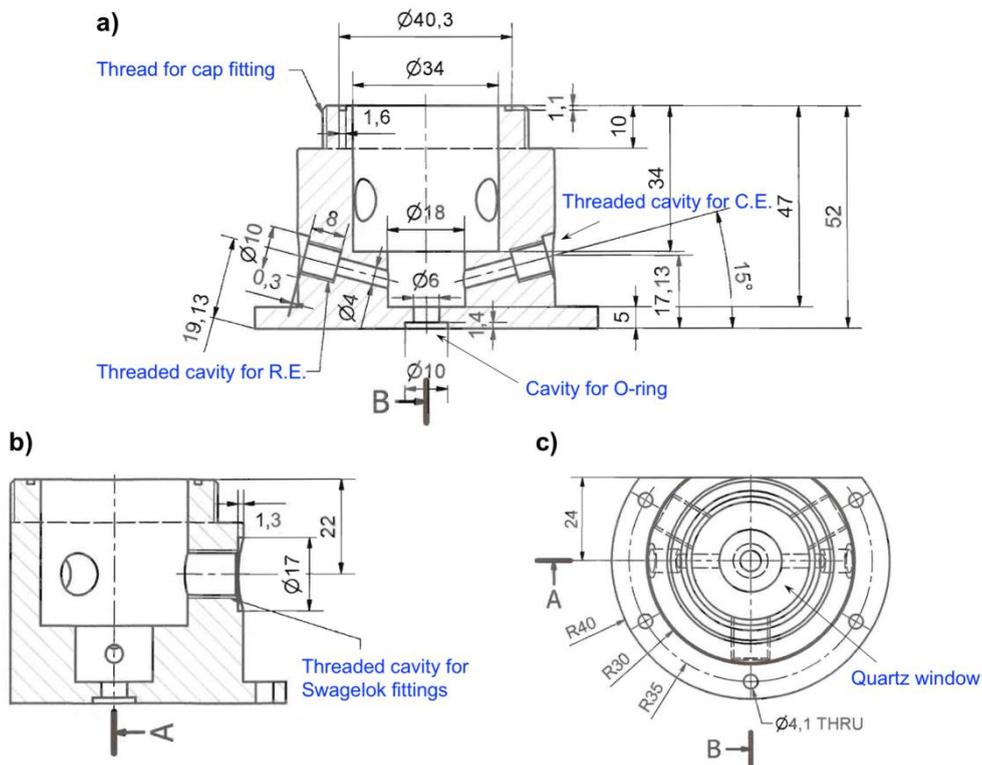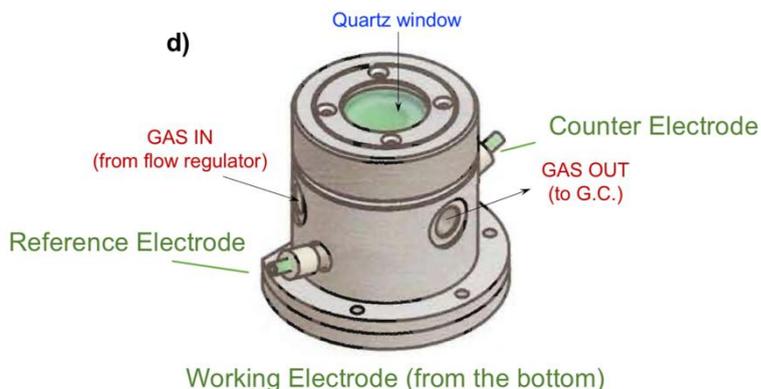
**Figure A.1:** Front, **a)** , lateral **b)** and top **c)** views of the electrochemical cell. **d)** 3D rendering of the electrochemical cell, with highlighted the main components. The working electrode is not visible, but the interchangeable basal plate can accommodate planar SPE as well as rod-like electrodes with $\varnothing$ = 6 mm. The drawings are not in scale.

The top of the cell is closed with a cap that is screwed on the main body. Two Viton sealing are placed between the cell and the cap to avoid the escape of gases.

Connection with the gas line from the cylinders (Ar or $CO_2$) and to the G.C. is assured by two Swagelok stainless steel connectors, that also in this case are screwed into the main body and have Viton O-rings to prevent gas leaks.

With all the mentioned precautions, the cell is finally completely isolated from the external environment and is possible to have a quantitative detection of any product that is generated during $CO_2$RR electrolysis.

It is to note that the top cap of the cell has a quartz window (Edmund Optics), that allow to monitor by eye the positions of the electrodes and the degas of the solution. The main feature of this window is however the possibility to irradiate the W.E. for PEC measurements (not performed in this work).

## A.3. Electrochemical characterization

### A.3.1. Electrochemical work-stations

The electrochemical characterization presented in the thesis has been performed using various electrochemical work-stations. Data in Chapter 1 and 2 have been recorded using a Biologic SP-300 bipotentiostat, equipped with an additional booster kit for high currents (10 A) and a board for EIS measurements (the FRA has a frequency response in the range µHz-MHz).

CA data of Chapter 2, when the electrochemical cell was coupled to a G.C. for products analysis, have been acquired using a CHI 910B bipotentiostat.

All the electrochemical data presented in Chapter 3 were taken with a EG&G 263A potentiostat coupled to a Solartron 1260 FRA. For the EQE measurements of the same chapter a Merlin lock-in amplifier (Newport Oriel) have also been used.

## A.3.2. Electrochemical cell

Experimental data presented in Chapter 1 have been carried out in custom-made single chamber PTFE cells with a 6 mm diameter aperture. SPEs are placed at the bottom of these cells in front of the aperture and tightened using connecting screws. Glass cylinders and Teflon caps placed on top of the PTFE cell ensure a proper gas-tightness. When GC electrodes are used, classic three electrode glass cells are employed. The cells have three top ports to hold the electrodes and an additional port for gas purging. The experiments reported in Chapter 2 have been performed using the electrochemical cell described in section **A.2.**

The PEC characterization of Chapter 3 has been done in a single chamber 250 mL glass electrochemical cell (Pine research instrumentation) with five 14/20 side ports for additional electrodes and gas purging. The cell has also flat optical quartz end faces to irradiate the W.E. with minimal absorption of the incident light (Fig. **A.4**).

## A.4. Experimental techniques

In this section is presented a brief overview of the SECM technique and of the PEC instrumentation that have been used to obtain the results reported respectively in Chapter 1 and Chapter 3.

## A.4.1. Scanning Electrochemical Microscopy (SECM)

Scanning Electrochemical Microscopy is a scanning probe technique that employs micro-nano electrode probes, which are moved in close proximity of a sample surface recording an amperometric signal. The obtained electrochemical response provides quantitative information of interfacial physic-chemical processes and may depend on both the topography and the reactivity of the surface. Indeed, the SECM response is sensitive to the conductivity of the samples and also to the presence of

electroactive species. For these reasons, SECM is useful for the high-resolution (μm-nm length scale) imaging of heterogeneous and homogeneous reactions on surfaces, in order to characterize them and to measure local kinetics.
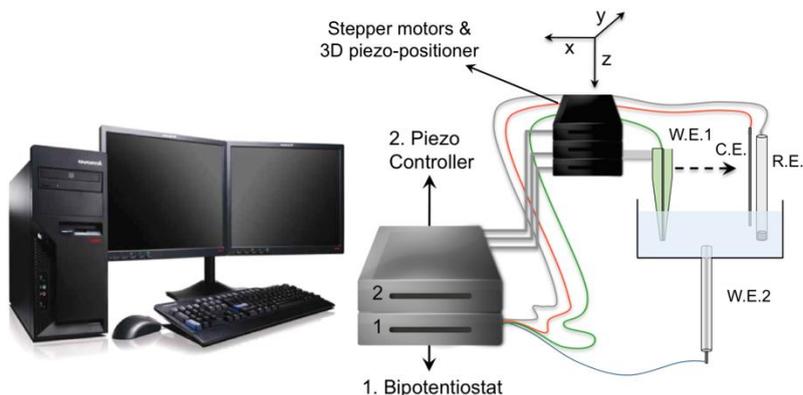


**Figure A.2:** instrumental SECM setup, with highlighted the bipotentiostat and piezo-controller blocks. The bipotentiostat can control two W.E. simultaneously, as requested for SG/TC measurements. The piezo controller governs both the stepper motors for a coarse positioning of the probe, and also the piezo-positioner for finer movements.

SECM probes, with a radius in the range of tens of nm to 25 μm, can induce chemical changes and collect electrochemical information while approaching or scanning the substrate of interest. The probe is held by a support and can be moved in the electrolytic solution using a 3D positioner. This consists of three stepper motors for a coarse positioning of the tip (μm range) and a XYZ piezoelectric block for finer movements. This set up gives a spatial resolution of 1.6 nm and allows maximum travelling distances in the order of few cm.

In Fig. **A.2** are shown the various components of a typical SECM setup. Besides the 3D positioner, the potentiostatic unit usually consists of a bipotentiostat, so that two W.E. can be biased simultaneously using the same R.E. and C.E. This is required for several operational modes of the SECM technique, like the SG/TC mode reported in Chapter 1, and briefly outlined in the section **A.4.1.3**.

### A.4.1.1. Ultramicroelectrodes

One of the fundamental part of the SECM instrumentation is the probe, a micrometric UME.[3] As explained in Chapter 1, section **1.2.1.1**, important features of the UME geometry are the radius of the conductive core ($a$) and the total tip radius ($r$), that accounts also for the thickness of the glass support. The RG ratio

defines the ratio (r/a) and should be kept as small as possible to allow a closer approach to the substrate surface.[4] The advantages of using UMEs reside in the different diffusion regime that occurs on surfaces with micrometric lateral size. With such micrometric electrodes, the diffusion of electroactive species towards the surface is governed by a hemispherical diffusion rather than a planar diffusion like in the case of macroelectrodes. This fact is strictly connected to the obtainment of steady state currents in the typical conditions of CVs experiments (1 mM concentrations and $\nu$ = 10-100 mV/s.

The steady state current for oxidation/reduction of a redox mediator at an UME disk electrode of radius $a$ in the bulk of a solution (x = $\infty$) is expressed by Eq. **A.9**.

$$i_{T,\infty} = 4nFc^*Da \qquad\qquad \text{Eq. } \textbf{A.9}$$

where $D$ is the diffusion coefficient of the redox mediator, $F$ is the Faraday constant and $n$ is the number of the electrons transferred.


## A.4.1.2. Feedback mode

In a feedback-mode experiment the UME tip is placed in a solution containing a redox mediator and is moved vertically along the z-axis until it reaches the proximity of the substrate. When the tip is far from the substrate, applying an appropriate $E_{tip}$ the mediator is oxidized (or reduced) and a stationary current is generated ($i_{T,\infty}$ , see Eq. **A.9**). By contrast, when approaching the surface, the current at a given distance x ($i_{T,x}$) changes to an extent that depends both on the substrate characteristics (conducting or insulating) and on the distance with the surface.

If the substrate is an insulating material the diffusion of the redox mediator at the electrode surface is hindered and the current decreases with respect to $i_{T,\infty}$ . The closer the tip gets to the substrate, the smaller $i_{T,x}$ becomes. This phenomenon is known as *negative feedback* (Fig. **A.3b**). By contrast, when the substrate is electrically conductive the diffusion of the redox mediator to the probe is still hindered by the substrate, but in this case a regeneration of the redox center at the substrate occurs. This regenerated species diffuses to the approaching tip and leads to an increase of current compared to $i_{T,\infty}$, generating a *positive feedback* (Fig. **A.3a**). The plot of the current dependence with distance is called approach curves

and in Fig. **A.3** are highlighted two representative examples of approaching curves exhibiting *positive* and *negative* feedback.
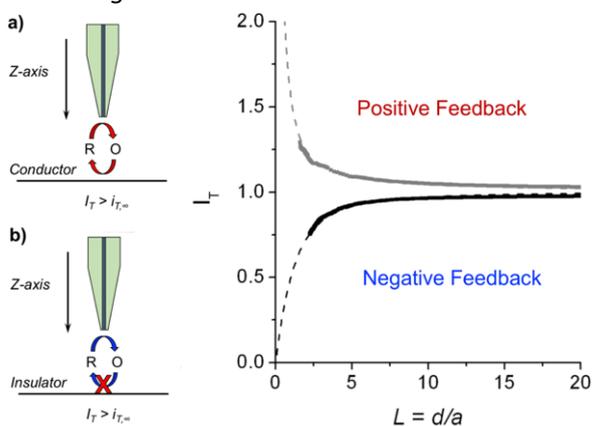


**Figure A.3: a)** probe-tip approaching a conductive substrate in the presence of a redox mediator. A *positive feedback* of current occurs for the regeneration of the redox couple at the conductive surface. **b)** Same situation as in **a)** but in the case of an insulating substrate. Since the mediator is not regenerated approaching the substrate results in a *negative feedback* of current.

These plots are reported in a dimensionless form by plotting $I_T = i_{T,x}/i_{T,\infty}$ versus $L = d/a$. By fitting of the experimental current-distance curves with theoretical equations it is possible to determine the distance scale $L$, which in turn allows to know the effective distance between the tip and the surface (essential for any quantitative SECM measurement). The fundamental analytical expressions for the case of conducting (Eq. **A.10a**) and insulating (Eq. **A.10b**) substrates were numerically calculated by Mirkin and Bard as a function of several RG values.[5]

$$I_T^C(L) = \frac{i_T}{i_{T,\infty}} = k_1 + \frac{k_2}{L} + k_3 \exp\left(\frac{k_4}{L}\right)$$

Eq. **A.10a**

$$I_T^{INS}(L) = \frac{i_T}{i_{T,\infty}} = \frac{1}{\left[k_1 + \frac{k_2}{L} + k_3 \exp\left(\frac{k_4}{L}\right)\right]}$$

Eq. **A.10b**

where $L = d/a$ and $k_1, k_2, k_3$, and $k_4$ are geometrical parameters listed in Ref [5]. Fig. **1.8a** in Chapter 1 refers to an approach curve relative to a **MWCNTs@Pd/TiO₂** substrate. The approach displays a *positive feedback* of current, confirming as expected the conducting nature of the material. By fitting of the experimental data with the appropriate version of Eq. **1.10a** taken from ref. [5] for RG = 3.66 it was possible to determine the exact position of the H₂-probe tip. After that, the tip was

then positioned at a controlled distance from the surface and finally SG/TC experiments for F.E. quantification were performed.

## A.4.1.3. Generation–Collection mode: SG/TC

SG/TC is one of the two generator-collector operational modes, the other one being tip generation-substrate collection (TG/SC). In both cases two working electrodes are needed. A species is electro-generated at one electrode and is collected at the other one. Since two W.E. are used, a bipotentiostat is required to control simultaneously the two electrode potentials.

In the specific case of SG/TC, a product (or more) is generated at the substrate electrode, biased at $E_{sub}$, and collected at the tip-probe, biased at $E_{tip}$. In this thesis SG/TC was used to evaluate the F.E. for HER of the nanostructured catalyst **MWCNTs@Pd/TiO₂**. $H_2$ was generated on the **MWCNTs@Pd/TiO₂** substrate via HER, and collected at a Pt tip-probe via the opposite reaction, HOR. The procedure assumes that the F.E. for HOR at the Pt-tip is unity (as widely accepted for HOR on Pt surfaces).

The SG/TC mode is also very useful for monitoring corrosion, enzymatic reactions, living cell methabolism and more in general, heterogeneous processes that occurs at the substrate surface.

## A.4.2. PEC instrumentation

The PEC characterization of **STO-GaAs** presented in Chapter 3 has been performed with the cell described in section **A.3.2** using a combination of techniques and instrumentation that are not commonly used in "dark" electrochemical studies.

Fig. **A.4** shows the optic table on which the measurements were performed, together with the quartz cell described in section **A.3.2**. Behind the cell of Fig. **A.4a** is highlighted the light source block, that encompasses a 300 W Xe lamp, a chopper (activated during EQE measurements) and a Schottky glass filter, necessary to reproduce the standard AM1.5g solar spectrum. These elements are coupled to a monochromator, activated in EQE measurements to evaluate the wavelength-dependence of the observed photocurrent (see Section **3.2.3)**. The monochromator is otherwise bypassed when the standard AM1.5g illumination (CV and CA experiments) is needed. The yellow arrows display the optic paths for the two cases. When 1 sun illumination hits the W.E., the cell is placed in front of the

light source. By contrast during EQE measurements the gratings inside the monochromator deviate the light, that exits from the lateral side port and is focused on the W.E by means of mirrors and lenses. In Fig. **A.4a** is also evidenced the connection between the lock-in amplifier and the electrodes in the typical setup used for EQE measurements (also visible in Fig. **A.4b**).

In EQE measurements the intensity of incident light is generally low, so as to minimize thermal effects on the photocurrent and also possible photodecomposition of the electrode. In the setup in use, the intensity of the 300 W Xe lamp is highly reduced inside the grating monochromator and the light reach the W.E. surface with an intensity of $\sim$1 mW/cm$^2$. Since low light intensities hit the W.E., the corresponding photocurrents are rather small and a connection with the lock-in amplifier is therefore needed to enhance the sensitivity by many orders of magnitude. In this way, the chopper highlighted in Fig. **A.4a** interrupts the light at a certain frequency so that the lock-in amplifier can distinguish even very small photocurrents from background (dark) currents.

The intensity of the light on the W.E. is calibrated for 1 sun measurements with a c-Si PV reference cell (SI BK-7, PV measurements).
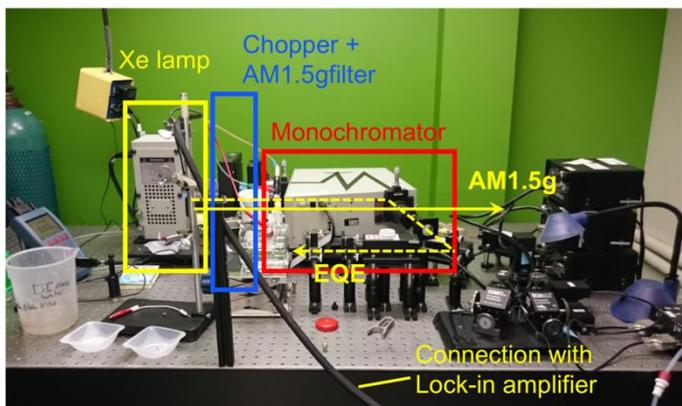
**a)**                                                                          **b)**



**Figure A.4: a)** picture of the optic table used for the characterization of STO-GaAs reported in Chapter 3. The various elements are highlighted. In this specific case, the cell is positioned so as to perform EQE measurements in which the incident wavelength is selected by the grating monochromator. **b)** picture of the electrochemical cell used for PEC characterization. The flat end faces are made of quartz so that the W.E. (the one with the yellow cap in the picture) can be illuminated with no absorption of incident light by the glass. The additional side ports allow to purge the solution with gases and also to couple cell with a G.C. line for the online detection of evolved products (H$_2$ in this case).

# A.5 Bibliography

1. K. Krischer, E. R. Savinova, *Fundamentals of electrocatalysis*, in *Handbook of Heterogeneous Catalysis*, *2nd Ed*., Eds. G. Ertl, H. Knozinger, F. Schuth, J. Weitkamp (Wiley-VCH Verlag, Weinheim, 2008).
2. O'M J. Bockris, A. K. N. Reddy, *Modern Electrochemistry* (Plenum Pr. New York, 1970).
3. P. Sun, F.O. Laforg, M. V. Mirkin, Scanning Electrochemical Microscopy in the 21$^{st}$ century. *Phys. Chem. Chem. Phys*., **9**, 802-823 (2007). *(b)* M. V. Mirkin, W. Nogala, J. Velmuruga, Y. Wang, Scanning Electrochemical Microscopy in the 21$^{st}$ century. Update 1: five years after, *Phys. Chem. Chem. Phys.*, **13**, 21196-21212 (2011).
4. A. J. Bard, Introduction and principles (Chapter 1) in *Scanning Electrochemical Microscopy*. A. J. Bard and M. V. Mirkin (Eds.) (Marcel Dekker, New York, 2001).
5. M. V. Mirkin, F-RF. Fan, A. J. Bard, Scanning Electrochemical Microscopy. 13 Evaluation of the tip shapes of nm-size microelectrodes. *J. Electroanal. Chem*., **328**, 47-62 (1992).

# Acknowledgments